

**The Lifetime of a Beautiful and
Charming Meson : B_c Lifetime
Measured Using the DØ Detector**

Leah Welty-Rieger

Submitted to the faculty of the University Graduate School

in partial fulfillment of the requirements

for the degree

Doctor of Philosophy

in the Department of Physics

Indiana University

September 2008

Accepted by the Graduate Faculty, Indiana University, in partial fulfillment
of the requirements for the degree of Doctor of Philosophy.

Rick Van Kooten, Ph.D.

Mike Berger, Ph.D.

Harold Ogren, Ph.D.

Mark Messier, Ph.D.

July 31, 2008

Copyright 2008

Leah Welty-Rieger

ALL RIGHTS RESERVED

Acknowledgements

The road to a PhD isn't easy for anyone. Along that road one meets several people that provide support and guidance. Without them, the path would definitely be rockier and might just lead one off a cliff.

First of all I must thank my adviser, Rick Van Kooten. I made the decision to come back to Indiana University for graduate school with the specific goal to work with Rick for the duration of the program. That has proven to be one of the better decisions I have made in my lifetime. There were several times during this analysis when there was not even a flicker of light at the end of that proverbial tunnel (if there was even a tunnel at all). During those times I thought the thesis you are about to read would never come to fruition, but Rick was always able to work with me on the next step or the next thing to try. Eventually all the components came together and the analysis started falling into place and before I knew it...Bob's your uncle.

It has also been a pleasure being able to talk to Rick about topics outside the realm of physics. He will always be one of the most important people in my life and I'm so pleased to have had the opportunity to work with him over the past six years.

I would next like to thank the B physics group at DZero and my Editorial Board for all of their support, suggestions, and good questions. I also want to thank Mike Berger, Harold Ogren and Mark Messier who were the members of my thesis committee for their detailed review of this thesis.

A thank you must go out to Brendan Casey for being there to listen to my questions or general frustrations. In addition, his support in meetings was greatly appreciated. While I was probably a little terrified of him when I first came to the lab, I found that he was one of the nicest and most supportive people at Fermilab. I also have to thank my old office mate, Dan Krop. While our office was a tad on the tight side, it was a huge benefit to have Dan next to me. His help at the start of this analysis was invaluable. Thank you to Aaron and Karen, our friends in Bloomington, for making graduate school so much more enjoyable by always coming over on Thursdays nights for homework, pizza and good bad TV. They are great friends and will always be a part of my life.

To my mom, well, what I can say. I would call you at times with tears rolling down my face, sadly stating, "It's never going to happen, Mom." You would respond with, "Of course it's going to happen. Just keep working at it and you will be there sooner than you realize." Of course, a perfect child would just listen, but I told her she just couldn't possibly understand my woes. However, a little part of that would get in and, in the end, her message pushed me harder to prove to her that her baby girl could do it and wasn't a quitter. Also I would like to thank her husband Ken for being a supportive force as well.

To my dad: So many years ago when I was a kid in your physics class, I wonder what you thought I would be when I grew up. I think we both know that, at that time, PhD physicist probably didn't cross your mind. Thank you for all the help; not only on the other end of 4am homework hotline phone calls, but also just for always being so supportive. I know it was hard for you to listen to what was happening at times but thank you for listening and being here when I really needed it. I don't think I could have gotten through those last few months without you. Also I would like to thank Sue, my stepmom, for always being the calming presence who I could talk with and who would listen without judgement.

Last but not least. To Jason. My husband. My best friend. My lab partner. I don't know how to thank you and I don't know if I even can, simply because words would not be fair to how much you mean to me. Not many couples go through graduate school together, let alone under the same adviser in the same research group. People can never believe that we didn't kill each other but, without you - hands down - I wouldn't have finished this program. You have not only helped me on several aspects of this analysis, especially with the Monte Carlo generation, but have been there to listen to new things I thought I could try or a new direction I could go and it has been wonderful. When you were assigned as my lab partner so many years ago, I immediately knew you were someone special and someone who would be in my life forever. That proves to hold true and you mean more to me than any other person on the planet. I love you.

Abstract

Using approximately 1.3 fb^{-1} of data collected by the DØ detector between 2002 and 2006, the lifetime of the B_c^\pm meson is studied in the $B_c^\pm \rightarrow J/\psi \mu^\pm + X$ final state. Using an unbinned likelihood simultaneous fit to $J/\psi + \mu$ invariant mass and lifetime distributions, a signal of 810 ± 80 (stat.) candidates is estimated and a lifetime measurement made of:

$$\tau(B_c^\pm) = 0.448_{-0.036}^{+0.038} \text{ (stat)} \pm 0.032 \text{ (sys) ps.}$$

Contents

List of Figures	xiv
List of Tables	xxiii
1 Introduction	1
2 Theoretical Overview	3
2.1 The Standard Model	4
2.2 CP Violation & Unitarity CKM Matrix	11
2.2.1 The Unitarity CKM Matrix	11
2.2.2 Parameterization of the CKM Matrix	14
2.2.3 The Unitarity Triangle	15
2.3 Semileptonic B Meson Decays	17
2.3.1 b -Quark Branching Fraction	19

2.3.2	b -Quark Lifetime	20
2.4	B_c^\pm Meson	22
2.4.1	Spectroscopy	23
2.4.2	Mass	24
2.4.3	Production	25
2.4.4	Theory of B_c^\pm Decays	30
2.4.5	Discussion and Conclusions	41
2.5	Motivation for this Measurement	42
3	Experimental Apparatus	50
3.1	The Tevatron Accelerator Complex	50
3.1.1	Proton Production and Acceleration	51
3.2	The DØ Detector	55
3.2.1	The Coordinate System	56
3.2.2	Central Tracking Systems	57
3.2.3	Preshower Detector	65
3.2.4	Calorimeter	66
3.2.5	Muon System	72
3.2.6	Luminosity	79
3.3	The DØ Trigger System	81

3.3.1	Level 1	82
3.3.2	Level 2	83
3.3.3	Level 3 and Data Acquisition	84
4	Reconstruction and Simulations	88
4.1	Event Reconstruction	88
4.1.1	Track Reconstruction	89
4.2	Event Simulation	97
4.2.1	Event Generation	98
4.2.2	Detector Simulation	99
5	Analysis	103
5.1	Overview	104
5.2	Monte Carlo Samples	105
5.2.1	Signal MC	106
5.2.2	$\psi(2S)$ Monte Carlo	106
5.2.3	J/ψ QCD Monte Carlo	107
5.2.4	Optimization of MC $p_T(b)$	110
5.3	Pseudo-Proper Decay Length	110
5.4	Event Selection	114

5.4.1	Data Set	114
5.4.2	Preventing Trigger Bias	118
5.4.3	J/ψ Selection	119
5.4.4	$J/\psi + \text{Track}$ Selection	121
5.4.5	$J/\psi + \mu$ Selection	122
5.5	Contributions to the $J/\psi + \mu$ Sample	122
5.5.1	B_c^\pm Signal	125
5.5.2	Real J/ψ & Fake μ	126
5.5.3	Fake J/ψ & Real μ	128
5.5.4	Real J/ψ & Real μ	130
5.5.5	B^+	132
5.5.6	Prompt $J/\psi + \mu$	132
5.6	Demonstration of B_c^\pm Signal	134
5.6.1	Presence of B_c^\pm Signal	135
5.6.2	Demonstration of Short Signal Lifetime	139
5.7	Lifetime Analysis	140
5.7.1	Prompt J/ψ ($c\bar{c}$)	142
5.7.2	Real $J/\psi + \text{Fake } \mu$	144
5.7.3	Fake $J/\psi + \text{Real } \mu$	145

5.7.4	Real J/ψ + Real μ	146
5.7.5	B^+	147
5.7.6	Signal	148
5.7.7	Full Fit and Results	151
6	Systematic Uncertainties and Analysis Checks	156
6.1	Mass Shape Systematic Uncertainties	157
6.1.1	Signal Decay Model	157
6.1.2	$\psi(2S)$ Feed-Down Signal Component	157
6.1.3	Uncertainty on the B_c^\pm p_T Distribution	158
6.1.4	Uncertainties on $p_T(b)$ Distributions	160
6.1.5	J/ψ MC Mass Distribution	162
6.1.6	J/ψ Sideband Mass Distribution	163
6.1.7	Prompt Mass Distribution	165
6.2	Lifetime Model Systematic Uncertainties	165
6.2.1	Signal Lifetime Model	165
6.2.2	Prompt Lifetime Model	168
6.2.3	J/ψ Sideband Lifetime Model	168
6.2.4	J/ψ QCD Monte Carlo	168
6.2.5	B^+ Lifetime Model	169

6.3	Alignment Systematic	170
6.4	Split Sample Tests	170
6.5	Summary	172
7	Summary and Conclusion	174
8	Appendix A	179
	Bibliography	182

List of Figures

2.1	Unitarity triangle. The upper portion corresponds to Eqn. 2.9, while the bottom shows the definition of ρ and η , where the triangle has been rescaled dividing each side by $ V_{cd}V_{cd}^* $	18
2.2	Free b quark decay.	44
2.3	μ decay.	45
2.4	The B_c^\pm mass spectrum (from Ref. [13].)	46
2.5	The dependence of the differential cross section on the factorization scale μ (Ref [20]).	47
2.6	The three possible decay paths of the B_c^+ meson.	48
2.7	Ladder diagram of the Coulomb-like interaction	48

2.8	The B_c^\pm lifetime predictions as calculated by QCD Sum Rules versus the scale of the hadronic weak lagrangian in the decays of the charm quark. The arrow depicts the preferred choice for $\mu = 0.85$ as determined in Ref. [25]. The wide-light blue shaded region shows uncertainties of semi-inclusive estimates. The dark purple shaded region is the preferable choice determined by charm quark lifetimes. The thin shaded band represents the result obtained by summing up exclusive channels in the decays of \bar{b} . The data points with error bars represent the solutions from the OPE approach [23]	49
3.1	Fermilab Accelerator Complex.	51
3.2	The DØ Detector.	55
3.3	Schematic drawing depicting the central detectors in the DØdetector.	57
3.4	Schematic drawing depicting the DØ tracking system.	58
3.5	Schematic of the silicon microstrip tracker.	60
3.6	Cross section of the SMT barrel.	60
3.7	Cross section of the Central Fiber Tracker.	63
3.8	A typical LED spectrum for a single VLPC showing the resolution of single photons.	64

3.9	Cross section and layout of the CPS and FPS. The circles represent the location of the wavelength-shifting fiber.	67
3.10	Cutaway view of the calorimeter system of the DØ detector.	69
3.11	Schematic of calorimeter cell showing the Liquid Argon gap and signal board unit cell.	71
3.12	Quarter cutaway view showing segmentation pattern of calorimeter.	72
3.13	Schematic view of Proportional Drift Tubes and Mini Drift Tubes.	75
3.14	Schematic view of the muon scintillation counters.	76
3.15	Cross-sectional view of mini drift tube.	78
3.16	Schematic showing the location of the luminosity monitors within the DØ detector.	80
3.17	Schematic of luminosity monitor, showing scintillation counters (triangular segments) and PMTs (block dots).	80
3.18	The DØ trigger system.	82
3.19	Flowchart showing the DØ Level 1 and Level 2 trigger system.	85
3.20	Schematic representation of L3 system and data acquisition.	86

4.1	Examples of $b\bar{b}$ pairs generated in the PYTHIA stage of MC generation. (a) Using <code>mse1 = 5</code> or back-to-back MC production. (b) An example of producing a $b\bar{b}$ pair through gluon splitting that can be obtained through <code>mse1 = 1</code> production that also produces $b\bar{b}$ pairs through gluon splitting and flavor creation as well as back-to-back production	100
5.1	p_T of the lower momentum muon from the J/ψ decay.	108
5.2	p_T of the lower momentum muon coming from the J/ψ after forcing equal normalization at higher p_T	108
5.3	Weighting function applied to the first QCD J/ψ MC Sample.	109
5.4	Monte Carlo weighting function for $p_T(b)$	111
5.5	K -factor distribution as determined in the signal Monte Carlo sample.	115
5.6	K -factor distribution in the $B_c \rightarrow \psi(2S)\mu\nu$ signal sample compared to the $B_c \rightarrow J/\psi\mu\nu$ signal MC sample.	116
5.7	K -factor distribution separated in bins of $M(J/\psi\mu)$ as determined in the signal Monte Carlo.	117

5.8	Variables used to separate signal from the background: (a) transverse momentum, p_T of the third track; (b) momentum, p of the third track; (c) p_T of J/ψ + track vertex; (d) χ^2 of J/ψ + track vertex; (e) angle between J/ψ and third track; and (f) maximum $\cos\theta$ between any two tracks.	123
5.9	Distribution of $M(J/\psi\mu)$ in the B_c^\pm signal Monte Carlo sample.	127
5.10	Distribution of $M(J/\psi\mu)$ in the $B_c \rightarrow \psi(2S)\mu\nu$ signal Monte Carlo sample compared to that from $B_c \rightarrow J/\psi\mu\nu$	127
5.11	B^+ mass peak fit in the (a) J/ψ + track data sample and the (b) $J/\psi + \mu$ sample. The ratio of fitted number of B^+ candidates is used to estimate the fraction of candidates due to real J/ψ but fake μ	129
5.12	Distribution of $M(J/\psi\mu)$ within the J/ψ + track sample, clearly showing the B^+ peak at a mass of ~ 5 GeV	129
5.13	Fit of the J/ψ mass in the $J/\psi + \mu$ sample with the yellow band delineating the two sideband regions.	131
5.14	Distribution of $M(J/\psi\mu)$ within the J/ψ sideband sample. This is the mass template for the fake J/ψ and real μ component.	131

5.15	Distribution of $M(J/\psi\mu)$ in the J/ψ QCD MC sample that is used to model the mass of the real J/ψ and real μ background component.	133
5.16	Fit of the B^+ peak in the $J/\psi + \mu$ mass distribution. The yellow histogram is an estimate of the mass template that is used in the full fit.	133
5.17	Mass distribution of the events in the $J/\psi + \mu$ data sample with negative decay length: (a) distribution with a fit to a Landau function; and (b) histogram based on the fit in (a) and used as the mass template.	134
5.18	Fit to the mass of the $J/\psi + \mu$ vertex with all components and no additional cuts applied.	137
5.19	Fit to the mass of the $J/\psi + \mu$ vertex with all components and decay length significance $L_{xy}/\sigma(L_{xy}) > 4$ required.	137
5.20	Fit to the mass of the $J/\psi + \mu$ vertex with J/ψ mass sideband subtracted and decay length significance $L_{xy}/\sigma(L_{xy}) > 4$ required.	138

5.21	Fit to the mass of the $J/\psi + \mu$ vertex with J/ψ mass sideband and B^+ component subtracted and decay length significance $L_{xy}/\sigma(L_{xy}) > 4$ required.	138
5.22	Mass fits after cutting progressively harder on the pseudo-proper decay length (PPDL) of the vertex. Note that there is still signal apparent at the lower PPDL cuts, but for very large values, the fit indicates that the components are dominated by the long-lived J/ψ QCD and the B^+ components; the prompt component has almost completely disappeared as has the signal.	141
5.23	PPDL of events with negative decay length, mirrored about the zero point of the x axis.	144
5.24	Fit to PPDL distribution of events in the $J/\psi +$ track data set. As will be seen, the contribution of this category in the final fit will only be a few percent.	145
5.25	Fit to PPDL distribution of events in the J/ψ mass sidebands.	147
5.26	Fit to PPDL distribution of the J/ψ QCD MC sample.	150
5.27	True decay length of the B_c versus the measured PPDL for the B_c signal MC.	151

5.28	PPDL and Mass distribution of the $J/\psi + \mu$ sample with the projected components of the fit overlaid. The hatching on the mass distribution is the systematic uncertainty of all the components as well as the statistical uncertainty from the sideband component, which is the largest contribution.	155
6.1	$M(J/\psi\mu)$ difference for the ISGW and Phase Space (PHSP) Models.	158
6.2	Predicted $p_T(B_c)$ distribution after event selection before and after reweighting to different factorization scales.	159
6.3	Mass of the $J/\psi + \mu$ distribution in the signal Monte Carlo sample with and without the $p_t(b)$ weighting applied.	161
6.4	Mass of the $J/\psi + \mu$ distribution in the J/ψ QCD Monte Carlo sample with and without the $p_T(b)$ weighting applied.	161
6.5	$\Delta(\phi)$ distribution for several different parentage categories. . .	164
6.6	$\Delta(\phi)$ distribution for demonstrating gluon splitting contribution.	164
6.7	Depiction of the s scale factor taken as a function of decay length rather than a constant value.	167

7.1	Lifetimes of the B_c^\pm meson at the DØ and CDF experiments as well as comparing with theoretical predictions.	177
7.2	Lifetimes of various B hadrons including the experimental measurement of the B_c^\pm meson of this thesis.	178

List of Tables

2.1	Properties of the fundamental quarks.	5
2.2	Properties of the fundamental leptons.	6
2.3	The fundamental forces and their properties.	11
2.4	Theoretical and experimental values of the B_c^\pm mass.	25
2.5	B_c^\pm branching ratio percentages calculated in various theoretical approaches. (Ref. [22]).	33
2.6	B_c^\pm lifetime and width predictions for various c -quark mass choices [23]. The partial widths are listed in ps^{-1} and the lifetimes in ps.	36
2.7	Lifetime predictions for the B_c^\pm meson.	41
3.1	Summary description of the silicon microstrip detector.	62
5.1	Function parameters for empirical $J/\psi + \text{track}$ PDDL model.	146

5.2	Function parameters for the empirical J/ψ mass sideband PPDL model.	148
5.3	Function parameter for J/ψ QCD MC PPDL model.	149
5.4	Results of the full simultaneous likelihood fit.	153
5.5	Correlation matrix of all variables in the full fit.	154
6.1	Split sample tests.	171
6.2	Summary of estimated systematic uncertainties.	173
7.1	Experimental measurement compared with various theoretical predictions and the average (HFAG) of the experimental results.	176

Chapter 1

Introduction

“Our imagination is stretched to the utmost, not, as in fiction, to imagine things which are not really there, but just to comprehend those things which ‘are’ there.” –Richard Feynman

“Make no little plans; they have no magic to stir men’s blood and probably will themselves not be realized. Make big plans; aim high in hope and work, remembering that a noble, logical diagram once recorded will not die.” –Daniel Burnham

The field of high energy physics begs the question of not only “What’s out there?”, but also “What used to be there?” We are searching for the very smallest particles at the very highest energies. The hope is to not only find

these particles that are predicted by theoretical models and perhaps discover new ones, but to simultaneously dial back the clock and attempt to spy on the conditions that were in place when the clock struck zero marked by the Big Bang. This scientific quest is currently driven by the particle accelerator at the Fermi National Laboratory but the array of things we can see will be increased many fold in the upcoming decade by the accelerator complex at the CERN laboratory located in Switzerland.

The topic presented in the following text is just a small kernel of information being added into the great pool of existing analyses and results. A small kernel perhaps, but a great amount of information still exists within its boundaries. This thesis starts off with some theoretical background and provides motivation for the measurement of the lifetime of the B_c^\pm meson. General information about the Fermi National Laboratory will then be given as well as a description of the DØ detector which is used to collect the data.. After setting the stage with the first two sections, the lifetime analysis is presented and conclusions are drawn.

Chapter 2

Theoretical Overview

“He who loves practice without theory is like the sailor who boards ship without a rudder and compass and never knows where he may cast.” –Leonardo da Vinci

“It is a test of true theories not only to account for, but to predict phenomena” –William Whewell

This chapter gives an overview of the physics that is generally studied in particle physics and provides the motivation to study the lifetime of the B_c^\pm meson.

2.1 The Standard Model

To understand elementary particle physics, one must, at the very least, be aware of the Standard Model, a mathematical theory that describes the relationships between all the fundamental particles that are studied in particle physics. While it's remarkably complete, the Standard Model does not encompass all of nature as it is unable to predict the masses of particles and does not include a theory of gravity. The Standard Model, having gone through scrupulous testing, has stood up exceptionally well to experimental results.

Within the Standard Model, the fundamental particles are primarily categorized into two groups that are based on their spin. The first type are called fermions and have half integer spin. The fermions can be further divided into two types known as quarks and leptons. Another step of classification that occurs within the fermion label is that they can be organized into three groups, known as *generations*, of particles. Each of the generations consists of a pair of quarks and a pair of leptons.

Quarks have either a charge of $-\frac{1}{3}e$, which are known as 'down-type' or $+\frac{2}{3}e$, known as 'up-type'. There are six flavors of quarks : up (u), down (d), strange (s), charm (c), bottom (at times referred to as 'beauty') (b) and top

(t). The u , c and t are the ‘up-types’ while the d , s and b are referred to as the ‘down-types’. Within a generation, the quark doublet consists of one up-type quark and one down-type quark. Table 2.1 lists the quarks and their basic properties [3].

Table 2.1: Properties of the fundamental quarks.

Generation	Quark name	Symbol	Charge (e)	Mass (MeV)
1 st	up	u	+2/3	~ 3
	down	d	-1/3	~ 5
2 nd	charm	c	+2/3	~ 1200
	strange	s	-1/3	~ 100
3 rd	top	t	+2/3	$\sim 178,000$
	bottom	b	-1/3	~ 4500

The other set of fermions, known as leptons, also has six members. They consist of: the electron (e), muon (μ), tau (τ) as well as their associated neutrinos (ν_e , ν_μ and ν_τ). In the original Standard Model theory, the neutrinos were assumed to have zero mass. However, experimental results [2] contradicted this assumption, having found that neutrinos have non-zero, although very small, mass. Neutrinos have no electric charge, while the other three leptons have a charge of -1 . A summary of the lepton properties can be found in Table 2.2 [3].

Table 2.2: Properties of the fundamental leptons.

Generation	Lepton name	Symbol	Charge (e)	Mass (MeV)
1 st	electron	e	-1	0.511
	electron neutrino	ν_e	0	$< 3 \times 10^{-6}$
2 nd	muon	μ	-1	105.6
	muon neutrino	ν_μ	0	< 0.19
3 rd	tau	τ	-1	1777
	tau neutrino	ν_τ	0	< 18.2

It should be noted that for every particle listed in Table 2.1 and 2.2, there is a corresponding antiparticle. This antiparticle is identical to the particle in every way except for having opposite electric charge (as well as other quantum numbers). An example would be the electron, which has an antiparticle, the positron, which has the same mass but with a charge of $+e$.

The second type of fundamental particle is called a vector gauge boson and has integer spin. These particles come into play when discussing the fundamental forces that are present in the Standard Model arises. There are four of these fundamental forces, namely the gravitational, weak, electromagnetic and strong force, listed in order of increasing strength. Most of these forces are responsible for the interactions that are present between the fundamental particles, e.g. the electromagnetic and weak force between

the W^+W^- , etc. However, the gravitational force, although plainly evident in everyday life, is not described by the Standard Model. The gravitational force is evident in everyday life only for very large masses, such as planets, but it is of negligible strength between fundamental particles when compared to the other three forces. A universal quantum theory that would encompass all four forces has not yet been constructed. The other three forces are mediated by the bosons: the photon (γ), Z^0 and W^\pm , and gluons (g); a discussion of them follows. The properties of all the forces that will be discussed can be found in Table 2.3.

All fermions experience the weak force, and neutrinos are affected by the weak force only. The weak interaction is mediated by the massive Z^0 and W^\pm bosons and thus this force operates at short distances, i.e. $\sim 10^{-16}$ cm. Particles that involve the weak interaction have a comparatively large lifetime on the the order of 10^{-12} to 10^{-8} s, while particles participating in the electromagnetic and strong forces have lifetimes on the order of 10^{-16} s and 10^{-23} s, respectively. Electromagnetic interactions are described by Quantum Electrodynamics (QED) [4]. As per QED, charged particles interact via photon exchange. This force falls off as the inverse of distance squared and has infinite range.

In the late 1960s, a gauge theory was proposed by Glashow, Weinberg and Salam [5] that unified the weak and the electromagnetic interactions. That theory is aptly entitled the Electroweak Theory. The gauge symmetry group of the electroweak force, $SU(2)_L \times U(1)_Y$ has the requirement that four massless gauge bosons exist. However, in order to describe the weak interaction phenomenology at low energies, the vector bosons that mediate this force acquire a non-zero mass via a process known as spontaneous symmetry breaking [6]. This is implemented through the Higgs Mechanism [7]. In short, the Higgs Mechanism introduces a complex scalar field. When this is done, 3 of the 4 gauge vector bosons acquire a mass. These three are the W^\pm that mediate charged-current weak interactions and the Z^0 that conversely mediates neutral-current interactions. The massless vector boson, is then the photon, which is the force carrier in electromagnetic interactions.

The final force that needs to be discussed is the strong force which is mediated by gluons. Quantum ChromoDynamics (QCD) [8], which is a $SU(3)_C$ gauge field theory, describes the interactions between the quarks and the gluons and is responsible for the strong force. Gluons are a set of eight massless vector particles that mediate the strong force between particles with “color charge”. In QCD color charge is the equivalent of the electric charge found in

the QED theory. The colors are arbitrarily labeled red, green and blue and have corresponding anti-charges. Photons couple to the electric charge in QED but are electrically neutral themselves so do not couple at first order to another photon. However, gluons carry color charge themselves, and therefore interact with themselves and each other in QCD. A consequence of this is that the strength of the strong interaction coupling constant (α_S) increases with long distance (low energy) and decreases at shorter distances (high energy). This behavior, very different from other field theories, leads to two features of QCD, namely “quark confinement” and “asymptotic freedom”.

The first of these features, quark confinement, explains the fact that quarks will never be found as free particles. They are instead found in quark-antiquark pairs which are known as mesons, or in three-quark bound states which are known as baryons. Collectively, meson and baryon bound states are known as hadrons. This is true for five out of six of the quark types. Due to the very short lifetime of the top quark, it cannot hadronize with any of the other five quarks and thus does not combine with them to make a hadron. Therefore all the hadrons observed either in nature or in the laboratory is made up of the other five quarks. Looking specifically at a meson, what happens if one were to try and separate the quark from its anti-

quark sibling? As the distance between the two increased and thus the strong force grew stronger, either the quarks would be brought back together by the increased attraction, or the energy would be so great that one would be able to create a quark-antiquark pair from the vacuum. So instead of separating the two quarks, one would be left with two mesons from the original quarks and antiquarks and the newly created quark and antiquark in the vacuum.

We now examine the other QCD feature of asymptotic freedom. If one looks closely at the quarks within the hadron they will behave as free particles, due to the quarks now being close together and thus having a smaller coupling constant, α_s . This region of asymptotic freedom in QCD is explored experimentally by observing the results of collisions between hadrons at high energies. These collisions can be thought of as high momentum transfer interactions between the gluons and the quarks within the hadrons. In the case of this thesis, collisions between protons and antiprotons are observed and will be discussed in further detail in the following chapter.

Table 2.3: The fundamental forces and their properties.

Force	Carrier	Range (cm)	Relative Strength	Mass (GeV)	Electric Charge	Spin
Gravity	graviton (G)	infinite	10^{-40}	0	0	2
Weak	W^+	10^{-16}	10^{-6}	80.4	1	1
	W^-			80.4	-1	1
	Z^0			91.2	0	1
EM	photon (γ)	infinite	10^{-2}	0	0	1
Strong	gluons (g)	$\sim 10^{-13}$	1	0	0	1

2.2 CP Violation & Unitarity CKM Matrix

2.2.1 The Unitarity CKM Matrix

For the work of this thesis it will be necessary to look at more details concerning the weak force. When a b quark decays to a c quark, it does so through a weak decay and thus there must be an understanding of this process. In the Standard Model the weak charged current between the three generations of up-type quarks (u , c and t) and the down-type quarks (d , s and b) is defined as

$$J_\mu^{CC} = (\bar{u}, \bar{c}, \bar{t}) \gamma_\mu \frac{(1 - \gamma^5)}{2} U \begin{pmatrix} d \\ s \\ b \end{pmatrix}. \quad (2.1)$$

where U is a unitary 3×3 matrix which is known as the Cabibbo-Kobayashi-Maskawa (CKM) matrix [9] in mixing space, and $\frac{\gamma_\mu(1-\gamma^5)}{2}$ is the weak charge current where $\gamma^5 = i\gamma^0\gamma^1\gamma^2\gamma^3$. Looking at more detail at the CKM matrix, its elements are as follows:

$$U = \begin{pmatrix} V_{ud} & V_{us} & V_{ub} \\ V_{cd} & V_{cs} & V_{cb} \\ V_{td} & V_{ts} & V_{tb} \end{pmatrix}. \quad (2.2)$$

Each of the V_{ij} elements in the CKM matrix is a complex number that represents the coupling strength between the particular set of up-type and down-type quarks it is describing. More specifically, when down-type quarks undergo a weak interaction to up-like quarks, the matrix element is the representation of the interaction amplitude of the decay vertex. For example, the decay vertex at which a b quark decays through a W^- to a c quark would include a term that is represented by V_{cb} . What happens if the c quark decays to the b quark (or more generally up-type quarks go to down-type quarks)? In that case, the interaction amplitude is represented by the complex conjugate of the matrix element in question, namely in this case V_{cb}^* . Note, from this we can say that the probability for a quark q to transition to another quark q' is proportional to $|V_{qq'}|^2$.

In general, a $n \times n$ matrix would have $2n^2$ free parameters necessary to describe the matrix. In this case, we have 18 parameters as we have a 3×3 matrix. However, it was previously mentioned that this matrix must be unitary: $U^\dagger U = 1$. With this requirement, the number of parameters drops by a factor of two leaving n^2 parameters. Another $2n - 1$ parameters can be eliminated due to the fact that the phases are arbitrary and we are left with $(n - 1)^2$ free parameters. For $n = 3$ this results in 4 independent free parameters. They can be represented by three real Euler angles and a single complex phase. The Euler angles are rotation angles and referred to as mixing angles. The complex phase allows for CP violation.

The most up to date values of each of the elements in the CKM matrix are shown in after performing a global fit to the CKM matrix are shown in Eq. 2.3 [3].

$$U = \begin{pmatrix} 0.97383_{-0.00023}^{+0.00024} & 0.2272_{-0.0010}^{+0.0010} & (3.96_{-0.09}^{+0.09}) \times 10^{-3} \\ 0.2271_{-0.0010}^{+0.0010} & 0.97296_{-0.00024}^{+0.00024} & (42.21_{-0.80}^{+0.10}) \times 10^{-3} \\ (8.14_{-0.64}^{+0.32}) \times 10^{-3} & (41.61_{-0.78}^{+0.12}) \times 10^{-3} & 0.999100_{-0.000004}^{+0.000034} \end{pmatrix} \quad (2.3)$$

2.2.2 Parameterization of the CKM Matrix

Noting the values of the matrix elements, it is clear that the interactions between quarks from the same generation are strongly favored as opposed to interactions between quarks outside of their generation which are suppressed. Jumping two generations for an interaction, e.g.: a t quark decaying to a d quark, is the most suppressed interaction for each quark.

A representation of the CKM matrix known as the Wolfenstein parameterization [10] is very well suited to demonstrate this empirical behavior over the generations. With this parameterization in hand, the matrix elements can be expanded in powers of four independent parameters, referred to as λ , A , ρ , and η . If the mixing angle between the quark generations is represented by s_{ij} , then in this parameterization

$$\lambda \equiv s_{12}; A \equiv s_{23}/\lambda^2; \rho - i\eta \equiv s_{13}e^{-i\delta_{13}}/A\lambda^3. \quad (2.4)$$

Experimental tests have found $\lambda \approx 0.22$, $A \approx 0.8$, and $\sqrt{\rho^2 + \eta^2} \approx 0.4$. With these parameterization values, the CKM matrix takes the form

$$U = \begin{pmatrix} 1 - \frac{1}{2}\lambda^2 & \lambda & A\lambda^3(\rho - i\eta) \\ -\lambda & 1 - \frac{1}{2}\lambda^2 & A\lambda^2 \\ A\lambda^3(1 - \rho - i\eta) & -A\lambda^2 & 1 \end{pmatrix}. \quad (2.5)$$

In this parameterization, ρ and η represent the CP-violating phase. However, noting that it is always multiplied by λ^3 (where λ is a small fraction), CP-violation in the Standard Model is expected to be small.

2.2.3 The Unitarity Triangle

Previously it was mentioned that the CKM matrix must be unitary ($U^\dagger U = 1$). This requirement leads to six orthogonality relationships [11]:

$$V_{ud}V_{us}^* + V_{cd}V_{cs}^* + V_{td}V_{ts}^* = 0, \quad (2.6)$$

$$V_{us}V_{ub}^* + V_{cs}V_{cb}^* + V_{ts}V_{tb}^* = 0, \quad (2.7)$$

$$V_{ud}V_{ub}^* + V_{cd}V_{cb}^* + V_{td}V_{tb}^* = 0, \quad (2.8)$$

$$V_{ud}V_{cd}^* + V_{us}V_{cs}^* + V_{ub}V_{cb}^* = 0, \quad (2.9)$$

$$V_{cd}V_{td}^* + V_{cs}V_{ts}^* + V_{cb}V_{tb}^* = 0, \quad (2.10)$$

$$V_{ud}V_{td}^* + V_{us}V_{ts}^* + V_{ub}V_{tb}^* = 0. \quad (2.11)$$

These six equations can be represented by six triangles in the complex plane, all of which have the same area. More specifically, each triangle has an area half that of the Jarlskog invariant, $A = |J|/2$ as cited in Ref.[12]. The Jarlskog invariant is an independent phase convention measure of CP violation. While four of the triangles created are very long and thin, the other two are triangles with roughly equal sides, each side of the order λ^3 .

One of those two triangles in question is represented by

$$V_{ud}V_{ub}^* + V_{cd}V_{cb}^* + V_{td}V_{tb}^* = 0. \quad (2.12)$$

This triangle is known as the Unitarity Triangle (see Figure 2.1) and is a very useful visualization of the CKM mechanism. The sides of the triangle have lengths of : $|V_{ud}V_{ub}^*|$, $|V_{td}V_{tb}^*|$ and $|V_{cd}V_{cb}^*|$. The angles within the triangle are

$$\alpha = \arg \left[-\frac{V_{td}V_{tb}^*}{V_{ud}V_{ub}^*} \right]; \beta = \arg \left[-\frac{V_{cd}V_{cb}^*}{V_{td}V_{tb}^*} \right]; \gamma = \arg \left[-\frac{V_{ud}V_{ub}^*}{V_{cd}V_{cb}^*} \right]. \quad (2.13)$$

Also shown in Figure 2.1 is the rescaled Unitarity Triangle which is obtained by aligning the side of the triangle of length $V_{cd}V_{cb}^*$ with the real axis, and then dividing each side by its magnitude, $|V_{cd}V_{cb}^*|$. In doing this two new parameters $\bar{\rho}$ and $\bar{\eta}$ are defined :

$$\bar{\rho} + i\bar{\eta} \equiv -\frac{V_{ud}V_{ub}^*}{V_{cd}V_{cb}^*}, \quad (2.14)$$

$$\bar{\rho} = \rho(1 - \lambda^2/2), \quad (2.15)$$

$$\bar{\eta} = \eta(1 - \lambda^2/2). \quad (2.16)$$

Then, using the above relationships, the angles within the triangle can be defined as

$$\alpha = \tan^{-1} \left(\frac{\bar{\eta}}{\bar{\eta}^2 + \bar{\rho}(\bar{\rho} - 1)} \right), \beta = \tan^{-1} \left(\frac{\bar{\eta}}{1 - \bar{\rho}} \right), \gamma = \tan^{-1} \left(\frac{\bar{\eta}}{\bar{\rho}} \right). \quad (2.17)$$

This unitarity triangle is very useful in visualizing the CKM mechanism, since experimental measurements of the length of each side as well of the angles should be consistent. If, for example, one finds that the triangle doesn't "close", that would be an immediate indication that there is another CP-violating process occurring that the Standard Model is not taking into account. Major efforts by particle physics experiments have been in place to determine these values very precisely.

2.3 Semileptonic B Meson Decays

The measurement presented in this thesis is the lifetime of a B_c^\pm meson, determined by examining its decay to a J/ψ and a μ^\pm , therefore the concept of a semileptonic B decay must be presented. The definition of a B meson is a hadron that contains a \bar{b} quark in a bound state with another quark. There are four ground state B mesons, $B^+(\bar{b}u)$, $B_d^0(\bar{b}d)$, $B_s^0(\bar{b}s)$ and most important for this thesis, $B_c^+(\bar{b}c)$. Of course, there also exist their anti-particle conjugates and charge conjugate models are implied throughout this thesis.

To discuss a B meson decay, it is useful to first examine what happens when a bare b quark decays. This process is shown in Figure 2.2. In the case

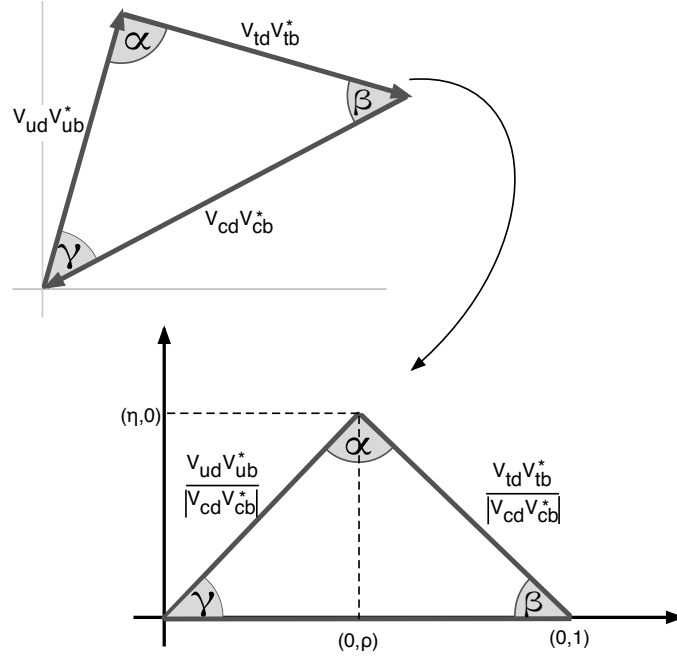


Figure 2.1: Unitarity triangle. The upper portion corresponds to Eqn. 2.9, while the bottom shows the definition of ρ and η , where the triangle has been rescaled dividing each side by $|V_{cd}V_{cb}^*|$.

of a semileptonic b decay, the b -quark decays weakly, emitting a W^- boson on its way to changing flavors and becoming a c quark. The probability for the b quark to make this transition is based on the CKM matrix related to the specific transition, in this case, the value $|V_{cb}|^2$ or $\sim 0.0016\%$.

2.3.1 b -Quark Branching Fraction

In this bare quark model, a naive estimate of the $b \rightarrow c\mu\nu$ branching fraction can be made. For the total decay width of the $b \rightarrow c$, all possible decays of the W must be taken into account:

$$\begin{aligned}
 W &\rightarrow e\nu \\
 W &\rightarrow \mu\nu \\
 W &\rightarrow \tau\nu \\
 W &\rightarrow ud(\times 3 \text{ colors}) \\
 W &\rightarrow cs(\times 3 \text{ colors}).
 \end{aligned} \tag{2.18}$$

Naively, taking the mass of all the possible decay products to be equal, the total branching fraction is roughly

$$Br(b \rightarrow c\mu\nu) \sim \frac{1}{[1 + 1 + 1](\text{leptons}) + [3 + 3](\text{hadrons})} = \frac{1}{9} = 11\%. \tag{2.19}$$

However, for hadrons, this is naive because it ignores the fact that the quarks that are bound together within the initial meson interact with each other. It should be noted that in the case of the B_c^\pm meson, the other quark in the meson is a c quark which can also decay weakly while the b quark spectates

and thus there is another semileptonic channel. This will be discussed in more detail in Section 2.4.4 where the theory of B_c^\pm decays will be discussed.

2.3.2 b -Quark Lifetime

Due to its large mass, the bare b quark lifetime calculation is comparable to muon decay, see Figure 2.3, and so we can first look at this process.

In general the decay rate can be obtained with the following:

$$d\Gamma = \frac{1}{2E} |\overline{\mathcal{M}}|^2 dQ \quad (2.20)$$

where \mathcal{M} is the amplitude, dQ is the invariant phase space and E is the energy. Looking first at the \mathcal{M} term we can find this is equal to :

$$\mathcal{M} = \frac{G_F}{\sqrt{2}} [\bar{u}(k)\gamma^\mu(1 - \gamma^5)u(p)] [\bar{u}(p')\gamma_\mu(1 - \gamma^5)u(k')] . \quad (2.21)$$

where G_F is the Fermi coupling constant.

After performing the integration and solving for Γ , we find that

$$\Gamma \equiv \frac{1}{\tau} = \int_0^{m/2} dE' \frac{d\Gamma}{dE'} = \frac{G_F^2 m_\mu^5}{192\pi^3} \cdot F(x) \quad (2.22)$$

where, G_F is the Fermi coupling constant, m_μ is the mass of the muon, and $F(x)$ is a phase space correction and given by, $F(x) = 1 - 8x + 8x^3 - x^4 - 12x^2 \ln(x)$, where $x = \frac{m_e^2}{m_\mu^2}$.

While this is correct for the muon decay, there are additional terms that are needed when discussing the b quark decay. The vertex of the b -quark decay to the c (or u) quark must include the CKM matrix element $|V_{cb}|$ or $|V_{ub}|$. However, the decay to a u quark is heavily suppressed due to the fact that the matrix element as seen in Equation 2.3 is two generations away. The W boson associated with this vertex can then decay to lighter quark pairs (\bar{u}, d) or (\bar{c}, s) . It can also decay to a lepton pair $(\ell, \bar{\nu}_\ell)$. There is a large phase space available in the b quark decay and thus all these decays are possible. Therefore when we take all of this into account we find:

$$\Gamma(b \rightarrow cW^-) = \frac{G_F^2 m_b^5}{192\pi^3} f_{cb} |V_{cb}|^2 \sum (3|V_{q_i q_j}|^2 \cdot f_{q_i q_j} + f_{\ell\nu_\ell}). \quad (2.23)$$

The summation is over the final states in the W decay, the f terms are phase space correction factors and the multiplicative factor of 3 is due to the color freedom in decays to quark pairs. Notice also that the mass term is now the mass of the b -quark rather than the muon.

If we plug in values and ignore the partial width from the annihilation $(\ell\nu_\ell)$ channel from the W decay, we can estimate the order of magnitude lifetime of a bare b quark, namely using: $G_F \simeq 1.17 \times 10^{-5} / \text{GeV}^2$, $m_b \simeq 5$ GeV, and $V_{cb} \simeq 0.04$ (from Equation 2.2) and $f_{q_1 q_2}(x) = F(x)$ (mentioned

previously), where $x = \frac{m_{q1}^2}{m_{q2}^2}$ [3]:

$$\begin{aligned}
 \Gamma_b = \frac{1}{\tau_b} &\simeq \frac{G_F^2 m_b^5}{192\pi^3} f_{cb} |V_{cb}|^2 \cdot (3|V_{ud}|^2 \cdot f_{ud} + 3|V_{cs}|^2 \cdot f_{sc}) \\
 &\simeq \frac{(1 \times 10^{-5}/\text{GeV}^2)^2 \cdot (4.5 \text{ GeV})^5}{192\pi^3} \cdot |0.04|^2 \cdot f_{cb}(x) \\
 &\quad \cdot (3|0.97|^2 \cdot f_{ud}(x) + 3|0.97|^2 \cdot f_{sc}(x)) \\
 &\simeq 2 \times 10^{-13} \text{ GeV} \quad (2.24)
 \end{aligned}$$

Using the natural units conversion of $1 \text{ GeV} = 1.5 \times 10^{24} \text{ s}^{-1}$ we can convert Equation 2.24 to picoseconds and thus get an estimate of the bare b -quark lifetime of $\sim 3 \text{ ps}$. This of course will change significantly when effects of the other quark(s) in the hadron are taken into account and so this estimate is high for the lifetime of the b -quark, which in actuality is $\sim 1.5 \text{ ps}$.

2.4 B_c^\pm Meson

The B_c^\pm meson is unique in that it is made up of two heavy quarks. This fact alone does not make it unique because the two heavy quarkonia states, charmonium ($c\bar{c}$) and bottomonium ($b\bar{b}$) carry two heavy quarks as well. The difference is that it carries two *different* heavy quarks and decays weakly, whereas quarkonia decay strongly. Due to this make-up, the B_c^\pm meson is one of the most interesting hadrons to study. As it is a carrier of

flavor, another window of study into heavy-quark dynamics can be achieved.

The following sections will delve deeper into the characteristics of the B_c^\pm meson. First the spectroscopy of the $(c\bar{b})$ system will be covered, followed by B_c^\pm meson production and concluding with theoretical discussions of the B_c^\pm lifetime and its decay rates.

2.4.1 Spectroscopy

The family of mesons that exist within the $\bar{b}c$ system provide a rich spectroscopy of orbital and angular momentum excitations. For the $\bar{b}c$ system, it would be advantageous to use potentials that do not depend on the flavor of the constituent quarks for its predictions since the B_c^\pm meson is a flavor-carrying particle. This can be done using a relativized quark model and is done in Ref. [13]. In this model, the authors take into account most relativistic effects, include the running constant of QCD $\alpha(Q^2)$ and is based on some variant of the Coulomb plus linear potential that is expected from QCD. In the relativized quark model, mesons are approximated by the $q\bar{q}$ sector of Fock space. Doing this in effect integrates out the degrees of freedom below some distance scale μ^{-1} .

The results of this theoretical prediction can be seen in the spectrum in

Fig 2.4. Note in the figure, the BD threshold is labeled. The states that lie below this threshold, namely $M_{(states)} < M_D + M_B$, are stable against fission into heavy-light mesons. These excited states cascade down through the spectrum until they reach the ground state via hadronic or electromagnetic transitions. The B_c^\pm ground state will decay via the weak interaction and will be looked at in more detail in upcoming sections.

2.4.2 Mass

While the work presented in this thesis will not be a measurement of the mass of the B_c^\pm meson, it is important for the measurement as will be seen in Chapter 5. The most precise theoretical calculation comes from a three-flavor (unquenched) lattice QCD numerical algorithm that yields: $M(B_c) = 6304 \pm 12_{-0}^{+18}$ MeV/ c^2 . This is in agreement with CDF's measurement of $M(B_c) = 6275.6 \pm 2.9 (stat) \pm 2.5 (sys)$ MeV/ c^2 [46] and the DØ experiment's measurement of $M(B_c) = 6300 \pm 14 (stat) \pm 5 (sys)$ MeV/ c^2 [47]. For this analysis, the mass measured by CDF will be used throughout as it is the most precise value obtained by experimental methods and the DØ mass result was not available at the time of this analysis.

A review of the different mass measurements is given in Table 2.4.

Table 2.4: Theoretical and experimental values of the B_c^\pm mass.

Lattice QCD	$6304 \pm 12_{-0}^{+18} \text{ MeV}/c^2$
CDF	$6275.6 \pm 2.9 (stat) \pm 2.5 (sys) \text{ MeV}/c^2$
DØ	$6300 \pm 14 (stat) \pm 5 (sys) \text{ MeV}/c^2$

2.4.3 Production

To successfully measure the lifetime of the B_c^\pm meson, a B_c^\pm meson must of course first be produced. The production can be thought of in three steps [14]:

1. A \bar{b} and c are created in a parton collision. These quarks need to have small relative momentum with respect to each other.
2. These two quarks bind and thus form the B_c^\pm or one of it's excited states. Note that to obtain a ground-state B_c^\pm meson the produced state must be below the BD threshold.
3. The states that are excited versions of the B_c^\pm will then cascade down to the ground state via hadronic or electromagnetic transitions.

To calculate the B_c^\pm total production cross section, the direct production cross section for B_c^\pm and it's excited states must be summed.

Using an effective field theory called *nonrelativistic* QCD or NRQCD, the direct production of the B_c^\pm and other $\bar{b}c$ mesons can be calculated. The reason this approach is taken in describing the B_c^\pm is because heavy quarkonia are, to a good approximation, nonrelativistic bound states consisting of a heavy quark and anti-quark. It is because the mass of the heavy quark m_Q is large that NRQCD is useful as a description.

Production of heavy quarkonia begins with hard scattering, in turn creating a heavy quark-antiquark pair which is in an angular momentum and color state. This will be denoted as $\bar{b}c(n)$. The color singlet state is denoted by $(\bar{b}c(1))$, while $(\bar{b}c(8))$ represents the color-octet state. By standard spectroscopic notation, $^{2S+1}L_J$ is the angular momentum state denotation. The $\bar{b}c$ state transitions into the final quarkonia state H in a way that can be described by the NRQCD theory.

The mathematical picture of the above is shown in the NRQCD factorization formula. The inclusive differential cross section for producing a B_c^\pm state in a proton-antiproton collision can be written as

$$d\sigma[p + \bar{p} \rightarrow H + X] = \sum_{ij} \int dx_1 dx_2 f_{i/p}(x_1) f_{j/\bar{p}}(x_2) d\sigma[ij \rightarrow H + X]. \quad (2.25)$$

The functions $f_{k/A}$ are the parton distribution functions and the sum is over the partons i and j in the initial state hadrons. The cross section $d\sigma[ij \rightarrow$

$H + X]$, which is the direct production of H by the collisions of partons i and j , can be written as the sum of products of short-distance cross sections and long-distance matrix elements

$$d\sigma[ij \rightarrow H + X] = \sum_n d\hat{\sigma}[ij \rightarrow \bar{b}c(n) + X] \langle O^H(n) \rangle. \quad (2.26)$$

In the above equation, $d\hat{\sigma}[ij \rightarrow \bar{b}c(n) + X]$ is the short distance cross section for creating the $\bar{b}c$ in the color and angular momentum state n , and it can be calculated as a perturbative expansion in α_s at scales of m_c or larger.

The long-distance matrix element $\langle O^H(n) \rangle$ is nonperturbative and it encodes the probability for a $\bar{b}c$ in the state n to bind and form the meson H . This matrix element scales by the relative velocity v of the charm quark. The leading color-octet matrix element in the S-wave states is suppressed by v^4 to the leading color-singlet element. Similarly, for the P-wave states both the leading color-singlet and color-octet matrix elements are suppressed by a factor of v^2 to the leading color-singlet matrix element in the S-waves.

The above treatment for $\bar{b}c$ is very similar to the production of bottomonium or charmonium; however, it differs in an essential point. In $\bar{b}c$ production *two* heavy quark-antiquark pairs must be produced in the collision, whereas for $b\bar{b}$ and $c\bar{c}$ only one pair must be produced. For a $b\bar{b}$ pair, it is created at the order of α_s^2 by the parton process $q\bar{q}, gg \rightarrow b\bar{b}$. However, look-

ing at $\bar{b}c$, the lowest order mechanism is on the order α_s^4 with the processes being $q\bar{q}, gg \rightarrow (\bar{b}c) + b\bar{c}$. One can also think of this processes sequentially, i.e., $gg \rightarrow b\bar{b}$ and then a subsequent gluon radiated off of any quark then splits to $c\bar{c}$, $g \rightarrow c\bar{c}$. At hadronic colliders, the gg component dominates and the process can create the $\bar{b}c$ in either the color-singlet or color-octet state.

Given the suppression of the color-octet matrix elements these contributions can be ignored to leading order in the calculation of the cross sections of a $\bar{b}c$ meson. Therefore all existing calculations for this have been carried out within the color-singlet model [19]. The cross sections are proportional to $\alpha_s^4(\mu)$ as well as to a wave function factor. The part of this calculation that is the most difficult and the most ambiguous is the choice of the scale μ . The reason for this is that the short distance process involves several scales, including m_c , m_b , and p_T . An example of this problem can be seen when μ varies from m_c up to $2(m_c + m_b)$. When this variation is made, the cross section of $\bar{b}c$ changes by a factor of 7 [19].

The cross section for the B_c^\pm meson is three orders of magnitude smaller than that of other B mesons due to the presence of two pairs of quarks and antiquarks in the final state. Due to this lower production cross section, only at high energy hadronic colliders with high luminosity such as the Tevatron

can one collect enough B_c^\pm events to make possible strides in experimental studies.

$p_T(B_c)$ Distribution

In hadronic production of S-wave and P-wave $\bar{b}c$ mesons via heavy quark fragmentation, the differential cross section $d\sigma/dp_T$ versus the transverse momentum of any ($\bar{b}c$) state, denoted by H , can be written as shown in Ref. [20]:

$$\begin{aligned} \frac{d\sigma}{dp_T}(p\bar{p} \rightarrow H(p_T)X) &= \sum_{ij} dx_1 dx_2 dz f_{i/p}(x_1, \mu) f_{j/\bar{p}}(x_2, \mu) \quad (2.27) \\ & \left[\frac{d\hat{\sigma}}{dp_T}(ij \rightarrow \bar{b}(p_T/z)X, \mu) \times D_{\bar{b} \rightarrow H}(z, \mu) + \right. \\ & \left. \frac{d\hat{\sigma}}{dp_T}(ij \rightarrow g(p_T/z)X, \mu) D_{g \rightarrow H}(z, \mu) \right] \end{aligned}$$

where the $f_{i/p\bar{p}}(x, \mu)$'s are the parton distribution functions, $d\hat{\sigma}$'s are the sub-process cross section, and $D_{i \rightarrow H}(z, \mu)$'s are the parton fragmentation functions at the scale μ .

The physical interpretation of the above is that a heavy \bar{b} antiquark or a gluon is produced in a hard process with a transverse momentum p_T/z and it fragments into hadron H carrying longitudinal momentum fraction z . Although the physics production rates should be independent of the choice of the scale μ , it is not because that can only be achieved if both the production

of the high energy partons and the fragmentation functions are calculated to all orders in α_s . The dependence on μ can be estimated by varying the scale $\mu = (0.5 - 2)\mu_R$, where μ_R is the primary choice of scale:

$$\mu_R = \sqrt{p_T^2(\text{parton}) + m_b^2}. \quad (2.28)$$

Due to this uncertainty on the factorization scale μ , there is an uncertainty on the $p_T(B_c)$. See Figure 2.5 which shows the dependence of the differential cross sections for the various choices of $\mu = \mu_R/2$ for the 1^1S_0 and 1^3P_0 states. The $\mu = 2\mu_R$ shows that the differential cross section increases only slightly at the low p_T region and vice versa for the high p_T region. While the $\mu = \mu_R/2$ curve shows a larger dependence, the variations are always within a factor of two.

These variations in the $p_T(B_c)$ will be taken into account as a source of systematic uncertainties and described in Section 6.1.3.

2.4.4 Theory of B_c^\pm Decays

It all started with Bjorken's pioneering paper in 1986 [21]. That paper presented the first predictions for hadrons composed of heavy quarks, including those with two heavy quarks such as the B_c^\pm . There has been a large effort in the past decade or so to get a better handle on doubly heavy hadrons

using the theoretical tools of Operator Product Expansion (OPE), sum rules (SR) of QCD, as well as potential models (PM) that have been adjusted using data from hadrons with a single heavy quark. Surprising, or maybe not, the initial predictions by Bjorken are very close to the results obtained using stricter methods.

In studying the B_c^\pm meson theoretically, there are two advantageous features: the non-relativistic motion of the \bar{b} and c quark and, given that there are two heavy quarks within the meson, the suppression of the light quark-antiquark. These two physical conditions lead to two expansion parameters: the relative velocity v of the quarks, and the ratio of the confinement scale to the mass of the heavy quark, λ_{QCD}/m_Q . In this section, the lifetime and decay rates of the B_c^\pm meson are explored giving the reader a taste of the physics accompanying this meson.

When a B_c^\pm meson decays, there are three paths it can take :

- The \bar{b} quark decays and the c -quark is a spectator, see Figure 2.6(a).
- The c -quark decays while the \bar{b} -quark spectates, see Figure 2.6(b).
- The \bar{b} and c can participate in annihilation decays of the order

$$\bar{b}c \rightarrow \ell^+\nu_\ell, c\bar{s}, u\bar{s} \text{ where } \ell = e, \mu, \tau. \text{ See Figure 2.6(c).}$$

In the first case, the specific process $\bar{b} \rightarrow \bar{c} + c\bar{s}$ (where the $c\bar{s}$ is the product resulting from the W^+ decay) must be separated in the total width calculation due to the Pauli Interference (PI) with the charm quark from the initial state [22].

The total width of the B_c^\pm is the sum of the partial decay widths coming from the above three decay possibilities and accordingly written as:

$$\Gamma(B_c \rightarrow X) = \Gamma(b \rightarrow X) + \Gamma(c \rightarrow X) + \Gamma(ann.) + \Gamma(PI), \quad (2.29)$$

and the lifetime of the B_c^\pm meson is determined by

$$\tau(B_c) = \frac{1}{\Gamma(B_c \rightarrow X)}. \quad (2.30)$$

Due to the three different possible decay channels, the B_c^\pm meson has an expected lifetime that is roughly one third shorter than other B hadrons. The expected contributions for each decay path can be calculated using several different theoretical models. The ratio of each decay, as predicted by the various theoretical models, is given in Table 2.5. These theoretical models will be discussed in more detail in the following text.

Annihilation Decays

Considering the annihilation decay, the width ($\Gamma(ann.)$) is the sum of the widths from the $\bar{b}c$ annihilating into a W^+ and then into quarks and leptons.

Table 2.5: B_c^\pm branching ratio percentages calculated in various theoretical approaches. (Ref. [22]).

B_c^\pm Decay Mode	Operator Product Expansion	Potential Models	Sum Rules
$\sum \bar{b} \rightarrow \bar{c}$	25.0 ± 6.2	25.0 ± 6.2	19.6 ± 1.9
$\sum c \rightarrow b$	64.3 ± 16.1	65.6 ± 16.4	72.0 ± 7.2
$B_c^+ \rightarrow \tau^+ \nu_\tau$	2.9 ± 0.7	2.0 ± 0.5	1.8 ± 0.2
$B_c^+ \rightarrow c \bar{s}$	7.2 ± 1.8	7.2 ± 1.8	6.6 ± 0.7

For the quark decay modes, hard gluon corrections to the effective four-quark interaction of weak currents must be taken into account and result in a correction factor of $a_1 = 1.22 \pm 0.04$ [22]. The calculation of this contribution does not depend on a hadronization model because there is a large energy release on the order of the meson itself. The width of this mode can be written as [22]:

$$\Gamma(ann.) = \sum_{i=\tau,c} \frac{G_F^2}{8\pi} |V_{bc}|^2 f_{B_c}^2 M m_i^2 \left(1 - \frac{m_i^2}{m_{B_c}^2}\right)^2 \cdot C_i, \quad (2.31)$$

where G_F is the Fermi coupling constant, f_{B_c} is the leptonic constant ~ 400 MeV, $C_\tau = 1$ for the $\tau^+ \nu_\tau$ channel and $C_s = 3|V_{cs}|^2 a_1^2$ for the $c\bar{s}$ -channel. In the expression above, note that the decay width is proportional to the square of the masses of the leptons and quarks in the final state and so the contribution from light leptons and quarks can be neglected, leaving only the

$\bar{b}c \rightarrow \tau^+ \nu_\tau$ and $\bar{b}c \rightarrow c\bar{s}$ final states as non-negligible contributors.

Non-Annihilation Decays

For the non-annihilation decays, QCD corrections need to be applied and three different theoretical models take three different approaches. These are covered in the following three sections.

A. OPERATOR PRODUCT EXPANSION

The approach of Operator Product Expansion (OPE) [23] for the quark currents of weak decays can be applied for these types of decays. In this approach, the α_s -corrections to the free quark decays are taken into account and it uses the Star Trek sounding “quark-hadron duality” for the final states. Applying the transition operator matrix element for the bound-state meson accounts for effects caused by the motion and virtuality of the decay quark inside the meson due to its interaction with the spectator. As a result Pauli Interference is almost entirely suppressed. Similarly, the c -quark decays with a spectator b quark are suppressed when compared to a *free* c -quark decay due to the large bound energy in the initial state.

Using OPE to determine the decay width, in accordance with the optical theorem, the total width Γ_H (where H is the B_c^\pm meson) has the form [23]:

$$\Gamma_H = \frac{1}{2M_H} \langle H | \mathcal{T} | H \rangle, \quad (2.32)$$

where \mathcal{T} is defined as the transition operator matrix element,

In the weak decay of either the b or c quark, the energy release is large when compared to the scale of the bound-state dynamics. For this reason, the OPE approach can be expanded in inverse powers of heavy-quark mass and thus the quantity \mathcal{T} in Equation 2.32 has the form:

$$\mathcal{T} = \sum_{i=1}^2 \left\{ C_1(\mu) \bar{Q}^i Q^i + \frac{1}{m_{Q^i}^2} C_2(\mu) \bar{Q}^i g \sigma_{\mu\nu} G^{\mu\nu} Q^i + \frac{1}{m_{Q^i}^3} O(1) \right\}, \quad (2.33)$$

where Q marks the flavor of the heavy quark (b or c). The leading contribution is given by the spectator decay, $\bar{Q}Q$, and is an operator of dimension 3. The corrections to the spectator decays is given by $\bar{Q}^i g \sigma_{\mu\nu} G^{\mu\nu} Q^i$ which is an operator of dimension 5.

The OPE calculations have a strong dependence on the quark mass values as seen above. However, the lifetime dependence on the b -quark mass can be eliminated by the relation [23]:

$$m_b = m_c + 3.5 \text{ GeV}. \quad (2.34)$$

The above heavy quark mass relation comes from the fact that for any value of m_c , m_b is obtained by matching the results of the B_d meson lifetime calculation to that of the experimentally measured value of $\tau_{B_d} = 1.55$ ps. The OPE method, however, is still very reliant on the c -quark mass and thus the results of the theory change accordingly. See Table 2.6 for a list of widths as well as lifetime predictions for various values of c -quark mass choice. Note the large changes in lifetime predictions when the c -quark mass value is varied.

Table 2.6: B_c^\pm lifetime and width predictions for various c -quark mass choices [23]. The partial widths are listed in ps^{-1} and the lifetimes in ps.

Parameters, GeV	$\sum \bar{b} \rightarrow \bar{c}$	$\sum c \rightarrow s$	PI	Ann	τ_{B_c}
$m_b = 5.0, m_c = 1.5, m_s = 0.20$	0.694	1.148	-0.115	0.193	0.54
$m_b = 4.8, m_c = 1.35, m_s = 0.15$	0.576	0.725	-0.132	0.168	0.75
$m_b = 5.1, m_c = 1.6, m_s = 0.45$	0.635	1.033	-0.101	0.210	0.55
$m_b = 5.1, m_c = 1.6, m_s = 0.20$	0.626	1.605	-0.101	0.210	0.43
$m_b = 5.05, m_c = 1.55, m_s = 0.20$	0.623	1.323	-0.107	0.201	0.48
$m_b = 5.0, m_c = 1.5, m_s = 0.15$	0.620	1.204	-0.114	0.193	0.53

B. POTENTIAL MODELS

In the approach of another theoretical basis, Potential Models (PM), it is necessary to sum up widths of exclusive decay modes [24] in order to obtain

an inclusive decay rate. In semileptonic decays, i.e., the $\bar{b} \rightarrow \bar{c}\ell^+\nu_\ell$ and $c \rightarrow s\ell^+\nu_\ell$ transitions, the final hadronic states are dominated by the lightest bound $1S$ -states, the $(c\bar{c})$ -system is dominated by η_c and J/ψ particles and the $(\bar{b}s)$ -system by B_s and B_s^* .

The total widths calculated in the inclusive OPE method and the inclusive PM method, where the widths are exclusively calculated and then summed, prove to be consistent with each other if the most significant uncertainty related to the choice of quark masses (as seen previously with the charm quark mass) is taken into account. The final result is then

$$\tau[B_c^+]_{\text{OPE, PM}} = 0.55 \pm 0.15 \text{ ps.} \quad (2.35)$$

C. QCD SUM RULES

Another theoretical approach is that of QCD sum rules (SR) [22, 25]. In contrast to the OPE method, where the largest uncertainty is the variation of the heavy quark masses, in SR these parameters are fixed by the two-point sum rules for bottomonia and charmonia. Also, by using the factorization, the semileptonic and hadronic decay modes can be related.

In the $\bar{b}c$ system, as mentioned previously, the relative velocity of the quark movement is small. Due to this fact, the Coulomb-like α_s/v corrections become front and center in importance in the semileptonic decay modes.

These corrections can be described by the ladder diagram depicted in Figure 2.7. In QCD sum rules, this leads to the finite renormalization for ρ_i , so that [25]:

$$\rho_i^c = \mathcal{C} \rho_i, \quad (2.36)$$

where

$$\mathcal{C}^2 = \left| \frac{\Psi_{bc}^c(0)}{\Psi_{bc}^{\text{free}}(0)} \right|^2 = \frac{4\pi\alpha_s^c}{3v} \frac{1}{1 - \exp\left(-\frac{4\pi\alpha_s^c}{3v}\right)}. \quad (2.37)$$

In this heavy quarkonia system, v is the relative velocity of the quarks

$$v = \sqrt{1 - \frac{4m_b m_c}{p_1^2 - (m_b - m_c)^2}}. \quad (2.38)$$

The coupling constant of effective coulomb interactions, α_s^c , is found by the calculation of leptonic constants for the appropriate heavy quarkonia and can be found in more detail in Ref. [25].

In QCD Sum Rules, the accuracy of the prediction for the total width of the B_c^\pm is determined by the choice of the scale μ for the hadronic weak lagrangian in decays of charm quarks. This dependence can be seen in Fig. 2.8. Assuming the preferred choice $\mu_{B_c}^2 \sim (0.85 \text{ GeV})^2$ [25] in the $c \rightarrow s$ decays of B_c^\pm , then in the framework of the semi-inclusive SR calculation it is found that

$$\tau[B_c^+]_{SR} = 0.48 \pm 0.05 \text{ ps}. \quad (2.39)$$

Note that in the sum rules approach the error is much smaller due to the fact that the ambiguity of the quark mass choice is not involved in the calculation.

Isgur-Wise Model, ISGW2

The kinematics of the B_c^\pm decay, i.e., the angles and energies of the decay products in the rest frame of the B_c^\pm , is described by the Isgur-Wise model. We use this model to get the distributions needed for the Monte Carlo samples that are used throughout the analysis. The absolute scale of partial widths and total width, Γ , and hence lifetime, is predicted in the previously discussed theories. This is being measured in the analysis and thus a precise value is not needed for the simulations.. To discuss the ISGW2 model, the Heavy Quark Effective Theory (HQET) [15, 16, 18] must first be described. HQET is a theory that can be applied in a situation where one of the quarks in the meson is heavy and the other is light. These cases are where $m_Q \gg \Lambda_{QCD}$, where m_Q is the mass of the heavy quark and Λ_{QCD} is the scale of the constituent mass of a light quark (i.e. $\approx 200 \text{ MeV}/c^2$). Quarks that can be used here are top, bottom and charm and are taken to have infinite mass in the calculations. However, they don't actually have infinite mass and so it is necessary to apply perturbative $\frac{1}{m_Q}$ corrections to

the initial approximation. One of the theoretical applications to these corrections is ISGW2 which is the theory used as the decay model in the Monte Carlo samples used in this analysis.

ISGW2 is an update to the original model, but would appropriately reflect advances in the field of the Heavy Quark Symmetry [17]. Additions to the model include:

- heavy quark symmetry constraints on the relations between form factors as well as the slopes of the form factors away from zero-recoil;
- relating the naive currents of the quark model to the full weak currents via HQET;
- heavy-quark-symmetry-breaking color magnetic interactions are included;
- modification of connection of quark model form factors to physics form factors so that there would be consistency with heavy quark symmetry break at the order of $\frac{1}{m_Q}$;
- relativistic corrections are taken into account; and
- more realistic form factor shapes are employed.

Lifetime Predictions

To summarize, the lifetime of the B_c^\pm meson is predicted in three different theoretical models. The OPE method and the PM agree when you take into account the uncertainty due to the quark masses. The QCD Sum Rules method has smaller errors on the prediction due to the fact that the quark masses are not involved in its prediction. The predictions for the two are summarized in Table 2.7.

Table 2.7: Lifetime predictions for the B_c^\pm meson.

Theoretical Model	$\tau(B_c)$ (ps)
OPE & PM	0.55 ± 0.15
QCD Sum Rules	0.48 ± 0.05

2.4.5 Discussion and Conclusions

The previous sections presented a brief summary of the theoretical predictions of the B_c^\pm meson's properties. The first topic discussed was the mass and spectroscopic properties of the B_c^\pm meson, and it was found that there are many levels in the $\bar{b}c$ system above the ground state. A prediction of the ground state mass were given. Those states that are below the BD threshold are stable against fission and thus cascade down to the ground state via

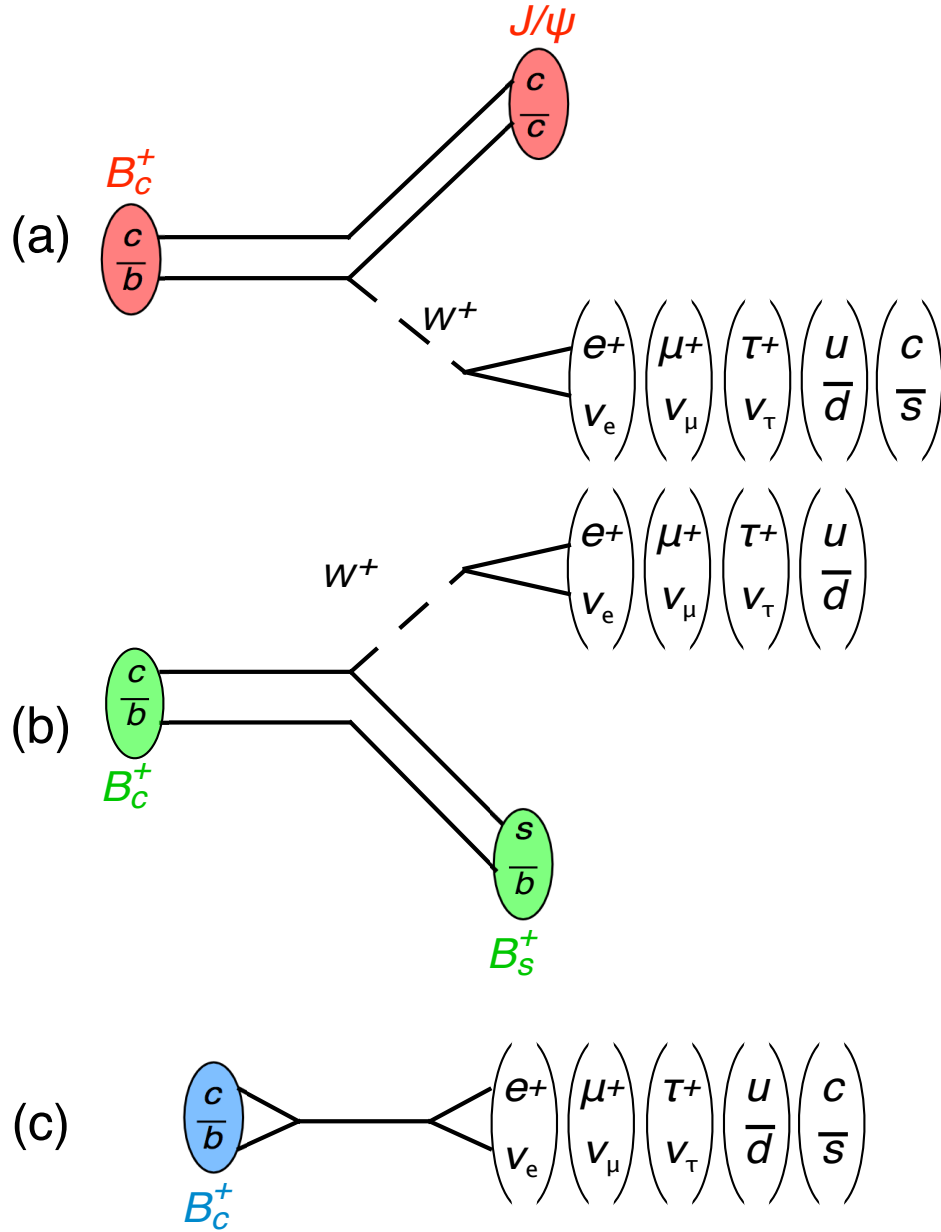
hadronic or electromagnetic transitions. The production mechanisms of the B_c^\pm meson and the NRQCD framework were also discussed.

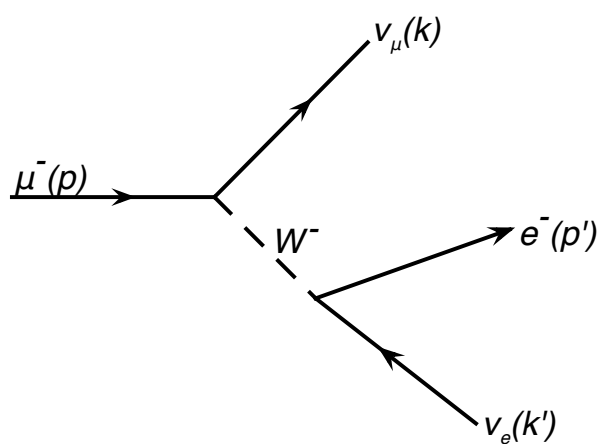
The chapter concluded with a discussion of the B_c^\pm decay rates and lifetime predictions. There are three different possible decay paths and that each one contributes to the lifetime. The dominant contribution to the B_c^\pm lifetime is from charm quark decays, contributing roughly 70% to the total. The other two modes, b quark decay and annihilation contribution about 20% and 10% respectively. Finally there was a more detailed discussion of the annihilation modes versus the non-annihilation modes and the lifetime predictions were summarized. The QCD Sum Rules prediction had the smallest errors due to the non-involvement of the quark masses in the theoretical calculation.

2.5 Motivation for this Measurement

This thesis is a presentation of the measurement of the B_c^\pm lifetime in the channel $B_c^\pm \rightarrow J/\psi\mu^\pm + X$. The decay products in this decay mode make for a decay which is ideal for detection in the DØ detector. Due to the three possible decay chains, the B_c^\pm meson lifetime is expected to be roughly a third smaller than its B hadron relatives, a prediction which will be tested

in this thesis. The B_c^\pm meson lifetime will be shown to be in agreement with the theoretical predictions presented here.

Figure 2.2: Free b quark decay.

Figure 2.3: μ decay.

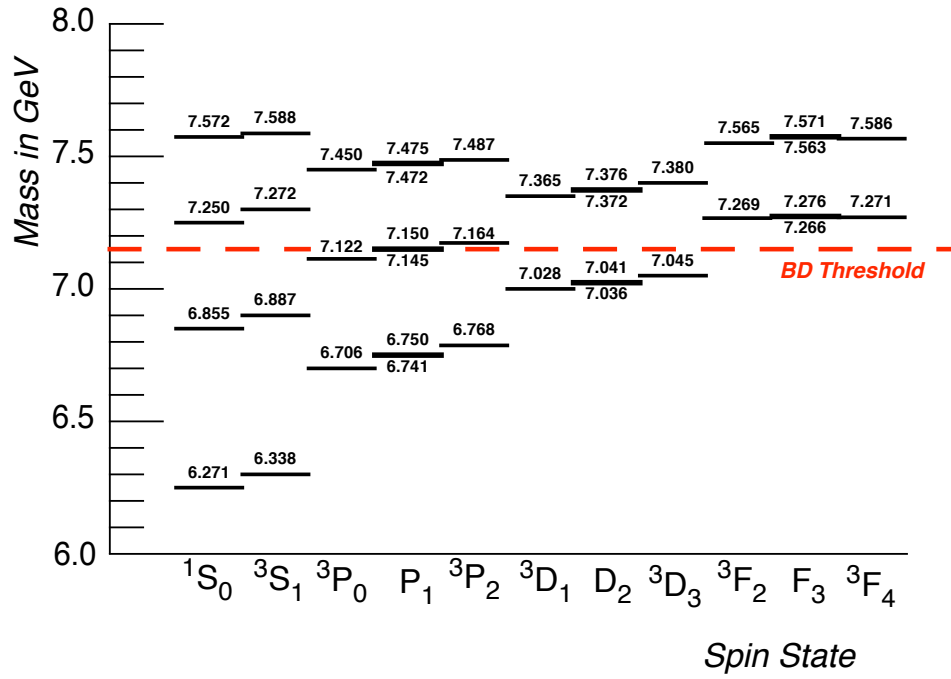


Figure 2.4: The B_c^\pm mass spectrum (from Ref. [13].)

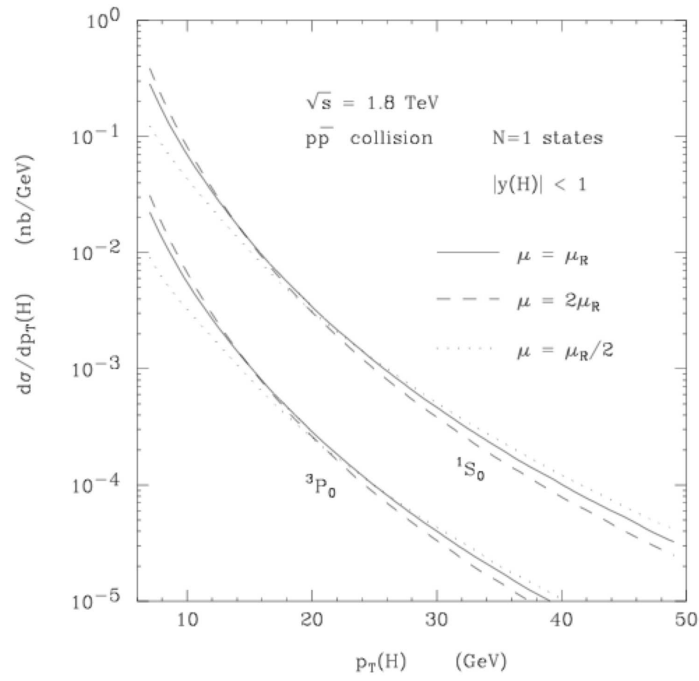


Figure 2.5: The dependence of the differential cross section on the factorization scale μ (Ref [20]).

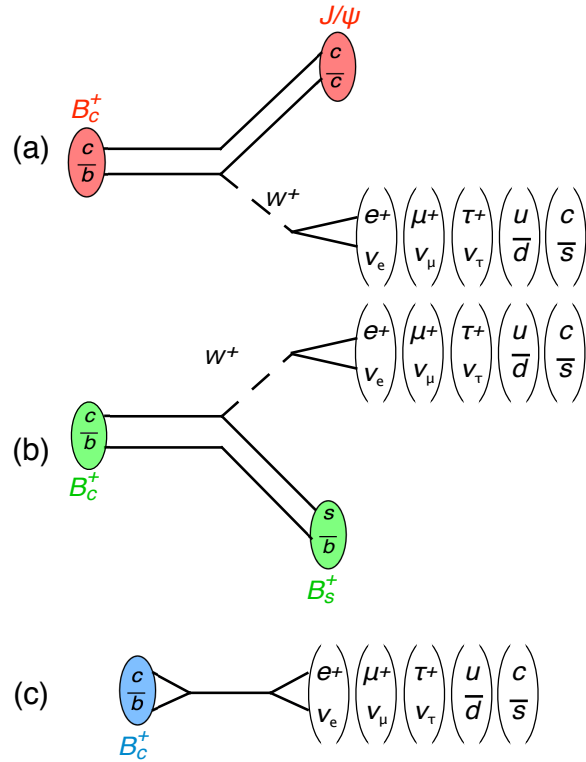


Figure 2.6: The three possible decay paths of the B_c^+ meson.

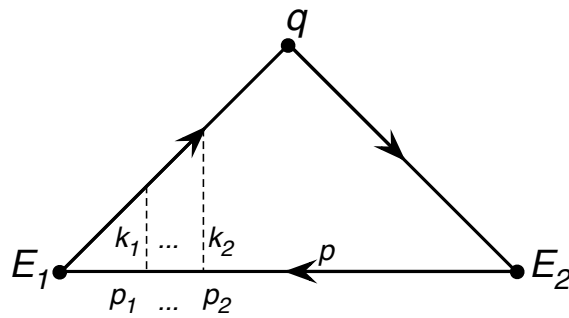


Figure 2.7: Ladder diagram of the Coulomb-like interaction

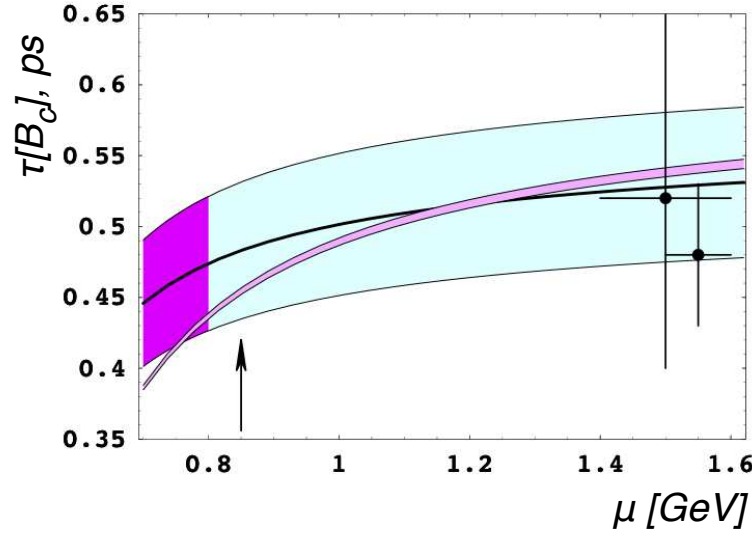


Figure 2.8: The B_c^\pm lifetime predictions as calculated by QCD Sum Rules versus the scale of the hadronic weak lagrangian in the decays of the charm quark. The arrow depicts the preferred choice for $\mu = 0.85$ as determined in Ref. [25]. The wide-light blue shaded region shows uncertainties of semi-inclusive estimates. The dark purple shaded region is the preferable choice determined by charm quark lifetimes. The thin shaded band represents the result obtained by summing up exclusive channels in the decays of \bar{b} . The data points with error bars represent the solutions from the OPE approach [23]

Chapter 3

Experimental Apparatus

“For a successful technology, reality must take precedence over public relations, for nature cannot be fooled.” – Richard Feynman

“It is difficult not to wonder whether that combination of elements which produces a machine for labor does not create also a soul of sorts, a dull resentful metallic will, which can rebel at times.” –Pearl S. Buck

3.1 The Tevatron Accelerator Complex

The Fermi National Laboratory (FNAL) is located about 45 miles west of downtown Chicago. It is here that the Tevatron complex [37, 38] is located. At the time of this writing, the Tevatron is the highest energy collider in the

world, and will be until the Large Hadron Collider (LHC) begins operating at CERN. The Tevatron delivers proton-antiproton collisions at center-of-mass energies of $\sqrt{s}=1.96$ TeV every 396 ns. Figure 3.1 shows a schematic view of the Fermilab accelerator complex and also the location of our $D\bar{O}$ detector.

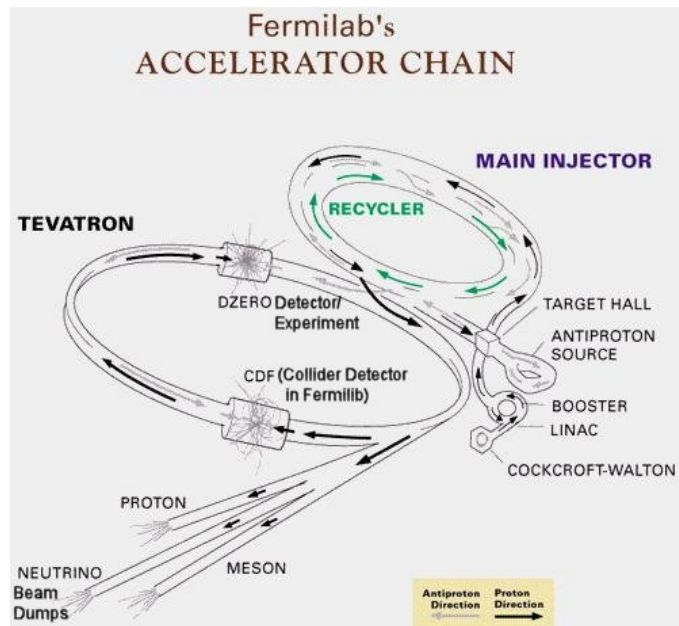


Figure 3.1: Fermilab Accelerator Complex.

3.1.1 Proton Production and Acceleration

Creating Protons

The first step in the process is to create the proton beam. This begins with a negative hydrogen ion (H^-) beam that is created from a magnetron

surface-plasma source. After the beam is created, it is accelerated to an energy of 750 keV by the Crockcroft-Walton Pre-Accelerator. From here the H^- beam is sent onto the linear accelerator (Linac). The hydrogen ions are bunched together in the Linac, and then boosted to 400 MeV and sent into the Booster. Before they hit the Booster, however, they are sent through a carbon foil that strips the electron from the H^- 's, thus leaving bare protons. The pure proton beam then continues into the Booster where it remains, until it reaches an energy of 8 GeV. At this point the protons move into the Main Injector.

Main Injector

There are two purposes to the Main Injector [39] section of the accelerator chain. The first is to accelerate the protons to 120 GeV for passing to the Antiproton source. The second is accelerating the pure proton beam to 150 GeV and collecting them into bunches before injecting them into the Tevatron. The Main Injector was one of the main upgrades added to the Tevatron complex during a shut down period from 1996 to 2001. The period after this shut down is known as Run II, and due to the Main Injector, three times as many protons can be injected into the Tevatron as compared to the Main Ring from Run I (that is defined as the data taking period between

1992 and 1996).

For the protons that take the path to the Antiproton source, they are first fired onto a nickel target that results in the production of antiprotons, see [40] for more details on this process. It's not an efficient process however, since for every one million protons that hit the target, approximately 20 antiprotons are produced. After the antiprotons are generated, they are sent to the Debuncher where they go through a process known as stochastic cooling to reduce the momentum spread of the antiprotons. From here the antiprotons travel to the Accumulator. Since so few antiprotons are created at a time, they are stored here until there is an adequate number at which point they are sent to the Recycler.

The Recycler is an 8 GeV permanent magnet ring. The Recycler acts as both a storage ring for the accumulating antiprotons as well as a collection point for those antiprotons that were not used in previous collisions. When the antiprotons are needed for a store, they are transferred back into the Main Injector for further acceleration.

Tevatron

Once there are a sufficient number of protons and antiprotons, both beams are then injected into the Tevatron ring at an energy of 150 GeV. They are

accelerated to an energy of 980 GeV around the ring which is roughly 4 miles in circumference. Each beam consists of 36 bunches which are distributed in three groups of 12, each of the three called a “super bunch”. Each bunch is spaced in time by 396 ns. The number of protons in a bunch is roughly $N_p \sim 2.7 \times 10^{11}$, while conversely the antiproton bunches contain an approximate five times fewer particles, namely, $N_{\bar{p}} \sim 5 \times 10^{10}$.

The bunches of protons and antiprotons are maintained in helical orbits by magnets except for two interaction regions: DØ, where the detector of the same name is located, and BØ where the Collider Detector at Fermilab (CDF) resides. At these locations the beams are forced to collide in the geometric center of each detector using quadruple final focus magnets.

At the beginning of a store, defined as a continuous colliding of proton and antiproton beams, the initial instantaneous luminosity is currently approximately $3 \times 10^{33} \text{ cm}^{-2}\text{s}^{-1}$. A store will typically last about 24 hours, with the luminosity greatest at the beginning and dropping off exponentially as time continues as beam particles are lost due to interactions with residual gas in the beam pipe.

3.2 The DØ Detector

The DØ detector will be discussed in the following sections. Given the complexity of the detector, please see Ref. [41] for more details if desired. The DØ detector consists of several subsystems wrapped up in an onion-like structure, all which work together to extract the key information from each $p\bar{p}$ collision that the Tevatron provides. Figure 3.2 shows a schematic view of the DØ detector where the subsections encompassing each other can clearly be seen.

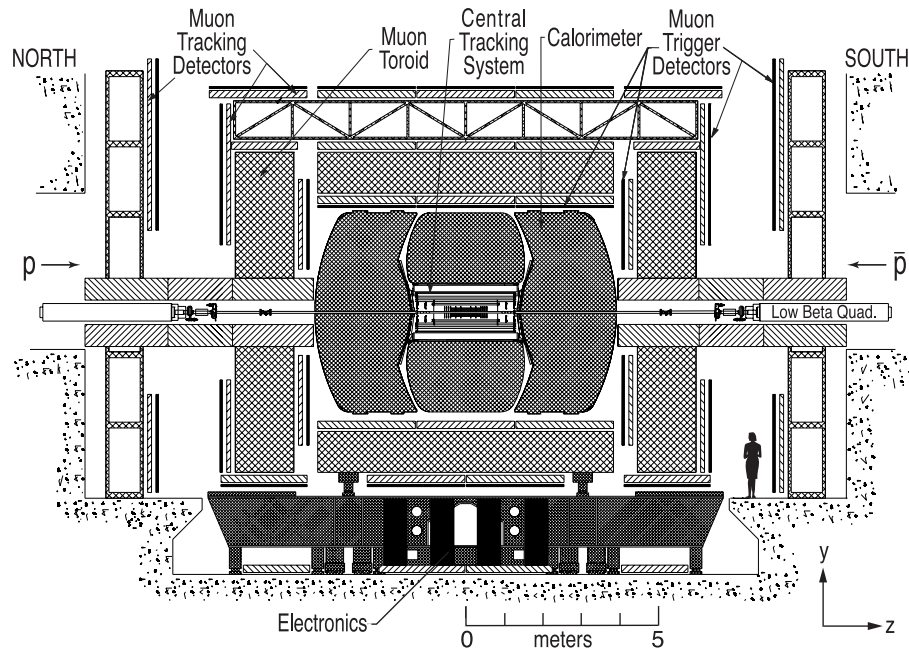


Figure 3.2: The DØ Detector.

Each subsystem is discussed in the following sections: Tracking Systems (Sec. 3.2.2), Preshower Detector (Sec. 3.2.3), Calorimeter (Sec. 3.2.4), Muon Detector (Sec. 3.2.5) and Luminosity Monitor (Sec. 3.2.6).

3.2.1 The Coordinate System

Before going into the details of the subsystems, the coordinate system that is used must be defined. The DØ detector uses a right-handed coordinate with the positive z -axis pointing along the proton direction, the y -axis upwards and x -axis pointing inward toward the center of the ring. Spherical coordinates (r, θ, ϕ) are used as well where r is used to denote the perpendicular distance from the z -axis. Frequently, pseudorapidity (η) is used rather than the angle θ , and is defined as:

$$\eta = -\ln\left[\tan\left(\frac{\theta}{2}\right)\right]. \quad (3.1)$$

In the high energy limit, where $m/E \rightarrow 0$ (which is almost always valid for the relativistic particles arising from the interactions at the Tevatron) the above approximates the true rapidity defined as :

$$y = \frac{1}{2} \ln \left(\frac{E + p_z}{E - p_z} \right). \quad (3.2)$$

When particles are at large η we will call them “forward particles”; similarly regions at large η are described as “forward regions”.

3.2.2 Central Tracking Systems

The central tracking system resides in the very center of the detector. For this thesis, the central tracking consisted of the silicon microstrip tracker (SMT) and the central fiber tracker (CFT). For data that was taken at later dates, another layer of SMT known as “Layer Zero” was inserted between the beam pipe and the original SMT detector for even more precise tracking results. The central tracking used in this thesis can be seen in an overview of the central systems in Figure 3.4 as well as in more detail in Figure 3.3.

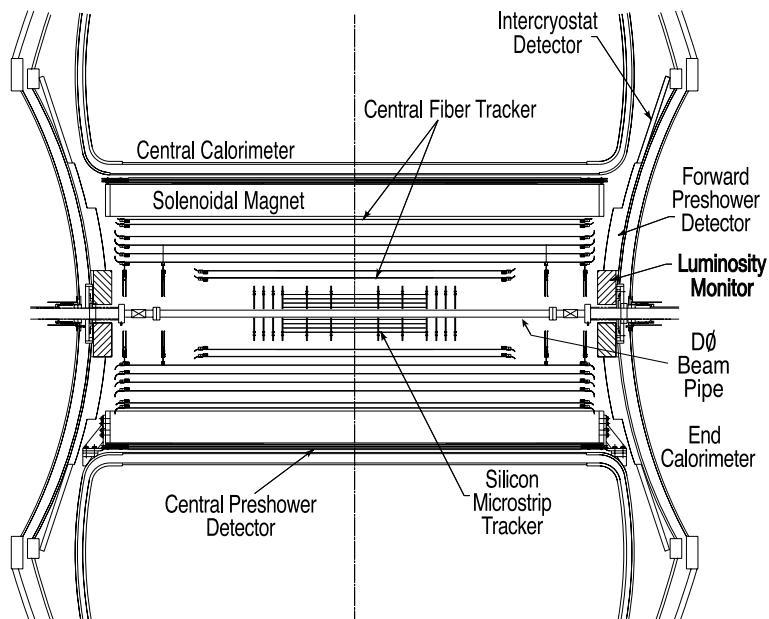


Figure 3.3: Schematic drawing depicting the central detectors in the DØ detector.

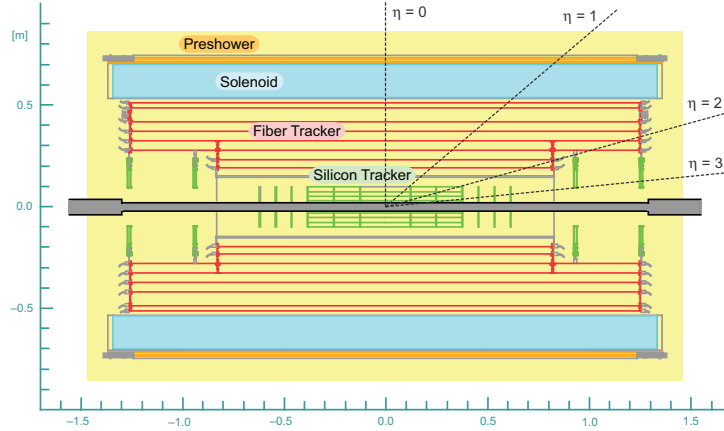


Figure 3.4: Schematic drawing depicting the DØ tracking system.

The two trackers are surrounded by a 2 T superconducting solenoid with the \vec{B} field pointing along the z -axis.. The tracking detectors have a wide range of goals, including: measuring a particle's curvature, and hence transverse momentum using the magnetic field, measuring the direction of the particle, identifying electrons by comparing energy deposits with measured momenta, position tracking over a large range of pseudorapidity ($\eta < 3$), secondary vertex identification, and hardware track triggering. The trackers can also locate the primary vertex of an interaction with a resolution of $\sim 35 \mu\text{m}$ along the beamline.

Silicon Micro Tracker (SMT)

Starting at the beam pipe and working one's way out, the first detector that a particle would encounter is the silicon microstrip tracker (SMT). The SMT is the precision tracking component of the tracking system and is capable of measuring charged track energy deposits (hits) with a resolution on the order of $10\ \mu\text{m}$.

The total length of the SMT detector is determined by the length of the interaction region ($\sigma_z \sim 25\ \text{cm}$). However, due to this length there is a challenge in designing the detector such that tracks are perpendicular to the detector surfaces for the full range of pseudorapidity. In order to overcome this obstacle, the final design of the SMT combined a barrel and disk configuration with both disks and barrels in the central region and disks only in the forward regions. See Figure 3.5 for a schematic description. This setup then allows for a measurement of the r - ϕ coordinate primarily from the barrels, and the disks measuring both r - z and r - ϕ .

As seen in Figure 3.5, there are six SMT barrels surrounding the $z = 0$ point on the beam pipe. Each of the six barrels are 12 cm long, and each has four silicon readout layers. On the readout layers are silicon modules called 'ladders'. Layers 1 and 2 (innermost) have twelve ladder while the outer

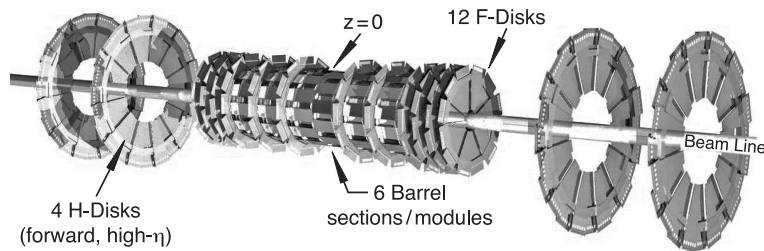


Figure 3.5: Schematic of the silicon microstrip tracker.

layers, 3 and 4, have 24 ladders for a total of 72 ladders per barrel as shown in Figure 3.6. There are thus a total of 432 ladders in the SMT detector.

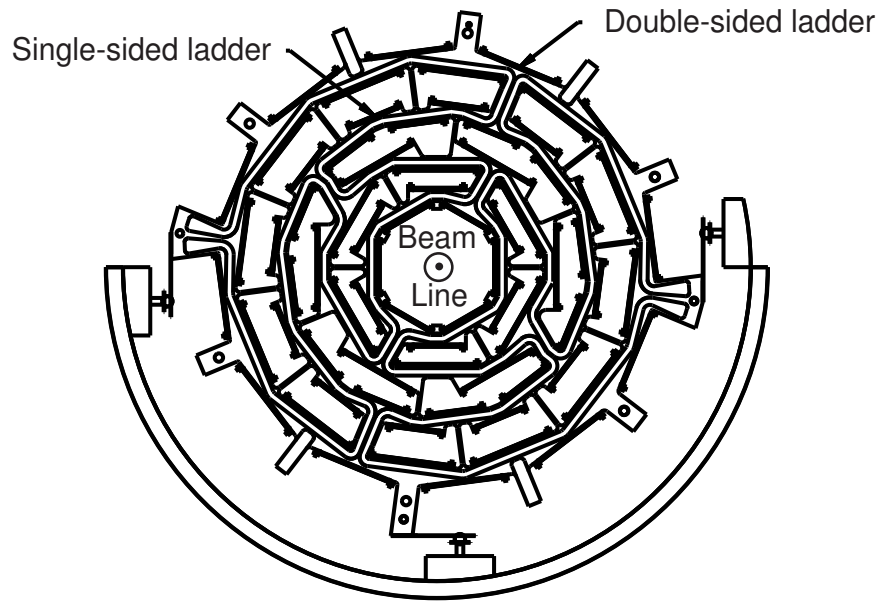


Figure 3.6: Cross section of the SMT barrel.

In the four central barrels, ladders on layers 1 and 3 are double-sided with axial strips on one side and 90° stereo angle strips on the other. On layers 2

and 4, the ladders are double-sided detectors with axial and 2° stereo strips. For the two outer barrels, all the ladders are single-sided detectors with only axial strips. The centers of the barrels are located at $|z| = 6.2, 19.0$ and 31.8 cm.

Moving onto the other component of the SMT detector, the disks, there are 12 ‘F’ disks and 4 ‘H’ disks. The F disks are double-sided detectors with $+15^\circ$ stereo angle on one side and -15° on the other. A F disk is placed at the high $|z|$ position of each barrel. The remaining six F disks are stacked at the forward edge of the barrel/disk construction. All the F disks have an inner radius of 2.6 cm and an outer radius of 10 cm.

In the very forward region of the SMT detector the other set of disks, the 4 ‘H’ disks, are located at $|z|=110$ cm and $|z|=120$ cm. These are also double-sided detectors with $\pm 7.5^\circ$ stereo angle. In total, the SMT consists of 912 readout modules with 792,596 channels, as detailed in Table 3.1.

The readout for the SMT is performed by 128-channel SVXIIe chips. These chips are mounted on High Density Interconnect (HDI) boards. The data is then relayed to sequencer boards through adapter cards and interface boards. From there data travels to the data acquisition system via an fiber optic link. The SMT provides single-hit resolutions of approximately $10 \mu\text{m}$.

Table 3.1: Summary description of the silicon microstrip detector.

	Barrels	F-Disks	H-Disks
Channels	387072	258048	147456
Modules	432	144	96
Silicon Area	1.3 m ²	0.4 m ²	1.3 m ²
Inner Radius	2.7 cm	2.6 cm	9.5 cm
Outer Radius	10.5 cm	10.0 cm	26 cm

Central Fiber Tracker (CFT)

After the particles travel through the SMT, they pass through the Central Fiber Tracker or CFT, the detector that surrounds the SMT. The primary job of the CFT is to work with the SMT and combine with the SMT track reconstruction and momentum measurement in the $|\eta| < 2$ region. The CFT is also necessary for providing fast track triggering in the $|\eta| < 1.6$ region.

The CFT consists of eight concentric carbon fiber cylindrical supports upon which scintillating fibers are mounted. Each of the cylindrical supports has a doublet layer of fibers that are oriented parallel to the beam pipe. On alternating cylinders is another doublet layer oriented at a 2° to 3° stereo angle. Figure 3.7 shows a cross section of the CFT detector. The radii of the supports range from 20 to 52 cm away from the beam pipe.

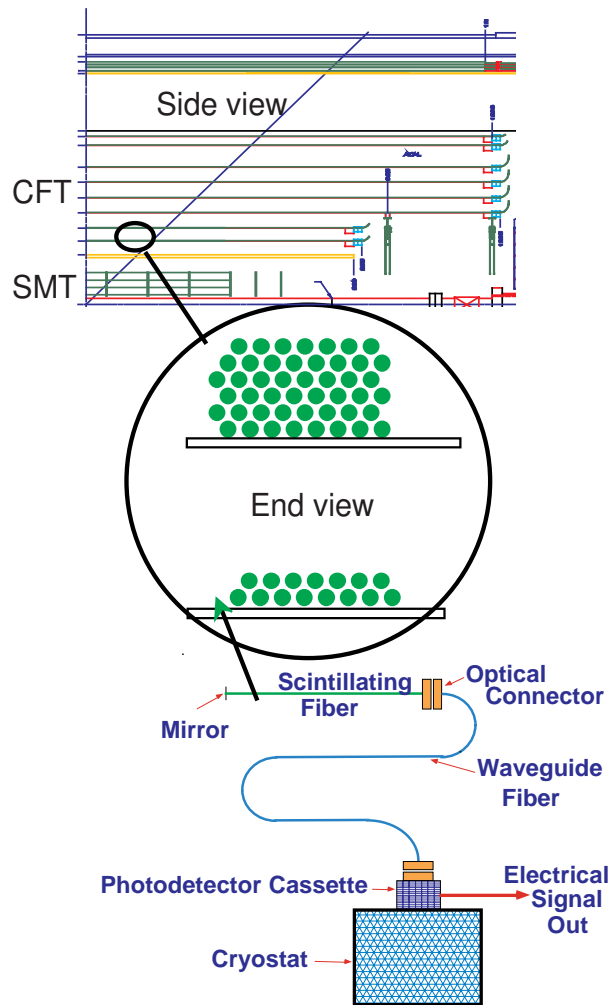


Figure 3.7: Cross section of the Central Fiber Tracker.

The scintillating fibers are made up of a polystyrene core, which is then covered with a layer of acrylic cladding. The acrylic cladding is coated with a layer of fluoroacrylic cladding. Each layer of cladding is $15 \mu\text{m}$ thick. To increase the light yield from the fibers, the polystyrene used for the

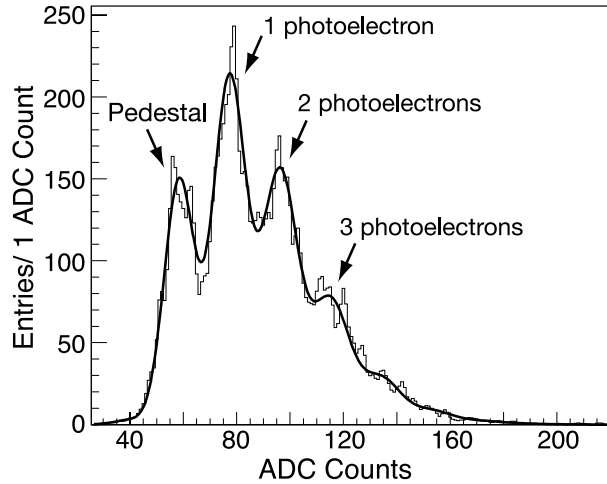


Figure 3.8: A typical LED spectrum for a single VLPC showing the resolution of single photons.

core is doped with 1% paraterphenyl. It is also doped with 1500 ppm 3-hydroxyflavone that shifts the scintillation light to 530 nm which is ideal for transmission in the polystyrene material. The diameter of the fibers is 835 μm and have lengths ranging between 166 to 252 cm. There is a total of 76,800 scintillating fiber readout optical channels.

The fibers run along the cylinders and then connect to clear fiber waveguides (that were constructed at Indiana University) that transport the scintillation light to a photodetector called a Visible Light Photon Counter (VLPC). These VLPCs are arsenic-doped silicon-avalanche devices that convert visible light into a useful electronic signal. They operate with a high

quantum efficiency ($\sim 80\%$), have large gains (22,000 to 65,000), low noise, and read out over 78,000 separate electronic channels. The VLPCs operate at temperatures of $8 - 10^\circ$ K and have the ability to resolve single photons as can be seen in Fig 3.8. The CFT detector provides a single hit resolution of $\sim 110 \mu\text{m}$.

Solenoid

A new addition to the DØ detector for Run II was a 2-T solenoid magnet that was added to allow for the determination of momentum of charged particles. The size of the magnet was restricted by the space in the central calorimeter void which is 2.73 m long with a 1.42 m diameter. It has two layers of 0.848 mm superconducting coil and operates at a temperature of 4.7 K and a current of 4749 A. The 2 T magnetic field has been measured to be uniform within 0.5%.

3.2.3 Preshower Detector

The preshower detector has two components: the central preshower detector (CPS) and the forward preshower detector (FPS). The purpose of this detector component is to aid in the identification of electrons, enhance matching between the hits in the calorimeter (discussed in the following sec-

tion) and the tracking detectors (previously discussed), as well as helping to correct for energy loss in material that is upstream from the calorimeter. Location of the preshower detectors can be seen in Figure 3.3.

The CPS consists of three concentric layers of triangular scintillator strips. Each of these has a wavelength shifting fiber (WLS) embedded in the center. The purpose of the WLS is to transfer the light from the scintillators to the waveguides. From the waveguides (also fabricated at Indiana University) the light is then transferred to VLPCs, similar to that of the CFT readout.

The FPS is very similar to the CPS. In the FPS there are two layers of two planes of scintillator strips located at different z positions. The two layers are separated by lead-stainless-steel absorbers. This is not the case for the region $1.5 < |\eta| < 1.65$ where the FPS lies in the shadow of the solenoid magnet coil and so there is no need for an additional layer of absorption. See Fig. 3.9 for a graphical representation of the CPS and FPS.

3.2.4 Calorimeter

The next subdetector layer in the DØ detector is the calorimeter. The purpose of a calorimeter is to measure the energy of the particles that enter the calorimeter. For electrons, photons and jets the calorimeter can measure

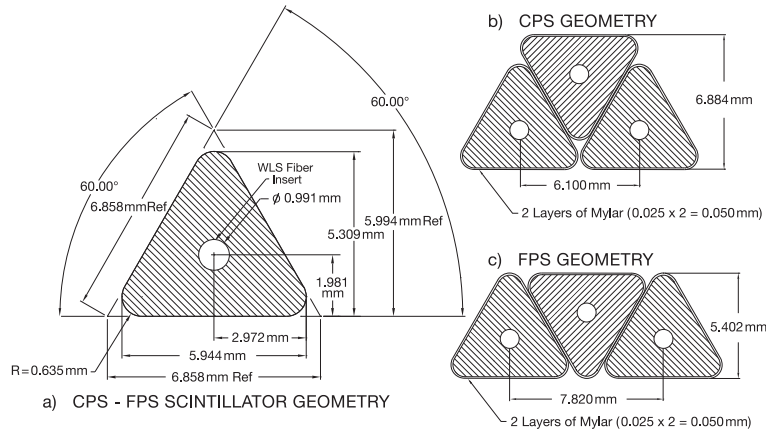


Figure 3.9: Cross section and layout of the CPS and FPS. The circles represent the location of the wavelength-shifting fiber.

the energy independent of a central magnetic field. The calorimeter can also help with particle identification while providing a measure of the transverse momentum balance in an event.

The fundamental concept behind calorimeters is that a particle traveling through will lose energy by interacting with the matter encapsulated within the detector. The energy loss can either be caused through an electromagnetic interaction for electrons or via a strong force interaction when hadrons are involved.

For electrons, the mechanism for energy loss depends on the incident energy. If the electrons are incident with $E_e < 10$ MeV, they will lose energy via ionization. Conversely, if they are incident with $E_e > 10$ MeV, they will

lose energy via brehmsstrahlung. The higher energy electrons, i.e., those that undergo brehmsstrahlung, will emit a photon that will, in general, produce electrons and positrons through pair production. These resulting electrons and positrons will then in turn produce more photons that will follow the same chain of events. The end result is a ‘shower’ of an electromagnetic interaction within the calorimeter. The total energy deposit of the shower is proportional to the energy of the incident electron (or photon).

When a hadron enters the calorimeter the resulting effect is similar. Hadrons will interact through an inelastic collision with the nucleus of the absorption material. This causes an emission of additional hadrons, which similar to the positrons and electrons that came from the photon, will undergo additional reactions with nuclei. Thus a cascade of hadronic particles (hadronic shower) is generated analagous to the electromagnetic shower described previously. The qualitative difference between the two is that while the electromagnetic radiation tends to have a relatively short radiation length, nuclear interaction tends to have radiation lengths that are much longer. Therefore, the hadronic showers tend to be more extended within the calorimeter volume.

There are two types of calorimeter detectors, “homogenous” and “sam-

pling”. A homogenous detector’s entire volume outputs a signal. A sampling calorimeter on the other hand has only a portion of the calorimeter outputting signal that is proportional to the total energy deposited. The DØ calorimeter is of the latter type and can be seen in Fig. 3.10.

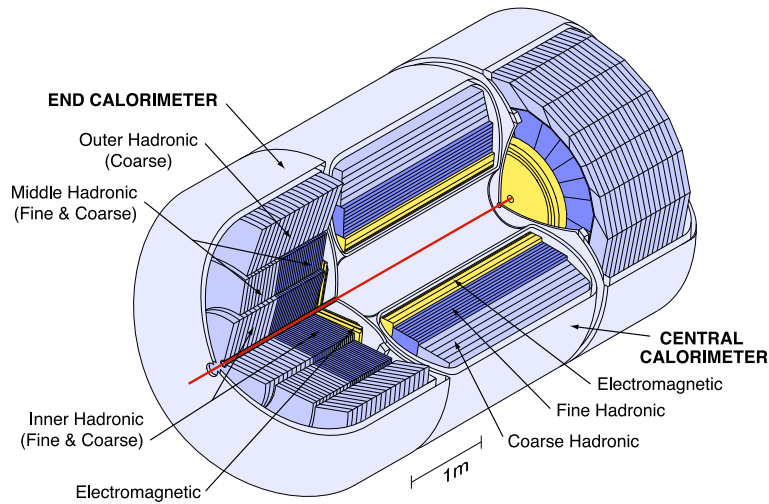


Figure 3.10: Cutaway view of the calorimeter system of the DØ detector.

A sampling calorimeter utilizes a high density material in order to cause the energy loss as well as an active medium to generate a signal. Specifically, the DØ calorimeter uses a combination of nearly pure depleted uranium and copper for the absorption material and the active medium used is liquid Argon. Ionization due to showering particles will occur in the Argon and thus produce an electric signal.

The DØ calorimeter consists of three components, the Central Calorimeter (CC), and two Endcap Calorimeters (EC). The CC covers the region of $|\eta| < 1.0$ while the ECs which, as the name implies, are positioned on either end of the CC covering the region $1.0 < |\eta| < 4.0$. Each of the components of the calorimeter have three types of modules: an electromagnetic section (EM), a fine hadronic calorimeter (FC), and coarse hadronic calorimeter (HC).

The EM employs thin plates of nearly pure depleted uranium for absorption, the FC uses thicker plates of a uranium-niobium alloy, and the HC uses relatively thick plates of copper or stainless steel. For all three sections, liquid Argon is located between the plates and is used as an active material for transmitting the signal through ionization of atoms by charged particles. Figure 3.11 shows a schematic of a typical calorimeter cell.

For a particle passing through the calorimeter, the position resolution is determined by the size of the cells. The EM is divided into four layers and most of the cells are divided into coarse segmentation (0.1×0.1 in $\eta \times \phi$ space). However, in the third layer there is a finer segmentation of (0.05×0.05) because this is where the electromagnetic shower is expected to reach its maximum. Within the hadronic calorimeter, the FC has a segmentation

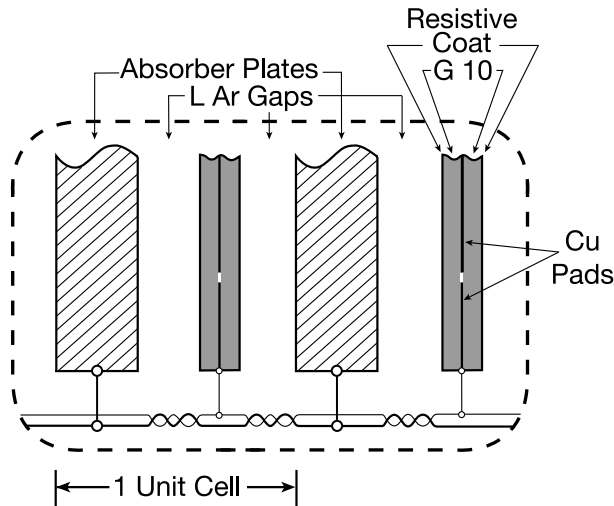


Figure 3.11: Schematic of calorimeter cell showing the Liquid Argon gap and signal board unit cell.

of 0.1×0.1 and the HC has a segmentation of 0.2×0.2 . This is visually depicted in Figure 3.12.

Between the endcaps and the central calorimeters, there are several gaps where particles will pass through support structures rather than instrumentation. To account for the energy loss that will occur here, two different type of detectors are installed: the Inter-Cryostat Detector (ICD) and Massless Gaps (MG). The ICD is a single layer of scintillating tiles mounted on the surface of the endcaps. The MG is installed before the first layer of uranium and consists of two readout cells which contain signal boards and liquid argon gaps and uses the cryostat walls as an absorber.

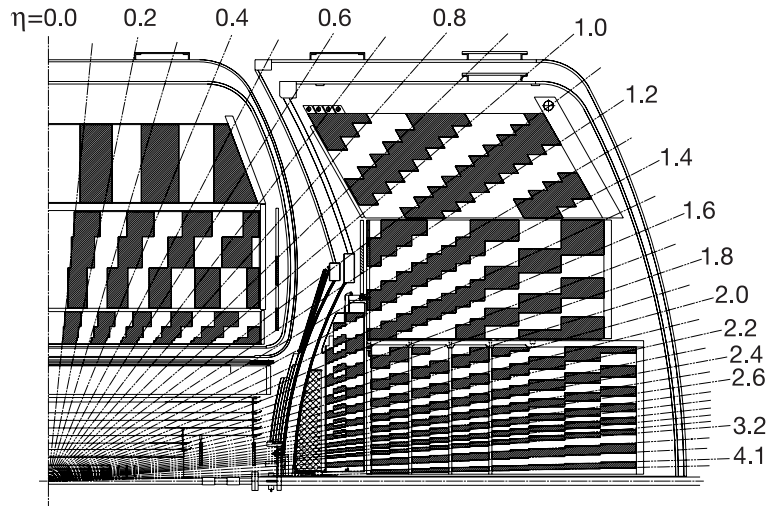


Figure 3.12: Quarter cutaway view showing segmentation pattern of calorimeter.

3.2.5 Muon System

For the analysis that is presented in this thesis, the muon detector was the most important component for characterizing a signal since the final signature of the B_c^\pm meson decay was three muons. Muons leave only minimal traces of energy in the calorimeter and a specialized detector is therefore needed to detect them. The muon detector [42] is the outermost layer in the onion-style configuration of the DØ detector. If a particle is going to reach the muon detector, it needs to pass through all the detectors previously described: the tracking system, the solenoid magnet and the calorimeter. The charged

particles with lifetimes long enough to be able to enter the calorimeter are pions, kaons, protons, electrons, and muons. Pions, kaons, and protons are strongly interacting particles that typically result in a hadronic shower in the calorimeter. These interactions are typically 10.5 nuclear interaction lengths deep. Electrons or photons will essentially always deposit all of their energy in the calorimeter (21 radiation lengths deep) in electromagnetic showers. Muons do not interact strongly, and at the energies involved, do not undergo bremsstrahlung and don't develop electromagnetic showers. They can therefore easily pass through the calorimeter leaving only minimal energy deposits due to ionization. As a result, hits detected in the outer muon chambers are very likely to be due to muons. The "punchthrough" rate of other charged particles such as pions, kaons, and protons producing complete segments in the muon chambers is very small, typically 10^{-6} to 10^{-5} .

The muon detector is comprised of three main components: scintillators for triggering and cosmic background rejection, drift tubes to measure hit positions and a 2-T torodial magnet that allows for an independent measurement of the muon momentum by bending muons in the r - z plane as they pass through the field. The toroid is actually comprised of three toroids: the central iron toroid (CF) and two end iron toroids (EFs). These magnets

comprise 65% of the total weight of the entire 5500 ton DØ detector. The location of these three components with respect to the rest of the DØ detector components and themselves can be seen in Figure 3.2.

The drift tubes and counters are assembled in three layers: A, B and C, where layer A is the innermost layer and is located between the calorimeter and toroid magnet. Layers B and C are outside of the toroid with layer C, naturally, the outer most layer. The assembly pattern of the drift tubes and scintillators can be seen in Figure 3.13 and Figure 3.14, respectively. The muon detector is divided into the central muon detector and forward muon detectors which are described in the following sections.

Central Muon Detectors

The central muon system covers the the pseudorapidity region $|\eta| < 1$ and is made up of the following: CF magnet, proportional drift tubes (PDT) chambers in all three layers, $A\phi$ scintillator counters on all sides of the A-layer and the sides and bottom of the B-layer, cosmic cap scintillators in the C-layer, and cosmic bottom scintillators in the B- and C-layer.

The PDT's in the Central Muon Detector are fairly large with a surface area of $2.8 \times 5.6 \text{ m}^2$. Each of the drift tubes has a wire of gold-plated tungsten strung through the center that serves as the anode. The drift tubes are filled

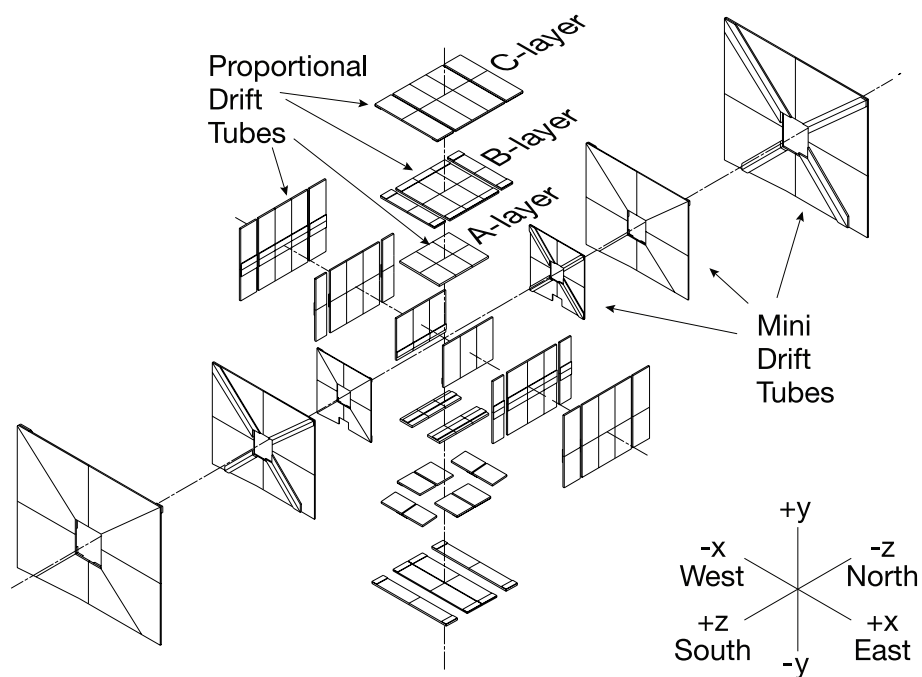


Figure 3.13: Schematic view of Proportional Drift Tubes and Mini Drift Tubes.

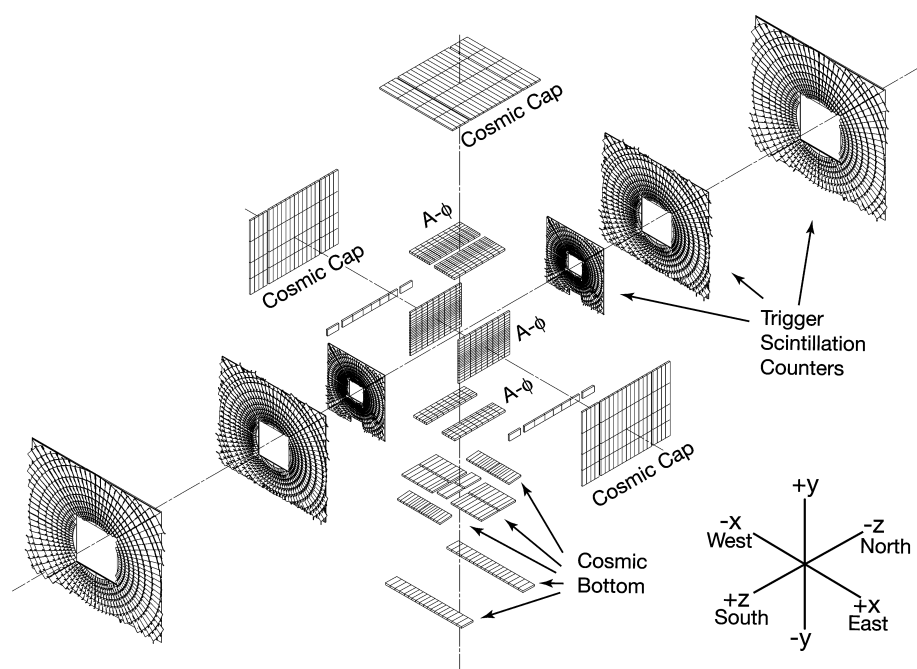


Figure 3.14: Schematic view of the muon scintillation counters.

with a gas mixture consisting of 84% Argon, 8% CH₄ and 8% CF₄. When a muon passes through the PDT, the gas is ionized and the drift time of the electrons to the wire gives a positional resolution of 1.0 mm in the z direction. When one combines the signal from the neighboring PDTs, the resulting resolution in the chamber x - y plane is between 10–50 cm, with the range depending on how close to the readout electronics the hit is along the wire.

The $A\phi$ scintillators are located between the calorimeter and the A-layer PDTs as well as on the bottom of the B-layer. There are 630 $A\phi$ counters, each roughly 4.5° wide in ϕ to match the segmentation of the central track trigger. The cosmic cap scintillators are installed on the outside of the C-layer PDTs, while the cosmic bottom scintillators are installed on the outside of the B- and C-layers. There are 240 counters in the cap and 132 in the bottom and these also have a ϕ segmentation of 4.5°.

Forward Muon Detectors

The forward muon system covers the pseudorapidity range $1.0 \leq |\eta| \leq 2.0$. It consists of EF magnets, three layers of mini drift tubes (MDTs), three layers of scintillation counters as well as shielding around the beam pipe. The MDTs in this part of the muons system are notably smaller than

the previously mentioned PDTs, consisting of eight cells each measuring $9.4 \text{ mm} \times 9.4 \text{ mm}$ in cross section, as shown in Figure 3.15 for a schematic diagram of a MDT. There are 6,080 such drift tubes arranged in six layers, each layer consisting of eight octants. These drift tubes are filled with a gas mixture of 90% CF_4 and 10% CH_4 . This mixture results in a very short drift time of 60 ns. Through the center the drift tubes there is a $50 \text{ }\mu\text{m}$ tungsten-gold wire, which is oriented parallel to the magnetic field from the center toroid magnet. The forward muon system has a position resolution of $\sim 1 \text{ mm}$ and improves the resolution for high momentum muons. For those tracks that don't hit all the layers of the CFT, namely with a pseudorapidity in the range of $1.6 \leq |\eta| \leq 2.0$, the forward muon detector is particularly important.

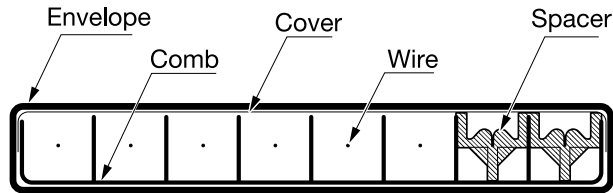


Figure 3.15: Cross-sectional view of mini drift tube.

In front of each layer of MDTs there is a “pixel” scintillator counter which is useful for reducing backgrounds coming from sources other than the event

interaction, such as cosmic rays. These pixel counters are also essential for providing fast signals to the trigger system. The scintillators in the forward detector have a ϕ separation of 4.5° to match the track trigger. There is a total of 4214 counters and their average time resolution is ~ 1 ns.

3.2.6 Luminosity

The luminosity monitor, as its name suggests, is used to determine the luminosity at DØ by counting small angle elastic proton-antiproton scatters. The luminosity monitor is mounted on the front faces of the end calorimeters at $z = \pm 140$ cm and covers a pseudorapidity of $2.7 \leq |\eta| \leq 4.4$. It consists of two arrays of twenty-four scintillator counters that are read out by PMTs. In Figure 3.16, the location of the luminosity monitor (denoted by LM) with respect to the rest of the inner detectors can be seen. Additionally Figure 3.17 shows the layout of the detector arrays. Aside from determining the luminosity, the luminosity counter also helps in determining a z -coordinate of a primary vertex via a measurement of the difference in arrival time for the particles that hit these counters.

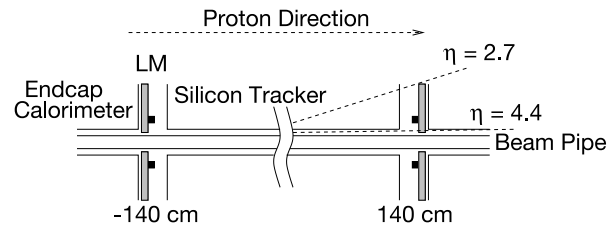


Figure 3.16: Schematic showing the location of the luminosity monitors within the DØ detector.

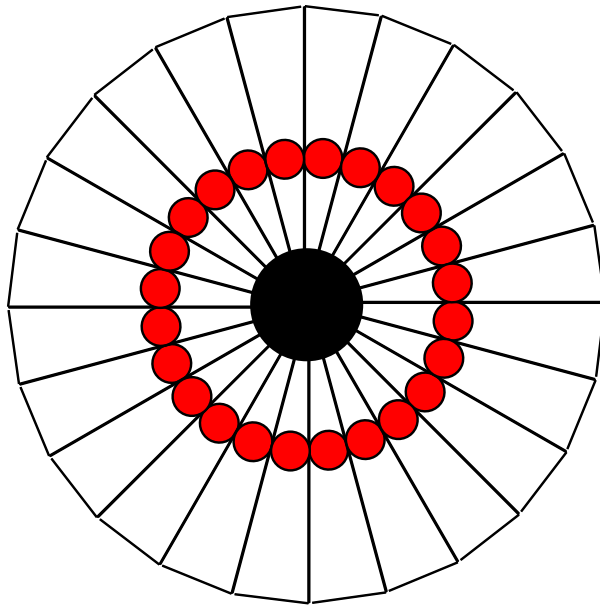


Figure 3.17: Schematic of luminosity monitor, showing scintillation counters (triangular segments) and PMTs (block dots).

3.3 The DØ Trigger System

The proton and anti-proton beams collide at a rate of 1.7 MHz at the DØ interaction point. This rate is much too high to read out events and write them out to recording media for use in physics analyses. In addition to the busy environment of each collision, not every event is of physics interest and so they must be discarded. To address these issues, DØ makes use of a three-stage triggering system that identifies and stores events that potentially have interesting physics signatures to be examined later in an analysis.

The three stages of the triggering system are named: Level 1 (L1), Level 2 (L2) and Level 3 (L3). The first two stages depend solely on hardware systems to make decisions on the importance of an event, while the final stage uses software systems to make its determination. More specifically, L1 accepts the 1.7 MHz rate and through simple hardware-based decisions, drops the rate to 2 kHz and passes it on to L2. Level 2 employs hardware with embedded microprocessors to construct trigger decisions using individual physics objects as well as correlations between objects. This more sophisticated system drops the rate to 1 kHz. L3 takes the 1 kHz rate and uses even more sophisticated algorithms in a farm of CPUs to reduce the rate to 50-100 Hz which can then be recorded for offline reconstruction. An

overview of the DØ trigger system can be seen in Figure 3.18. The different stages are discussed below in more detail.

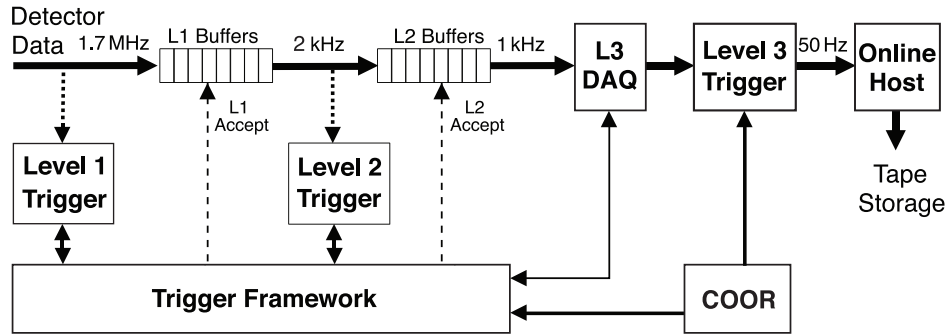


Figure 3.18: The DØ trigger system.

3.3.1 Level 1

When an event comes into the L1 trigger, specialized hardware determines whether or not the event has characteristics of interest. That information is passed to the trigger framework (TFW) that holds all the information coming from L1. The TFW will issue a L1 accept if it deems that an event should continue on to L2 for further investigation. The L1 trigger is fast, providing decisions in $4.2 \mu\text{s}$ with little or no deadtime.

Almost all of the detector subsections, the calorimeter, CFT, preshower and muon systems send information to the L1 triggers. The SMT sends its

information directly to L2 due to bandwidth constraints. All of the detector subsystem information combines within the TFW and thus a comprehensive decision is made at this location. To eliminate the problem of deadtime, the L1 triggers are all buffered and have enough memory associated with each trigger to retain data from 32 beam crossings.

L1 supports 128 separate trigger bits, each of which determines whether there is a valid trigger in a beam crossing. The logic that determines if a particular bit is set is built into the L1 hardware using a series of field-programmable gate-arrays (FPGA's). If any of the 128 bits are satisfied the event is passed along to L2 for further investigation.

3.3.2 Level 2

The next level of the trigger system, L2, is composed of an array of detector-specific pre-processing engines (FPGAs) and a global processor (L2Global) which will examine the incoming physics objects as well as correlations in physics signatures across the various subsystems. The L2 trigger makes decisions in 100 μ s. This system reduces the rate of data flow by about a factor of two.

There are two steps to the L2 trigger decision. First, the subdetector

processors take information from what has been passed on from Level 1 and uses this information to form physical objects, including energy clusters and tracks. The next step utilizes L2Global which makes trigger decisions based on objects that are identified by the processors in L2, namely:

- L2 silicon and central track trigger (L2STT and L2CTT),
- L2 central and forward preshower trigger (L2CPS and L2FPS),
- L2 calorimeter trigger (L2CAL),
- L2 muon trigger (L2Muon).

Physics objects can be constructed directly from the output of the above processors or by combining objects from different processors. Events that pass the L2 requirements are then sent on to the L3 buffers for more testing and eventually acquisition. Figure 3.19 shows the full layout of the L1 and L2 systems.

3.3.3 Level 3 and Data Acquisition

The Level 3 trigger is different from the previous two discussed in that it is a fully programmable software based trigger system rather than a hardware-based system. The L3 system makes a quick, albeit limited, reconstruction

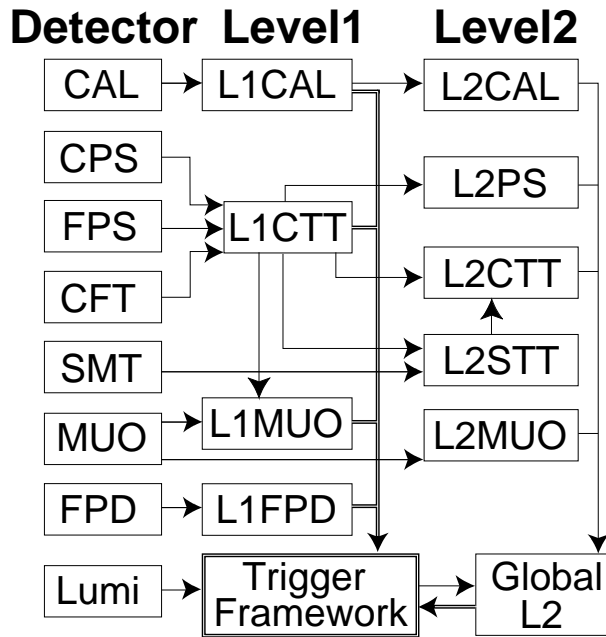


Figure 3.19: Flowchart showing the DØ Level 1 and Level 2 trigger system.

of events. The final trigger decision is based on complete physics objects (e.g. electrons, muons, and jets) as well as the relationship between objects (e.g. azimuthal angle separating objects or the combined invariant mass). After the data has gone through L3 the rate is reduced from 1 kHz down to 50-100 Hz. Figure 3.20 shows the layout of L3 as well as the data acquisition system that will be discussed below.

When an event passes L2, it issues an accept and the data is then transferred out of the respective readout crates by a single board computer, or SBC, which is situated in each crate. There is one SBC which is only used

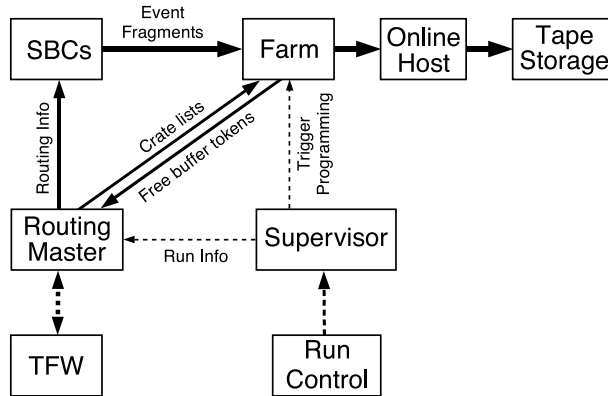


Figure 3.20: Schematic representation of L3 system and data acquisition.

to take the data from the SBCs and transfer them to the farm nodes where additional processing is done. This SBC is called the Routing Master and collects multiple pieces of information including the event number and L1 and L2 triggers for the event. Each event is sent to a unique farm node within a processing farm of 600 nodes [43]. The data is transferred from SBC to farm node via two 100 MB/s ethernet cables.

After an event arrives at L3, it is processed by a software package called the Event Builder (EVB). The EVB takes the event information from the SBCs and builds complete events from that information. For each event in question, the Routing Master sends along a list of expected crates to the EVB of the particular node so that it will know when and if the event is complete. Therefore if the EVB is missing information from a crate that it

expects information from, the event is discarded. If an event is complete and kept, then it moves to shared memory buffers in a format that allows the L3 trigger to make a decision regarding the validity of the event. There are 2 - 4 L3 trigger processes which are applied to the event. If the event satisfies one of these processes the event continues on. From here it is passed over 100 MB/s ethernet cables to the Collector which is a temporary storage device.

When enough events have accumulated, the data is transferred to a machine called the Datalogger and then to its final resting place at the Feynman Computer Center which is located at Fermilab. The data representing event collisions is then stored on tapes and maintained in a tape robot system.

Chapter 4

Reconstruction and Simulations

Once an event in the system with some physics promise, the next step to is go back and collect the complete information in each of the subdetectors and reconstruct the event into an object that can then be stored and analyzed off-line. This chapter describes in detail how this is done, and more specifically Section 4.1 discusses how the particle tracks are reconstructed in the data as well as within Monte Carlo simulations, and Section 4.2 discusses generating and simulating data using Monte Carlo.

4.1 Event Reconstruction

The following discusses how a track is reconstructed in the tracking chambers and the muon detector system.

4.1.1 Track Reconstruction

When a charged particle travels through the DØ detector, it follows a three-dimensional helical path due to the magnetic field created by the solenoid. This takes the particle through the various subdetectors and as the particle passes through them, it leaves an energy deposit within each detector. This helical path is what is known as a ‘track’ and, by examining the energy deposits in more detail, we can reconstruct it and trace its journey through the DØ detector systems.

To identify one of these tracks, there are several steps the track reconstruction program goes through. First it goes through the charge ‘clusters’ (described later) that have been left in the tracking system. Then, using those clusters, it attempts to link them together - similar to a “connect the dots” game - to make one continuous track. There are two different methods to do this: the Histogram Track Finding (HTF) [26] method and the Alternative Algorithm (AA) [27] tracking method. To complete the track identification, a global track reconstruction algorithm combines the tracks using the information from the HTF and AA methods.

Track Hit Clustering

As mentioned earlier, the first step in identifying a track is finding charge ‘clusters’ in the tracking system or, more to the point, identifying a ‘hit’ in either the SMT or CFT systems. In the SMT, a hit is defined by the deposit of charge from an ionizing particle that is over some threshold (8 analog-to-digital counts). This threshold is required to reduce the background from detector noise. If an additional hit is found on an adjacent silicon strip, these two hits are combined and form the start of the cluster. This is repeated for hits in any surrounding strips. The center of the hit is determined by a charge-weighted average of the central position of each silicon strip. For the CFT system, a hit is recorded in a similar method. This time however, instead of adjacent silicon strips, hits are recorded in consecutive layers of fibers. The position of a hit is the half-way point between two fibers. The two hit fibers represent the end points of the cluster. The CFT resolution is $\sim 100 \mu\text{m}$ while the resolution for the SMT is $10 - 15 \mu\text{m}$; the range is due to dependence on the cluster width.

Histogram Track Finding Method (HTF)

When particles travel through the tracking chamber, they leave several hits in the transverse, x - y , plane. These particles will also have unique curvature and azimuthal angle. From these inputs, the HTF method [26] transforms the hits in the x - y plane to a plane formed by the curvature, $\rho = 1/R$, and the azimuthal angle (ϕ), also known as ρ - ϕ space. If the hits are from the same particle, then there will be a peak in the ρ - ϕ space, whereas if they were just random hits, it would have a flat distribution. A histogram is generated from the hit information and then processed through a two-dimensional Kalman filter removing noisy tracks with large errors. The HTF method also incorporates detector geometry as well as material density which results in a set of smooth tracks. Longitudinal information is included and the tracks are either extrapolated back to the SMT if the track originated in the CFT or vice versa if the track originated in the SMT.

Alternative Algorithm Tracking (AA)

For the lower- p_T events that are common in a B physics data analysis, the Alternative Algorithm (AA) tracking method [27] is better suited for track finding and reconstruction. The first thing the AA method does is

form track candidates using any three clusters in the SMT, resulting in an initial track hypothesis or ‘seed’ hit. AA starts from the innermost layer and works its way outward. If the axial angle between the first and second layer is less than 0.08 rad, AA adds on a second layer. A third layer is added if the radius of an extrapolated curve through the three points has a radius of greater than 30 cm. This requirement corresponds to a $p_T \geq 180$ MeV. The impact parameter with respect to the beamspot must be less than 2.5 cm and the track fit must have $\chi^2 < 16$ for the third layer to be added.

After this, AA continues on to the next layer of the SMT or CFT and it generates an expected crossing region. Any track that is found within this window is tested and, if found to be a track match, a new hypothesis is made. If there is no matching track found, the layer is considered a ‘miss’. These misses are categorized into three different types: inside misses (misses that occur between any two hits in a track hypothesis), forward misses, and backward misses (misses when the extrapolation either outward or inward shows no track matches). The restriction on the number of misses depends on the category of miss, where the inside misses hold the most stringent requirements. If the $D\emptyset$ detector had 100% efficiency, an inside miss would surely mean that the track was a fake. For the other two misses however,

there exists physical reasons for their existence. For example, the track could interact with matter creating a forward miss or a track may not originate from the primary vertex, such as a long-lived $K_S^0 \rightarrow \pi^+\pi^-$ decay, and causes a backward miss.

The track hypotheses are then ordered to determine the best track as follows: hypotheses with the most hits are ranked highest, hypotheses with an equal number of hits - the fewest total misses are preferred - come next, and the list ends with hypotheses with the same number of hits and misses where the best track χ^2 is placed first. To determine the best track, the ‘number of shared hits’ criteria is set [27]:

$$N_{shared} \leq \frac{2}{3}N_{total} \quad N_{shared} \leq \frac{1}{5}N_{total} \quad \text{and} \quad N_{total} - N_{shared} < 3. \quad (4.1)$$

N_{total} represents the total number of axial clusters associated with a track candidate while N_{shared} is the number of shared axial clusters. To further reduce the number of fake tracks, tracks with a small impact parameter with respect to the primary vertex have their hit count incremented by 2 and the tracks are reordered. The track selection then continues with this new ordered list. The reordering helps confirm that the track candidates are associated with the primary vertex.

To improve overall efficiency, AA considers also tracks with only CFT

clusters only. When this is done, the tracking method starts in the innermost layer of the CFT and moves outward. Then each track extrapolated from the CFT clusters has to have an impact parameter with respect to the primary vertex of less than 1.5 cm. When this track is found, it is extrapolated back to the SMT to find clusters with which it can be associated. By allowing track finding in this manner, the overall efficiency of track finding is increased.

For the DØ detector the overall momentum resolution is:

$$\frac{\sigma(p_T)}{p_T} = \sqrt{0.015^2 + (0.014 \times p_T)^2}, \quad (4.2)$$

where the first term is the multiple scattering term.

Calorimeter Reconstruction

When a charged particle passes through the calorimeter, the liquid argon it comes in contact with is ionized and the collection of electrons resulting from this process defines a calorimeter signal. This signal is then digitized and read out by electronics, a correction is applied to account for differences between the cells, and then this corrected number of counts is then converted into an energy deposit which is measured in GeV.

When there are energy deposits in neighboring cells, a cluster is formed and thus a calorimeter object can be reconstructed. An EM cluster is de-

fined as a group of towers in the calorimeter within a cone surrounding the highest energy tower. When the total energy is calculated, the fraction of cells from EM versus hadronic layers is used to determine whether the object is an electromagnetic or hadronic jet. If the jet is an EM jet, the particle is identified as an electron if it can be matched to a central track, or a photon if there is no track match.

Muon Reconstruction

The $D\bar{0}$ muon system has three layers of detectors as previously discussed in Chapter 3.2.5, and muons are reconstructed by requiring hits in these three layers. Hits in both the scintillators and drift tubes are used to reconstruct muon tracks.

In the central region, the PDTs provide a measurement of two timing signals: the drift time, which is the time it takes for the electrons resulting from the ionization to reach an anode, and the axial time, which is the time between the electrons hitting the wire and the arrival of the signal at the readout. These two measurements provide information on the track's location. The drift time, when combined with the angle of the track, gives the distance perpendicular to the wire and the axial time gives a position along the direction of the wire. Combining this information with the scintillator hit

position improves the axial resolution. The momentum resolution is $\sigma(1/p) = 0.18/p \otimes 0.005$ with p in GeV/ c .

For the forward region, the MDTs do not separate the axial and longitudinal drift time but rather provide the sum of these two properties, although the positions are can still be calculated. For the axial position of the track, a matching scintillator time is required. With this information in hand, the drift time can be determined and used to calculate the distance perpendicular to the wire.

Once the hits have been reconstructed, straight lines called ‘links’ are formed between straight track segments that are within 20 cm of each other, not in the same plane, and not from the same wire hit. This process is known as a linked list algorithm. If two links are found to be compatible with a straight line, the links are merged to form a new link that contains all the information from the original two links. Once this track fit is completed, the segment is extrapolated to a corresponding scintillator position in the plane of the wire hits. If a scintillator hit should be found and matched, the track is refit, now taking into account scintillator timing.

Since there are three layers in the muons system, a good muon candidate should have hits in all three layers. Matching begins in the B and C layer and

a match is made assuming straight line segments since there is no magnetic field between these two outer layers. A fit is made to the two segments and, since there are multiple track candidates for each set of line segments, the one with the best χ^2/n_{dof} is chosen. If there are only two hits in a segment, the segment most compatible with coming from the primary vertex is chosen. After having a track match in the B and C layers, the A-layer segments are fit with the BC segments and a ‘local’ muon track is declared. The difference in this level of matching is that when traveling from layer A to layer B, the particle must traverse the local magnetic field in the toroid that is located between these two layers. The fit is thus not a straight line but rather a helical path. The fit also takes into account energy loss within the material as well as multiple scattering at each point. The local muon track can then be matched to a track that has been found within in the central tracker and thus a ‘global’ muon track is found and recorded.

4.2 Event Simulation

An important component of this thesis is the simulated Monte Carlo (MC) samples of data that are used to represent the signal and the background processes. The process of generating these events is described in the following

sections.

4.2.1 Event Generation

To describe $p\bar{p}$ hard scatter events, an ‘event generator’ is used - which simulates events at the four-vector level. The generator that is used in this analysis is the PYTHIA generator [32]. This generator incorporates all of the underlying physics as it is currently understood in the generation of events including hard and soft sub-processes, parton distribution functions, fragmentation, etc. To properly simulate these multiple properties, Monte Carlo techniques are in place to simulate quantum mechanical variations observed in nature and includes both average behavior and fluctuations.

For this analysis, PYTHIA is used to generate several different samples of events with different requirements which will be discussed more in Chapter 5. One of the major differences, aside from a signal versus a background sample, is the difference in $b\bar{b}$ pair production. One method (`mse1 = 5`, Figure 4.1 (a)) specifically produces a $b\bar{b}$ pair initially in the collision with the b and \bar{b} produced back-to-back. The other method generates a ‘QCD’ inclusive sample where the $b\bar{b}$ pairs are produced through gluon splitting as well as via direct production (`mse1 = 1`, Figure 4.1(b)). With the second sample, for

example, it is possible to produce a $u\bar{u}$ pair in the initial collision but then have one of the quarks radiate a gluon that then subsequently splits into a $b\bar{b}$ pair. This kinematic signature will be different from the back-to-back $b\bar{b}$ pairs produced with `mse1 = 5` because these $b\bar{b}$ pairs tend to be closer in angle to each other. The principle reason for using `mse1 = 5` is to speed up production when the effects due to gluon splitting are not of a concern. In this analysis, a `mse1 = 1` background sample was essential to measuring the B_c^\pm meson lifetime.

b hadrons (and charm hadrons) that are created in PYTHIA are decayed using the EVTGEN [33] package, a program especially designed for simulating heavy flavor decays. It includes all known, and in some cases anticipated, decay modes of b hadrons and their daughter particles. These decays are then filtered using `d0_mess`, a package that allows the user to select certain decay modes and place requirements on kinematic properties of the particle.

4.2.2 Detector Simulation

The PYTHIA event generator produces four-vectors of final state particles. However, to correctly model our observation of the data events, these final states need to be passed through a full simulation of the DØ detector. There

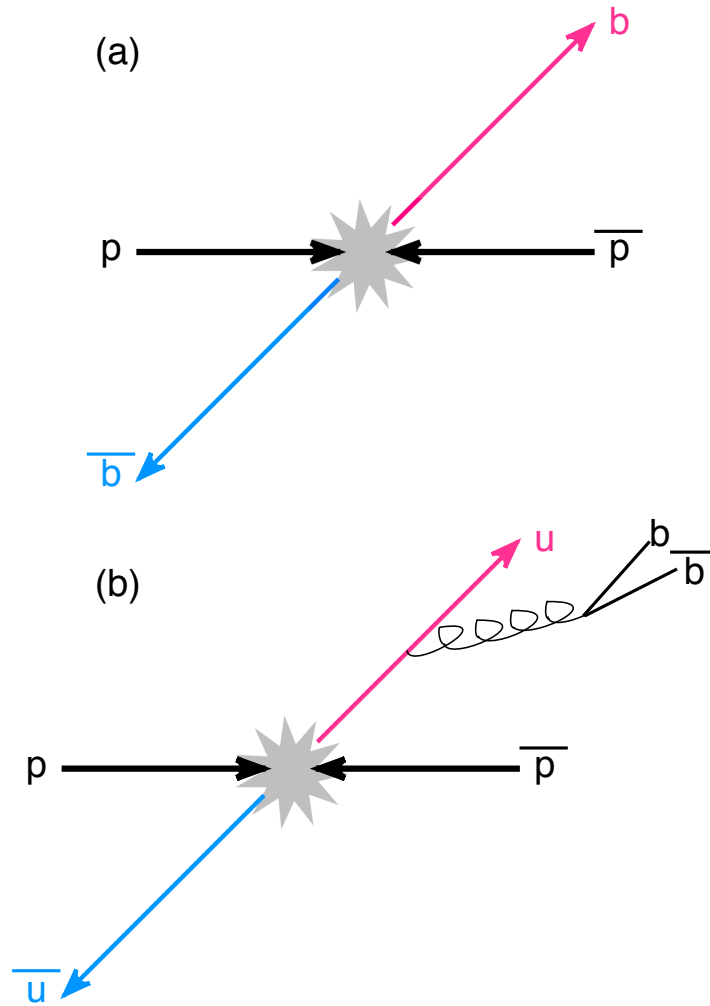


Figure 4.1: Examples of $b\bar{b}$ pairs generated in the PYTHIA stage of MC generation. (a) Using `mse1 = 5` or back-to-back MC production. (b) An example of producing a $b\bar{b}$ pair through gluon splitting that can be obtained through `mse1 = 1` production that also produces $b\bar{b}$ pairs through gluon splitting and flavor creation as well as back-to-back production

are two parts to the detector simulation. The first is DØGSTAR [34] and the second is DØSIM [35]. DØGSTAR is based on the CERN program GEANT [36] that allows one to describe a detector by building up its geometry and its material from a library of known shapes. With DØGSTAR one can trace a particle through the detector and identify where the particle interacts with matter while simulating energy deposits and secondary interactions.

After passing through DØGSTAR, the output goes into DØSIM and it is modified to account for various detector-related effects. These include analog-to-digital conversion within the detector and converting the MC to mimic real data when it is processed through the DØ electronics. Various detector inefficiencies are also included in the simulation as well as noise from the detector and its electronics. DØSIM also takes into account ‘pile-up’, which is the collision of multiple $p\bar{p}$ pairs within a single bunch crossing. The output of DØSIM is the same format as the data that comes out of the detector. This allows it to be processed by DØRECO which reconstructs the Monte Carlo events in the same manner as the data events, but it retains the generator-level information of each event.

The Monte Carlo programs are often updated to include improvements that aid in the proper simulation of the DØ data. The updates are released

as different production versions and the Monte Carlo for this analysis was produced with version p17.09.01. References to ‘p17’ throughout this thesis refer to this production version.

Chapter 5

Analysis

“The most exciting phrase to hear in science, the one that heralds the most discoveries, is not ”Eureka!” (I found it!) but “That’s funny...” ” –Isaac Asimov

The result of this thesis is the measurement of the lifetime of the B_c^\pm meson using the DØ detector. This chapter is devoted to a description of the analysis broken up in the following sections:

- 5.1: Overview of the analysis process
- 5.2: Details on Monte Carlo samples
- 5.3: Pseudo-Proper Decay Length

- 5.4: Event selection and cuts applied to the samples
- 5.5: Signal and background contributions to the final sample
- 5.6: Demonstration of existence of B_c^\pm meson
- 5.7: Lifetime Analysis

5.1 Overview

The point of this analysis was to not only extract the B_c^\pm meson from the terabytes of $D\bar{O}$ data, but also to measure how long it lives before decaying into its daughter particles. For ease of detection, the decay channel that was chosen for this analysis was $J/\psi + \mu^\pm$, with the $J/\psi \rightarrow \mu^+\mu^-$ final state. This three-muon signature is readily accessible particularly with the high-acceptance $D\bar{O}$ muon detectors.

The analysis procedure starts off with selecting a sample of $J/\psi \rightarrow \mu^+\mu^-$ decays in the data and then forming a control sample by vertexing the J/ψ with a single track. A subset of this sample, the signal sample, is selected by demanding that this third track is identified as a muon. There are a total of six contributions to the $J/\psi + \mu$ data sample: five backgrounds and the B_c^\pm signal; these will be discussed in detail in Section 5.5.

Signal Monte Carlo (MC) samples and the data are then used to select criteria that will enhance the signal contribution. The invariant mass of the resulting three-muon system is taken as an estimate of the mass of the B_c^\pm meson. Data and Monte Carlo simulations are used to form templates of this mass distribution for both signal and background components. The decay length is measured as the distance between the reconstructed primary vertex and the secondary vertex formed between the J/ψ and the third muon.

After demonstrating the presence of the B_c^\pm signal and making a qualitative estimate of its short lifetime compared with the other b hadrons, ‘ K -factors’ are used to correct the boost factor estimate due to the escaping neutrino and models are constructed of the lifetime distributions of signal and background components. A log likelihood simultaneous fit to the three-muon invariant mass and lifetime distributions is then made to measure the lifetime of the B_c^\pm meson.

5.2 Monte Carlo Samples

There were several Monte Carlo samples generated to describe both the signal components and one of the backgrounds. These generated samples are described and a discussion of their application will follow in Section 5.5.

5.2.1 Signal MC

To simulate the B_c^\pm properties in this decay channel and to determine appropriate selection criteria and cut values, signal Monte Carlo of the decay $B_c \rightarrow J/\psi\mu\nu$; $J/\psi \rightarrow \mu^+\mu^-$ was generated. The standard $D\bar{O}$ simulation chain was used that is described in detail in Section 4.2. The full decay path of the signal was generated using the default decays of the EVTGEN package. For the Monte Carlo simulated samples used throughout the analysis, the Isgur-Wise semileptonic decay model [44] for B_c^\pm is used. 18662 events were generated in this sample. A separate sample with a phase space decay model was also generated for systematic study purposes. The mass of the B_c^\pm meson was set to 6.30 GeV [51] and its $c\tau$ set to 0.014 cm.

5.2.2 $\psi(2S)$ Monte Carlo

Another viable decay of the B_c^\pm is $B_c \rightarrow \psi(2S)\mu + X$ where $\psi(2S) \rightarrow J/\psi\pi^+\pi^-$. 12350 events containing this decay mode were generated. See Section. 5.5.1 where this process is discussed in more detail.

5.2.3 J/ψ QCD Monte Carlo

To model one of the backgrounds, two large samples of QCD inclusive Monte Carlo were generated, only requiring a generator-level $J/\psi \rightarrow \mu^+\mu^-$ with the only generator-level *d0mess* cuts being on the two muons coming from the J/ψ parent: the first sample had $p_T(\mu) > 2.0$ GeV, which was not an optimal selection due to missing muons with $1 < p_T(\mu) < 2$ GeV that would pass the analysis cuts, and $|\eta(\mu)| < 2.5$ (725000 events generated). To remedy the shortcoming of the high $p_T(\mu) > 2.0$ GeV cut, 1.4×10^6 events of $p_T(\mu) > 1$ GeV and the same η cut were generated. This second sample was used to form a weighting function to be applied to the first sample to correct for the fraction of missing generated events with $1 < p_T(\mu) < 2$ GeV that would pass analysis cuts. It was important that these samples be generated as QCD inclusive (MSEL=1) which includes gluon splitting $g \rightarrow b\bar{b}$ so that the J/ψ and the third muon that are produced are not necessarily roughly back-to-back. That is the case in MSEL=5 ($b\bar{b}$ Monte Carlo) where the J/ψ arises from the decay of a b hadron and the muon from the other b hadron in the event. See Figure 4.1 for a visual description of the two processes.

To obtain sufficient MC statistics, the two samples needed to be combined. The p_T distribution of the softer muon from the J/ψ decay was used

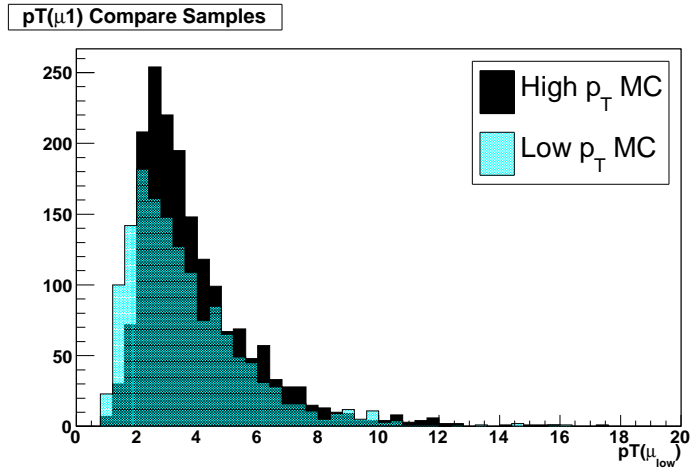


Figure 5.1: p_T of the lower momentum muon from the J/ψ decay.

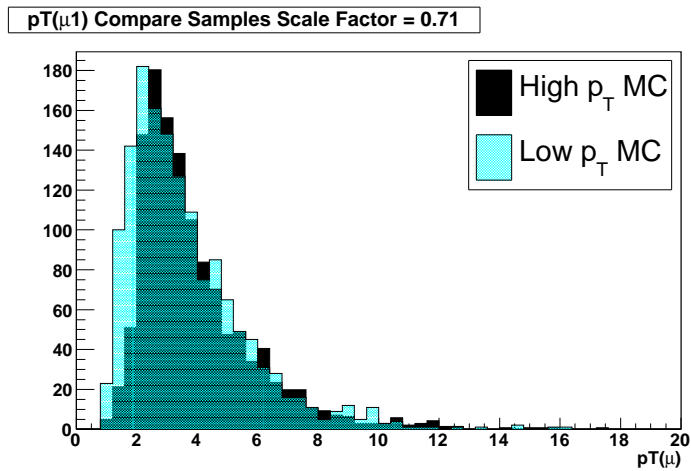


Figure 5.2: p_T of the lower momentum muon coming from the J/ψ after forcing equal normalization at higher p_T .

to determine the weighting mentioned above. Figure 5.1 is the distribution of the $p_T(\mu_{low})$ from the two samples. The distribution of the first MC sample was then scaled so that the number of events with $p_T(\mu) > 4$ GeV was equal. Figure 5.2 shows the resulting overlay of the distribution. The histograms were then divided and smoothed to obtain a weighting function that could be applied to the high- p_T sample; the result of this is shown in Figure 5.3.

The combined J/ψ QCD sample was then run through the same analysis code as the data. Vertexing the J/ψ with a track, and then identifying the track as a muon was then performed as in the data.

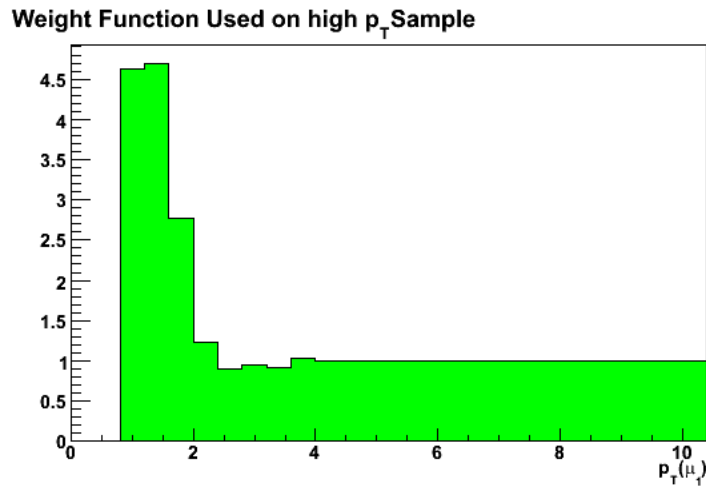


Figure 5.3: Weighting function applied to the first QCD J/ψ MC Sample.

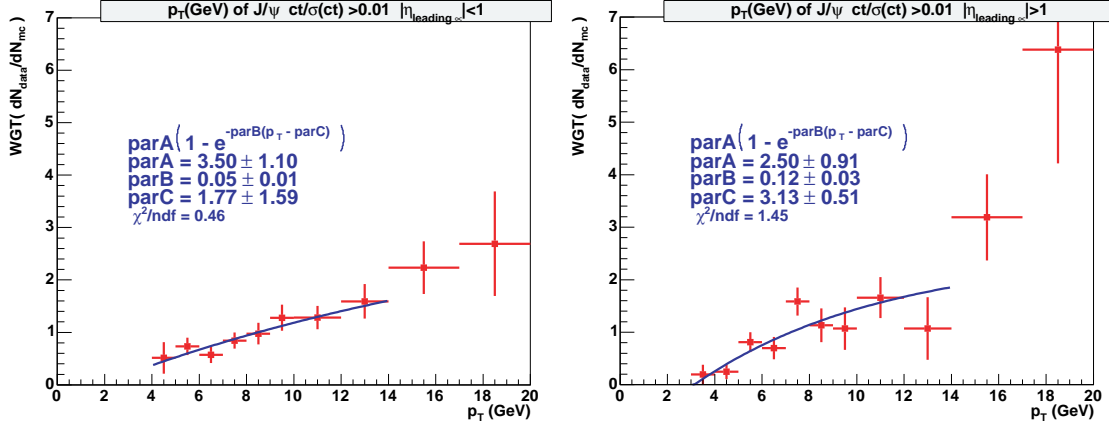
5.2.4 Optimization of MC $p_T(b)$

It is a known effect that the PYTHIA MC generation of b production does not model the true $p_T(b)$ distribution well when compared to data. In addition, the MC samples were not passed through a trigger simulation of the various muon triggers. To alleviate this problem, an iterative weighting process is applied. Weighting functions were found from a detailed study of the kinematic properties of reconstructed J/ψ mesons from B hadrons in the data compared with those observed in the MC as shown in Fig. 5.4 [45]. The weighting function takes as input the p_T of the J/ψ . There are two separate weighting functions as determined by the η of the leading muon from the J/ψ .

5.3 Pseudo-Proper Decay Length

To calculate the lifetime of the B_c^\pm meson, as will be done in the next chapter, it is first important to define the Pseudo-Proper Decay Length or PPDL. The lifetime of the B_c^\pm , τ , is related to the decay length, L , by the relation:

$$L = c\tau\beta\gamma = c\tau\frac{p}{m}, \quad (5.1)$$

Figure 5.4: Monte Carlo weighting function for $p_T(b)$

where $c\tau$ is the proper decay length, p is the total momentum, and m is the mass of the B_c meson. In the transverse plane the relationship can be written:

$$L_{xy} = c\tau \frac{p_T}{m}, \quad (5.2)$$

where p_T is the momentum of the B_c in the transverse plane and L_{xy} is the transverse decay length. The decay length of the B_c^\pm in the transverse plane is defined as the displacement of the B_c^\pm vertex from the primary vertex projected onto the transverse momentum of the $J/\psi\mu$ system. The primary vertex (PV) as determined by the BANA package is used where information from both the average x - y position of the beamspot and the other tracks

in the event is considered [50]. The x and y locations of the PV fluctuate within $40 \mu\text{m}$ between events. The z location of the PV is roughly a Gaussian distribution with a spread of 28 cm. If vertex points from the primary vertex to the secondary vertex in the transverse plane, we then have:

$$L_{xy} = \frac{\vec{X} \cdot \vec{p}_T(J/\psi\mu)}{|\vec{p}_T(J/\psi\mu)|}. \quad (5.3)$$

However, when the B_c^\pm decays in the semileptonic channel, it is not fully reconstructed due to the neutrino that escapes undetected. Therefore, the p_T of the B_c^\pm is not determined. A correction factor, K , must be introduced and the p_T of the $J/\psi\mu$ system is used as a close approximation. A K -factor is therefore defined as:

$$K = \frac{p_T(J/\psi\mu)}{p_T(B_c)}. \quad (5.4)$$

To obtain the B_c^\pm lifetime, the pseudo-proper decay length (PPDL) is measured. It is represented by λ and is then defined as:

$$\lambda = L_{xy} \frac{m(B_c)}{p_T(J/\psi\mu)} = c\tau \frac{1}{K}. \quad (5.5)$$

The K -factor is determined using signal Monte Carlo samples and is applied statistically by smearing the exponential decay distribution when extracting the $c\tau(B_c)$ from the pseudo-proper decay length in the lifetime fit. The mass

of the B_c is taken from the precise CDF result $M(B_c) = 6274.1 \pm 3.2 \pm 2.6$ MeV [51].

The K -factor distribution determined as above is shown in Fig. 5.5. Note that it includes values of the K -factor above 1.0 due to resolutions and measurement uncertainties. Since part of the signal component contains the $\psi(2S)$ feed-down component, a separate K -factor distribution is needed for this component. Similar to the difference observed in the mass distributions, Fig. 5.6 shows the expected difference in the K -factor distributions due to the missing $\pi^+\pi^-$ in the feed-down channel.

The K -factor distribution was also broken up in bins of $M(J/\psi\mu)$:

- $M(J/\psi\mu) < 4.0$ GeV,
- $4.0 < M(J/\psi\mu) < 4.5$ GeV,
- $4.5 < M(J/\psi\mu) < 5.0$ GeV,
- $5.0 < M(J/\psi\mu) < 5.5$ GeV,
- $5.5 < M(J/\psi\mu) < 6.0$ GeV,
- $6.0 < M(J/\psi\mu) < 6.5$ GeV,
- $M(J/\psi\mu) > 6.5$ GeV,

as shown in Fig. 5.7. As $M(J/\psi\mu)$ approaches the B_c mass, less energy and momentum is being carried off by the neutrino and the K -factor distribution is narrower and peaked more towards 1.0, i.e., provides better resolution on estimating the boost factor. To take advantage of these particular events with better resolution, the K -factor is applied in the analysis in the indicated bins.

5.4 Event Selection

With the signal Monte Carlo now in hand we move on to selecting a data sample. The Monte Carlo aided in the determination of the selection criteria for the final data sample.

5.4.1 Data Set

This measurement uses the large preselected single muon data sample corresponding to approximately 1.3 fb^{-1} of integrated luminosity [28] collected by the DØ detector between April 2002 and March 2006. The single muon data sample is an object skim and is a combination of several other object skims with varying p_T requirements listed below:

- A single, central muon with $p_T > 8 \text{ GeV}$,

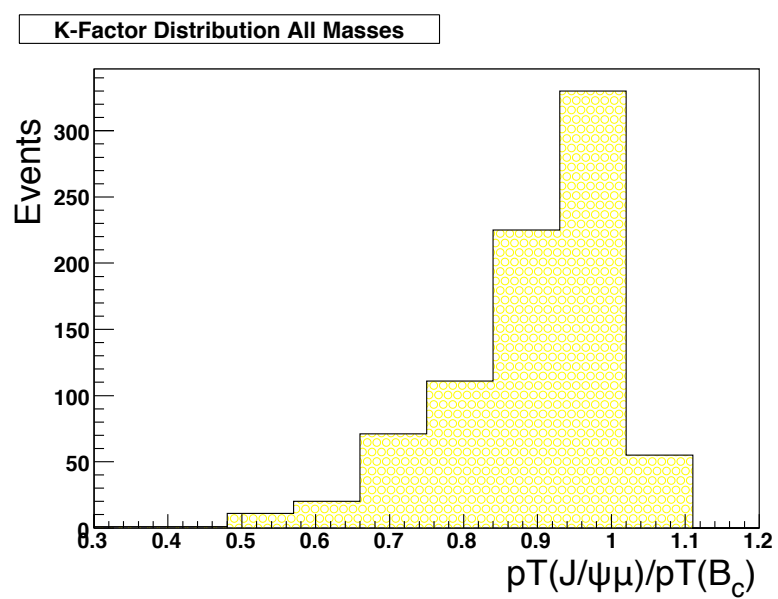


Figure 5.5: K -factor distribution as determined in the signal Monte Carlo sample.

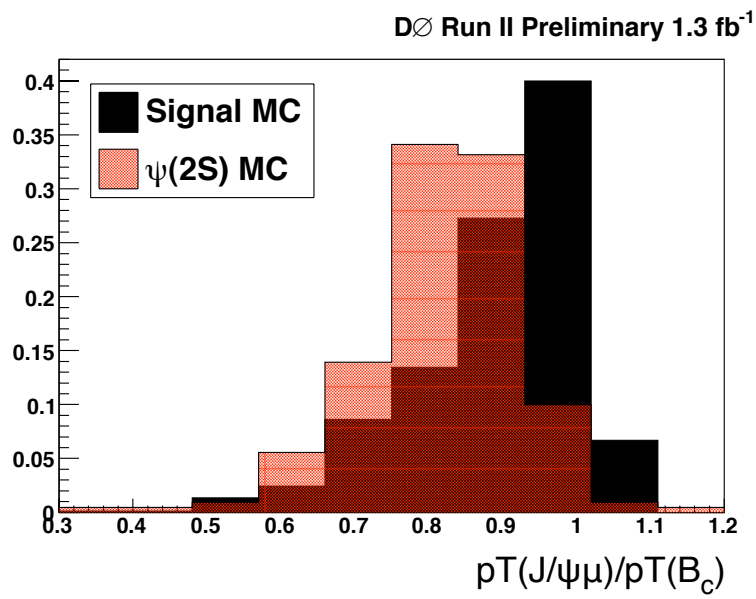


Figure 5.6: K -factor distribution in the $B_c \rightarrow \psi(2S)\mu\nu$ signal sample compared to the $B_c \rightarrow J/\psi\mu\nu$ signal MC sample.

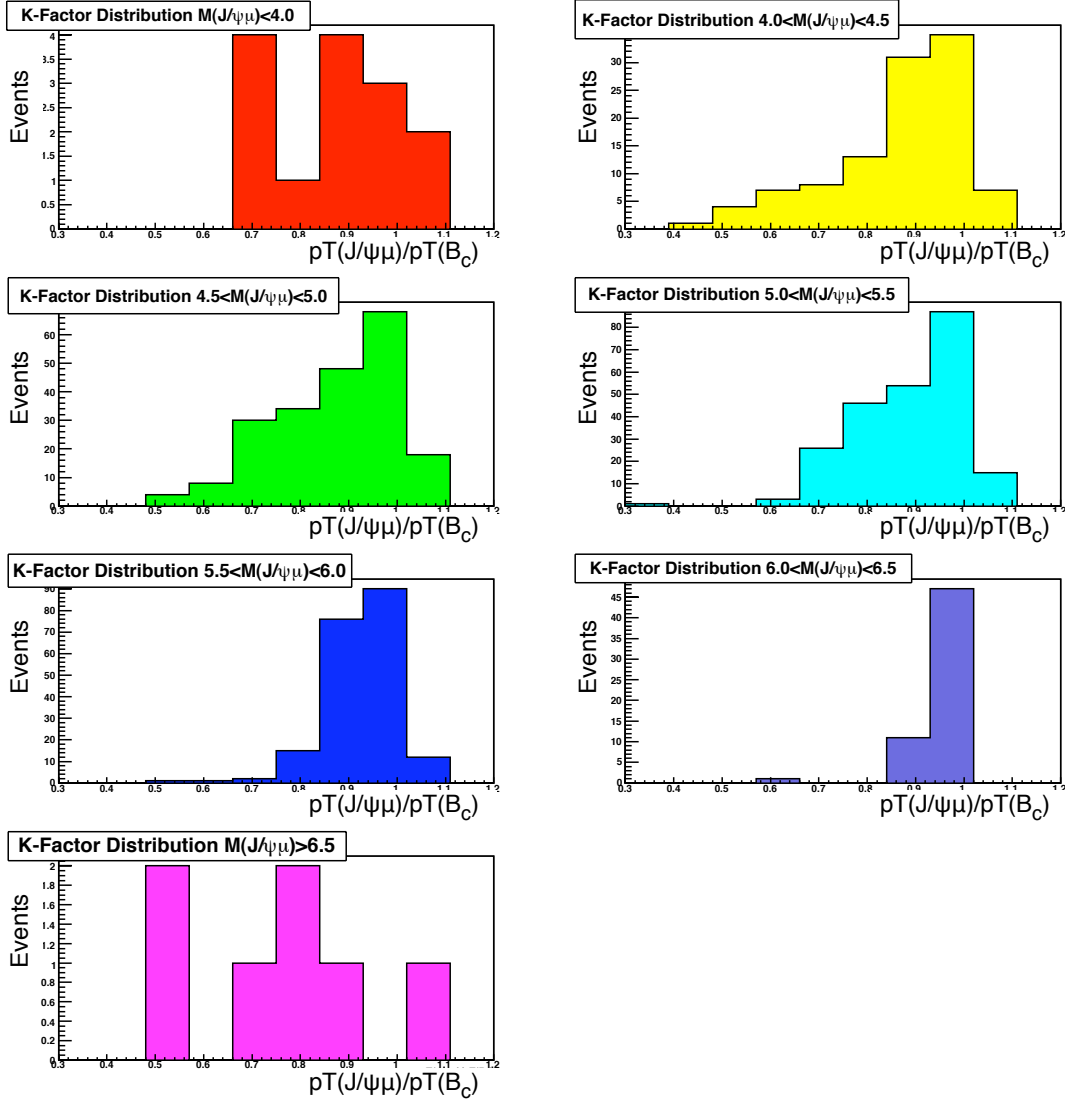


Figure 5.7: K -factor distribution separated in bins of $M(J/\psi\mu)$ as determined in the signal Monte Carlo.

- Two muons, one of which has a p_T of at least 1 GeV in the central region, $|\eta| < 1$,
- A muon with a $p_T > 5$ GeV, plus two tracks with $p_T > 5$ GeV and $p_T > 8$ GeV, respectively,
- A muon with $p_T > 10$ GeV in the central region plus two jets, each with $p_T > 8$ GeV,
- A muon plus two jets, each with $p_T > 10$ GeV. The muon is required to have $p_T > 4$ GeV, $nseg > 3$, and be within a jet.

In principle, any trigger could contribute to this sample. Events were reconstructed using the standard DØ software suite [29] after the removal of events that enter the sample only via impact parameter biasing triggers (see next subsection). Information only from the muon and tracking systems was used in this analysis.

5.4.2 Preventing Trigger Bias

While the majority of events selected in the inclusive muon sample satisfy single muon trigger requirements, it is possible to have events trigger only on lifetime-biasing triggers. To avoid this, events that triggered exclusively

on impact parameter biasing triggers were removed from the event selection. These triggers are removed to eliminate the need to determine their trigger efficiencies versus decay length and their subsequent impact on this lifetime analysis. See the Appendix for a listing of the triggers which are removed.

5.4.3 J/ψ Selection

The analysis starts by using the single muon data sample. Running over this sample of events, a subsample of events each containing at least one J/ψ candidate is formed using the BANA JpsiFinder package [31]. The following cuts were applied to identify a J/ψ candidate:

- two certified muons [48] of opposite electric charge;
- $p_T > 1.0$ GeV for each muon;
- each muon must have at least two hits in the CFT;
- at least one of the muons must have $nseg = 3$, where $nseg$ is the number of reconstructed segments in the muon system assigned to the muon;
- if $nseg > 0$, then $p_T > 1.5$ GeV, i.e., allow $p_T < 1.5$ only for those muons with $nseg = 0$;

- If a muon has $nseg = 0$
 - $p_T(\mu^+\mu^-) > 4.0$ GeV;
 - $nmtc() \geq 0$, i.e., a muon-in-calorimeter-track (MTC) is allowed;
 - $CalEsig() > 0.015 \cdot CalNLayer()$, where $CalEsig$ is the significance of energy assigned to a MTC track, and $CalNLayer$ is the number of calorimeter layers associated with an MTC track.
 - $p < 7$ GeV;
 - $p_T(\mu^2) > 2.5$ GeV;
 - χ^2 of global muon fit less than 25 for both particles;
- $M(\mu^+\mu^-) > 2.5$ GeV;
- If $M(\mu^+\mu^-) > 3.6$ GeV (high di-muon mass selection):
 - $nseg > 1$ for both muons;
 - $p_T > 2.5$ GeV for both muons.

From this sample, the mass requirement was further tightened to $2.9 < M(\mu^+\mu^-) < 3.26$ GeV (see mass window in Fig. 5.13). The muon momenta following the mass-constrained fit to the J/ψ mass of 3.096 GeV [3] from the BANA package is used in the selections below.

5.4.4 J/ψ + Track Selection

Once a J/ψ has been found, an additional track that can be associated with the J/ψ vertex is sought, which will be referred to as the third track. The following are the cuts applied that result in a J/ψ + track candidate. Figure 5.8 shows the distribution of the various major selection variables for the J/ψ + track sample and the J/ψ + μ sample (described in the following Subsection 5.4.5) compared to those observed in the signal MC and the value of selection variable used for the cut.

- Each muon from the J/ψ must have a least one hit in the SMT while the third track must have two;
- $\chi^2 < 49$ of the J/ψ + μ vertex;
- $p_T(\text{third track}) > 3$ GeV;
- $p(\text{third track}) > 4$ GeV;
- $p_T(J/\psi + \text{track}) > 5$ GeV;
- $\chi^2(J/\psi + \text{track}) < 16$;
- angle between J/ψ and third track < 1 rad;

- $\cos \theta$ between any two muons < 0.99 ; and
- if more than one $J/\psi + \text{track}$ candidate is present in an event, the candidate with the lowest χ^2 of the $J/\psi + \text{track}$ vertex is selected.

5.4.5 $J/\psi + \mu$ Selection

The $J/\psi + \mu$ sample, which will be defined as the final signal sample, has three additional requirements, i.e., it is a subset of the $J/\psi + \text{track}$ sample described above. To obtain this sample, additional requirements listed below are placed on the $J/\psi + \text{track}$ sample. The “3rd track” identified as a muon, will from this point be defined as the “third muon”, i.e., μ_3 :

- The third track must be identified as a muon [48];
- $n_{\text{seg}}(\mu_3) = 3$, i.e., only high-quality muons are desired;
- $|\text{sctime}(A)| < 10$ ns, i.e., A-layer scintillator times between ± 10 ns of the beam crossing to reduce fake muon background.

5.5 Contributions to the $J/\psi + \mu$ Sample

There are several different contributions to the $J/\psi\mu$ sample:

- B_c^\pm signal;

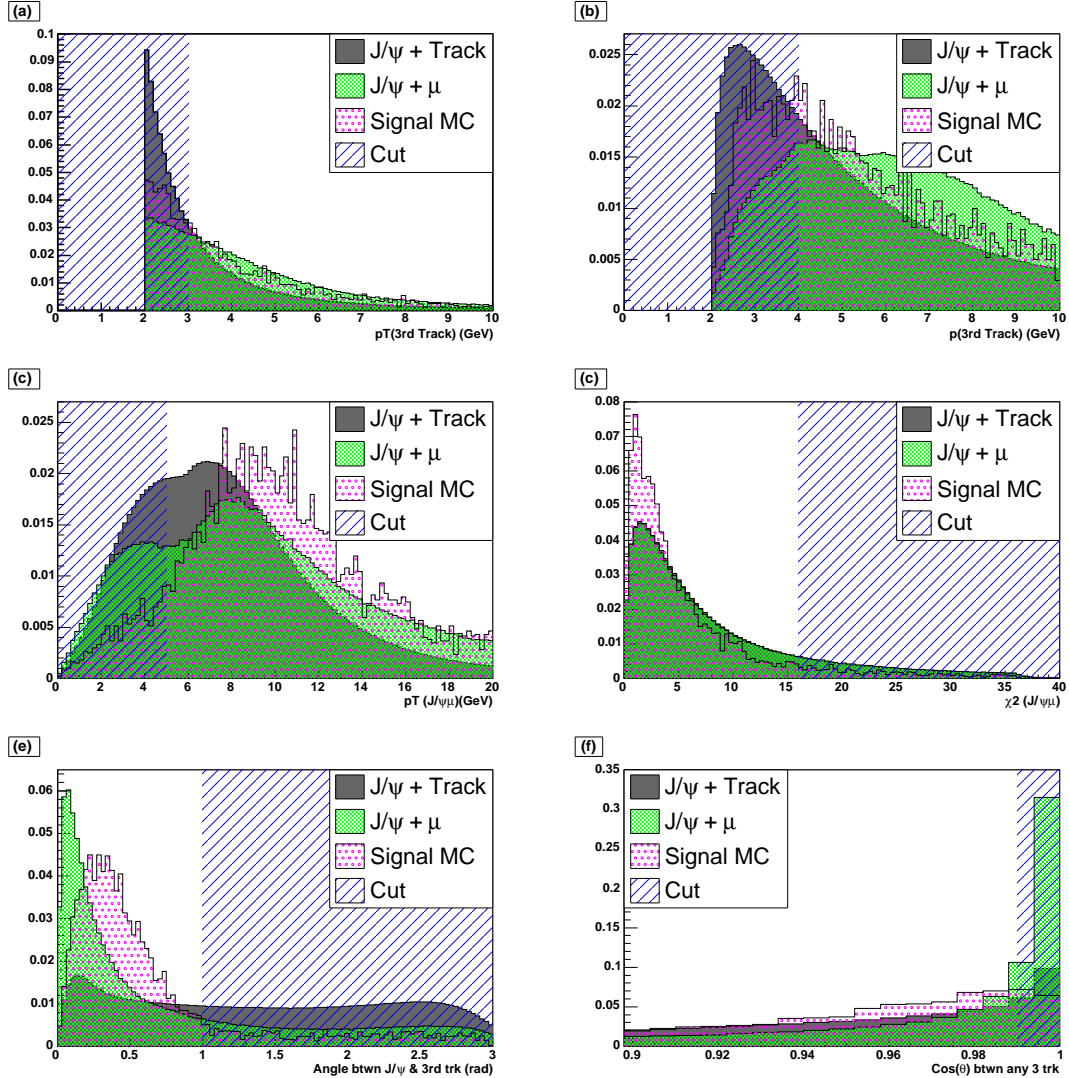


Figure 5.8: Variables used to separate signal from the background: (a) transverse momentum, p_T of the third track; (b) momentum, p of the third track; (c) p_T of $J/\psi + \text{track}$ vertex; (d) χ^2 of $J/\psi + \text{track}$ vertex; (e) angle between J/ψ and third track; and (f) maximum $\cos \theta$ between any two tracks.

- a real J/ψ vertexing with a fake μ ;
- a fake J/ψ vertexing with a real μ ;
- a real J/ψ and a real μ but neither from a B_c^\pm meson decay;
- $B^+ \rightarrow J/\psi + K^+$ followed by the K decaying in flight to a μ thus having the same signature as B_c^\pm meson;
- prompt J/ψ , i.e., due to $c\bar{c}$ production rather than via b hadron decay.

These different contributions will be described in further detail in the following sections.

Due to the missing neutrino, an exclusive decay resulting in an invariant mass peak at the mass of the B_c^\pm is not possible; however, the invariant mass of the $J/\psi + \mu$ combination, i.e., the trimuon invariant mass, can still be used to characterize and separate each of the components.

A description of each component is given along with the mass template that will be used in a mass-only fit demonstrating that B_c^\pm signal exists in the sample. These mass templates subsequently will then be used in a simultaneous mass and PDDL fit which is the ultimate goal of this analysis. The modeling of the PDDL distributions will be discussed in Section 5.7.

5.5.1 B_c^\pm Signal

The B_c^\pm signal Monte Carlo described in Section 5.2.1 is used to find the mass distribution shown in Fig. 5.9 that is used as a mass template for the signal.

$\psi(2S)$ Feed-Down Channel

Another signal decay channel is $B_c \rightarrow \psi(2S)\mu\nu$ where $\psi(2S) \rightarrow J/\psi\pi^+\pi^-$. Therefore, some of the events in the $J/\psi + \mu$ sample could be arising from this feed-down channel. Theoretical estimates predict the $B_c \rightarrow J/\psi\mu + X$ branching fraction to be approximately 5 to 100 times larger than that of $B_c \rightarrow \psi(2S)\mu + X$ [22, 49]. To estimate the fraction of events due to this feed-down component, the efficiency of the selection for the two signal components was found to be $\epsilon(B_c \rightarrow J/\psi\mu X) = 0.0443 \pm 0.0015$ (stat) and $\epsilon(B_c \rightarrow \psi(2S)\mu X) = 0.0352 \pm 0.0017$ (stat) using the signal MC samples. The ratio of these efficiencies is 0.79 ± 0.04 (stat). In the worst case scenario, the $J/\psi\mu$ channel is 5 times as likely as the feed down channel. In this case the feed-down channel can comprise a fraction of up to $(0.79 \pm 0.04) \cdot 0.17 = 0.13 \pm 0.01$ of the signal. For the central value, the fraction of this feed-down channel is taken to be one-half of this value, i.e.,

6.5%, and it is later varied widely from 0% to 13% in the estimate of the systematic uncertainty due to this additional signal channel.

The $B_c \rightarrow \psi(2S)\mu\nu$ MC is used to determine the shape of the $M(J/\psi\mu)$ distribution as shown in Fig. 5.10. In comparison with the $B_c \rightarrow J/\psi\mu\nu$ MC, this distribution is shifted down in mass as expected due to the pions not reconstructed in the decay $\psi(2S) \rightarrow J/\psi \pi^+\pi^-$.

5.5.2 Real J/ψ & Fake μ

To model this component, the invariant mass of the J/ψ and vertexed track in the relevant $J/\psi + \text{track}$ data sample described in Section 5.4.4 is used. Given the robust DØ muon detectors, the fake muon rate is small but not zero, and primarily due to decays in flight of $\pi^\pm \rightarrow \mu^\pm\nu$ and $K^\pm \rightarrow \mu^\pm\nu$, where the charge conjugate channel is understood. To find the fraction of events contributing to this component, the $B^+ \rightarrow J/\psi K^+$ decay is used. The K^+ meson will decay in flight to a muon and neutrino hence enter the $J/\psi + \mu$ final sample. As shown in Figure 5.11 a fit was made to the B^+ mass peak in both the $J/\psi + \mu$ sample and the $J/\psi + \text{track}$ sample and the ratio of the number of B^+ events in the $J/\psi + \mu$ sample to that found in the $J/\psi + \text{track}$ sample is taken as the fraction of events that are due to a real

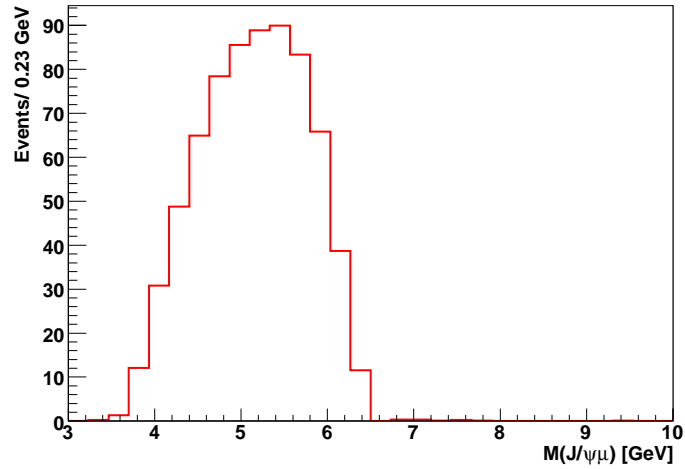


Figure 5.9: Distribution of $M(J/\psi\mu)$ in the B_c^\pm signal Monte Carlo sample.

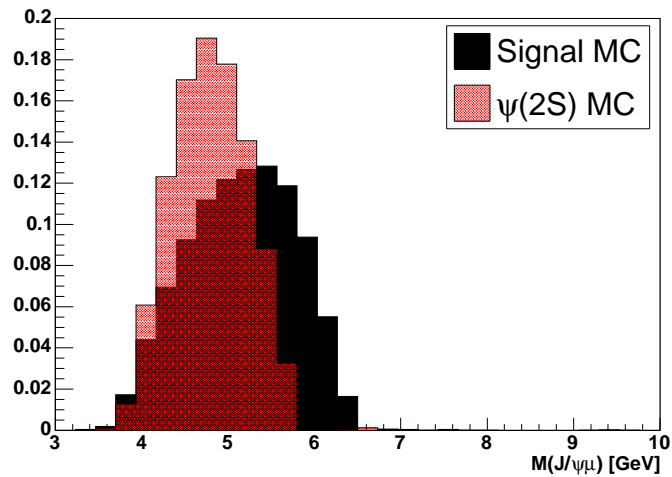


Figure 5.10: Distribution of $M(J/\psi\mu)$ in the $B_c \rightarrow \psi(2S)\mu\nu$ signal Monte Carlo sample compared to that from $B_c \rightarrow J/\psi\mu\nu$.

J/ψ but a fake μ . Contributions due to $B^+ \rightarrow J/\psi\pi^+$ and $B_c^+ \rightarrow J/\psi\pi^+$ were estimated to be negligible.

The fraction of events thus estimated to arise from fake muons associated with real J/ψ mesons is 0.0338 ± 0.0021 . The mass distribution of this component is shown in Fig. 5.12; a peak due to $B^\pm \rightarrow J/\psi K^\pm$ can also clearly be seen in this distribution. A sideband subtraction is performed using the mass sidebands of the J/ψ as described later to remove the component due to fake J/ψ and fake muons.

5.5.3 Fake J/ψ & Real μ

Events containing an identified J/ψ candidate within the prescribed $M(\mu^+\mu^-)$ mass range but that are actually due to combinatorial background are covered by this component. The distributions that will be used to describe this components are formed from events from the J/ψ mass sidebands. Fitting to the J/ψ mass before all cuts are applied, the sideband regions were defined to be 3σ on either side of the J/ψ peak (defined as $2.9 < M(J/\psi\mu) < 3.26$ GeV), i.e., events within $2.62 < M(J/\psi\mu) < 2.80$ GeV or $3.40 < M(J/\psi\mu) < 3.58$ GeV, i.e., see Fig. 5.13.

The ratio of events in the $J/\psi + \mu$ sample that are within the two sideband

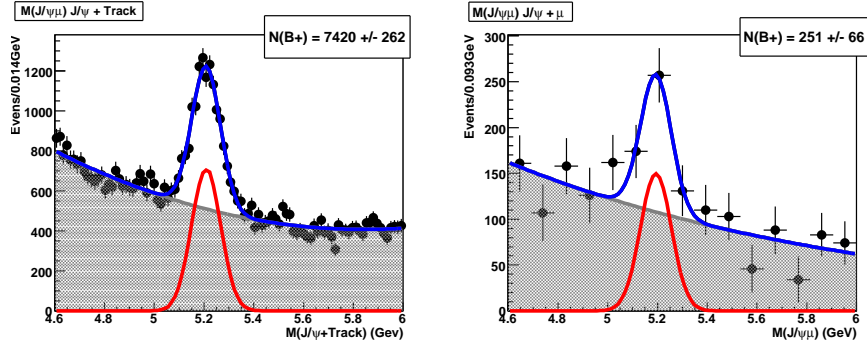


Figure 5.11: B^+ mass peak fit in the (a) $J/\psi + \text{track}$ data sample and the (b) $J/\psi + \mu$ sample. The ratio of fitted number of B^+ candidates is used to estimate the fraction of candidates due to real J/ψ but fake μ .

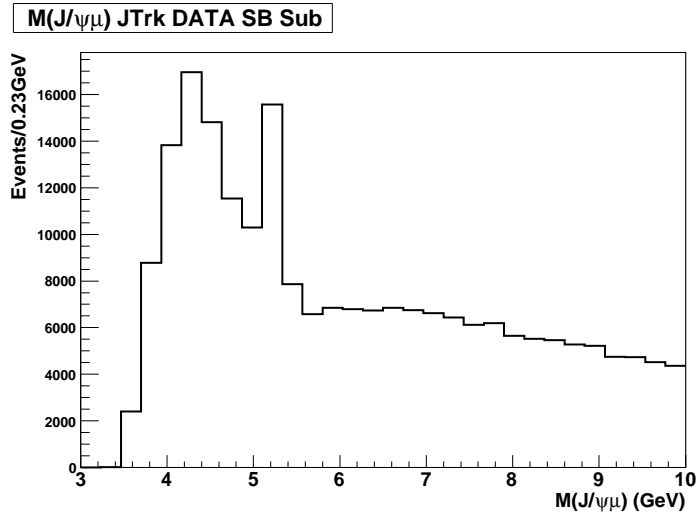


Figure 5.12: Distribution of $M(J/\psi\mu)$ within the $J/\psi + \text{track}$ sample, clearly showing the B^+ peak at a mass of ~ 5 GeV

regions to the number total number within the J/ψ signal region is then taken as the fraction of total ratio that comprise this background. This fraction is found to be 0.6672 ± 0.0036 and the mass distribution of this component estimated from the data is shown in Fig. 5.14.

5.5.4 Real J/ψ & Real μ

This is a background where both a real J/ψ and a real μ are produced, but neither comes from a B_c^\pm decay and they are incorrectly vertexed together. This component is dominated by $b\bar{b}$ backgrounds, where one b hadron decays to $J/\psi + X$ and the other decays semileptonically to a muon (or via a cascade decay $b \rightarrow c \rightarrow \mu$). The requirement that the J/ψ and μ_3 be close in angle increases the accepted fraction of $b\bar{b}$ production via gluon splitting. To model this background, the J/ψ QCD Monte Carlo described in Section 5.2.3 is used. A requirement is placed that the parent of the J/ψ does not arise from prompt $c\bar{c}$ (estimated using the data as separate component described later) or a B_c^\pm . The resulting distribution that will be used as a mass template is shown in Fig. 5.15. Note that the $B^+ \rightarrow J/\psi + K$ component, as discussed in the following section, is subtracted off.

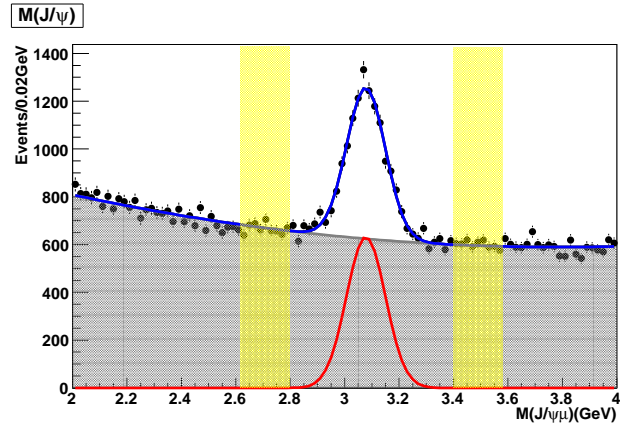


Figure 5.13: Fit of the J/ψ mass in the $J/\psi + \mu$ sample with the yellow band delineating the two sideband regions.

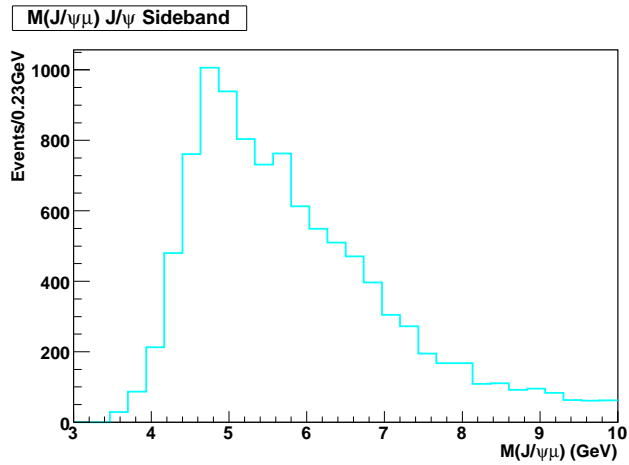


Figure 5.14: Distribution of $M(J/\psi\mu)$ within the J/ψ sideband sample. This is the mass template for the fake J/ψ and real μ component.

5.5.5 B^+

The decay $B^+ \rightarrow J/\psi K^+$ followed by the decay in flight of the K to a muon results in a mass peak right in the middle of the signal mass region so it is important to correctly and carefully model this feature. A fit was made to the mass of the B^+ in the $J/\psi + \mu$ data sample. This fitted distribution, as shown in Fig. 5.16, was then used as a mass template for the B^+ component. Determining this mass distribution from the data itself removes uncertainty in the modeling of the width of this mass distribution.

Since this component is modeled with the data, this particular component needs to be removed from the J/ψ QCD Monte Carlo sample. Using the Monte Carlo truth information, those events due to $B^+ \rightarrow J/\psi K^+$ were subtracted from the J/ψ QCD Monte Carlo mass shape.

5.5.6 Prompt $J/\psi + \mu$

One has to take into account the $c\bar{c}$ contribution to the signal where a prompt J/ψ is vertexed with a muon. Using the $J/\psi + \mu$ data sample, those events that have a negative decay length on the J/ψ vertex are used to estimate the prompt background since this component should be symmetric with respect to zero decay length due to resolution effects. Initially the $J/\psi +$

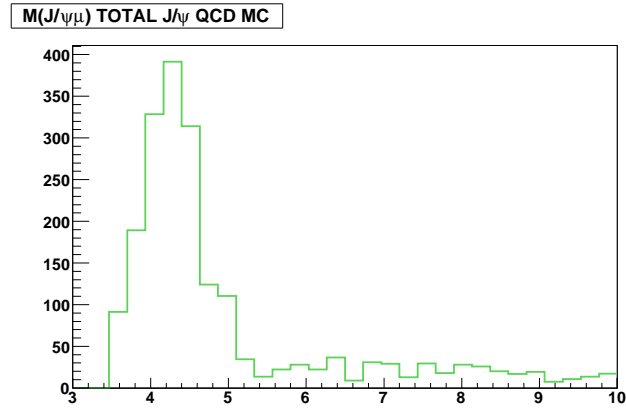


Figure 5.15: Distribution of $M(J/\psi\mu)$ in the J/ψ QCD MC sample that is used to model the mass of the real J/ψ and real μ background component.

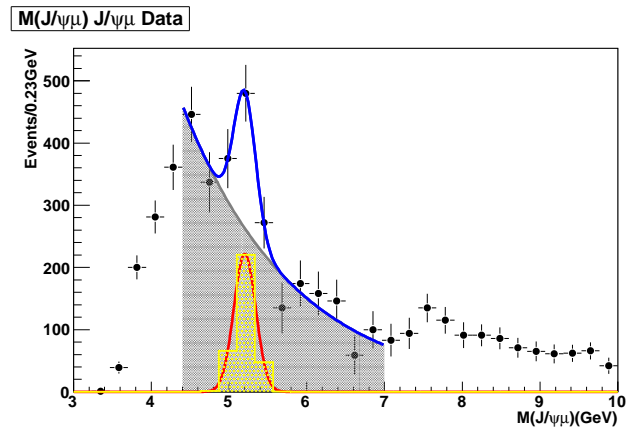


Figure 5.16: Fit of the B^+ peak in the $J/\psi + \mu$ mass distribution. The yellow histogram is an estimate of the mass template that is used in the full fit.

track data sample was considered to determine the shape of the prompt mass component, but it was observed to be significantly different in the $J/\psi + \text{track}$ sample both in the data and in the J/ψ QCD MC sample. The determination of this shape was statistically limited in the $J/\psi + \mu$ sample so a fit was applied to the distribution as shown in Fig. 5.17 to estimate the prompt mass distribution used throughout the analysis for this component.

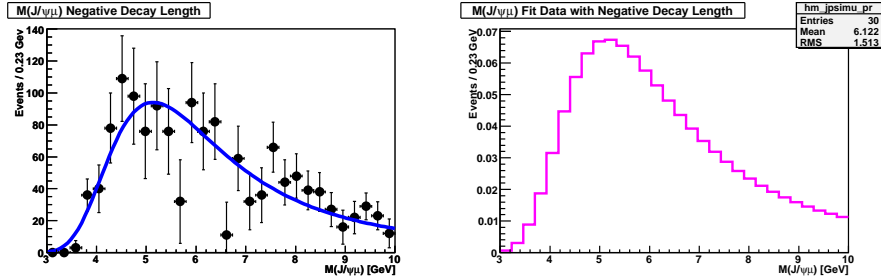


Figure 5.17: Mass distribution of the events in the $J/\psi + \mu$ data sample with negative decay length: (a) distribution with a fit to a Landau function; and (b) histogram based on the fit in (a) and used as the mass template.

5.6 Demonstration of B_c^\pm Signal

Now that the mass templates have been determined, we first demonstrate the presence of the B_c^\pm signal and proper behavior of the signal component within the $J/\psi + \mu$ data sample before measuring the B_c^\pm lifetime. The

following shows that the signal sample does in fact have a shorter lifetime than the rest of the sample as expected.

5.6.1 Presence of B_c^\pm Signal

To check on the validity of the modeling of the $M(J/\psi\mu)$ mass distribution, a mass-only fit is performed to check for both an adequate description of the data and for the presence of B_c signal. Taking the mass distributions of the six components described in the previous section, and fitting to the mass distribution in the data sample, the fit result shown in Fig. 5.18 is found. Fixed in this fit is the fraction of fake μ events taken from the fraction determined in the $J/\psi + \text{track}$ sample as well as the sideband fraction. Since the sample without additional requirements is overwhelmingly background, additional cuts are placed in an effort to further suppress background and check for the presence of the signal.

The first step is to place a requirement on the transverse decay length significance: $L_{xy}/\sigma(L_{xy}) > 4$, where L_{xy} is the transverse decay length between the primary vertex (described earlier) and the vertex formed from the J/ψ and μ_3 , and $\sigma(L_{xy})$ is the uncertainty on L_{xy} due to propagation of track parameter errors to the vertices. The result is shown in Fig. 5.19. Note that

new fits were performed to determine the fake μ fraction and the sideband fraction following the decay length significance cut. For $L_{xy}/\sigma(L_{xy}) > 4$, the fake μ component is estimated to be 0.0403 ± 0.025 and the sideband fraction to be 0.3959 ± 0.0102 . The different $M(J/\psi\mu)$ distributions have all been remade with the decay length significance cut applied. As expected, the prompt component has now dropped to a very small contribution and the B^+ contribution is much more apparent.

We next subtract the J/ψ sideband component, see Fig. 5.20. This nicely shows that, especially around the B^+ , there is an excess that can only be due to the signal component. For demonstrating the presence of the signal component even more clearly, the B^+ component is subtracted, leaving a fit to the mass distribution that now only has components from the J/ψ QCD MC (the real J/ψ and real μ background), signal, prompt and $J/\psi + \text{track}$ (real J/ψ and fake μ background), see Fig. 5.21.

At this point, and with the fit shown in Fig. 5.21, the significance of the signal component can be determined. The total number of data candidates in the distribution is 1033. The fitted number of the events due to the signal component is 242 ± 38 . The probability for the signal to fluctuate down to the background is equivalent to 6.4σ . The probability for the background

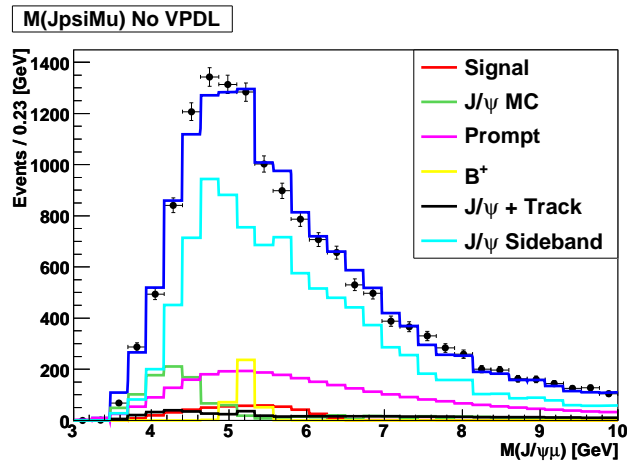


Figure 5.18: Fit to the mass of the $J/\psi + \mu$ vertex with all components and no additional cuts applied.

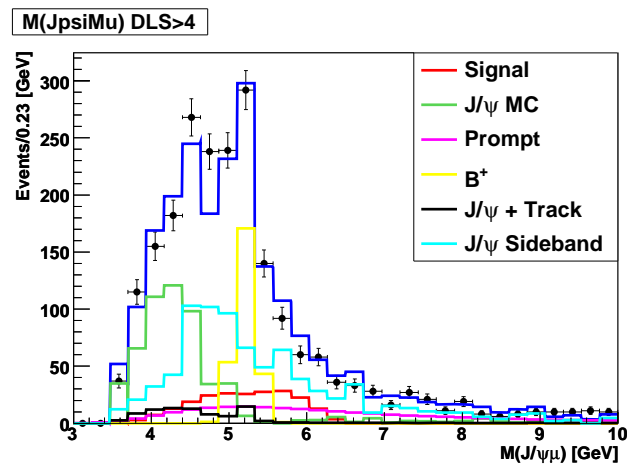


Figure 5.19: Fit to the mass of the $J/\psi + \mu$ vertex with all components and decay length significance $L_{xy}/\sigma(L_{xy}) > 4$ required.

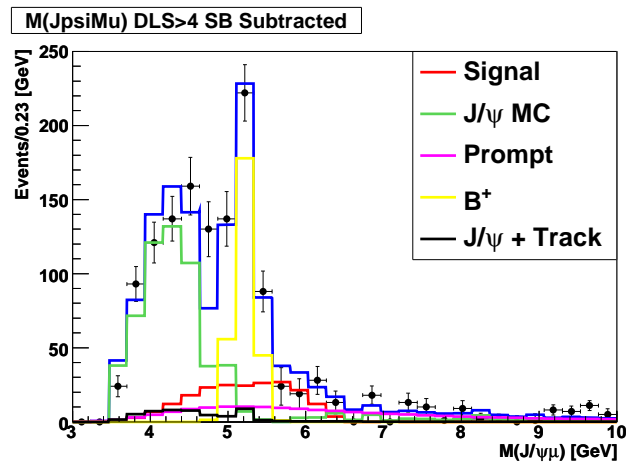


Figure 5.20: Fit to the mass of the $J/\psi + \mu$ vertex with J/ψ mass sideband subtracted and decay length significance $L_{xy}/\sigma(L_{xy}) > 4$ required.

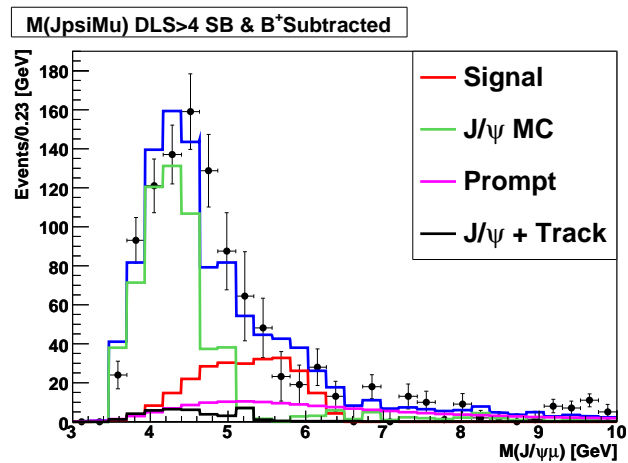


Figure 5.21: Fit to the mass of the $J/\psi + \mu$ vertex with J/ψ mass sideband and B^+ component subtracted and decay length significance $L_{xy}/\sigma(L_{xy}) > 4$ required.

to fluctuate up to the total number of events or more is 4.7×10^{-7} , i.e., equivalent to $> 5\sigma$. Such lifetime-biasing cuts will not be applied in the full simultaneous fit, and the signal significance will be even greater.

5.6.2 Demonstration of Short Signal Lifetime

A similar test can be made cutting progressively harder on the pseudo-proper decay length (PPDL) of the $J/\psi + \mu$ vertex. A J/ψ mass sideband subtraction is made to more clearly distinguish the important components. As shown in Fig. 5.22, when a cut of $\text{PPDL} > 0$ is applied, the prompt component is decreased by a factor of approximately two compared to no PPDL cut, as expected since it should be symmetric around zero. The B_c meson is expected to have a shorter lifetime than the other b hadrons. As the cut value of PPDL is further increased, the relative fraction of the B_c signal increases. However, as the cut value is increased to even larger values, the fraction of signal component drops and for large PPDL values, the only significant components are those due to the long-lived $b\bar{b}$ estimated from the J/ψ QCD MC and that due to the B^+ . This test demonstrates the validity of the modeling of the $M(J/\psi\mu)$ distributions, particularly in the important positive PPDL region, both at small and large values, and also provides a

qualitative comparison that the B_c meson has a significantly shorter lifetime than the other b hadrons.

5.7 Lifetime Analysis

Now that we have demonstrated that the B_c^\pm exists within the data, we are finally at the point where the lifetime of the B_c^\pm meson can be measured. The lifetime analysis is performed over the set of data defined in Section 5.4.5. In addition the mass window on the $J/\psi + \mu$ vertex must lie between $3.0 < M(J/\psi\mu) < 10.0$ GeV. The sample contains 14753 events. An unbinned log likelihood fit is made maximizing the log likelihood:

$$\log(\mathcal{L}) = \log \left(\prod_i (f_{jtrk} \mathcal{F}_{jtrk}^i + (1 - f_{jtrk}) \mathcal{F}_{jmu}^i) \right), \quad (5.6)$$

where f_{jtrk} is the fraction of the $J/\psi + \text{fake } \mu$ component and \mathcal{F}_{jtrk} is the model of the lifetime distribution from the $J/\psi + \text{track}$ sample, described later. The product is over all the events in the data signal sample.

Digging deeper into Eq. 5.6 and looking more closely at what is involved in the \mathcal{F}_{jmu}^i term:

$$\begin{aligned} \mathcal{F}_{jmu}^i = f_{sb} \mathcal{F}_{sb}^i + (1 - f_{sb}) (f_{sig} \mathcal{F}_{sig}^i + f_{jmc} \mathcal{F}_{jmc}^i + f_{bp} \mathcal{F}_{bp}^i \\ + (1 - f_{sig} - f_{jmc} - f_{bp}) \mathcal{F}_{pr}^i), \end{aligned} \quad (5.7)$$

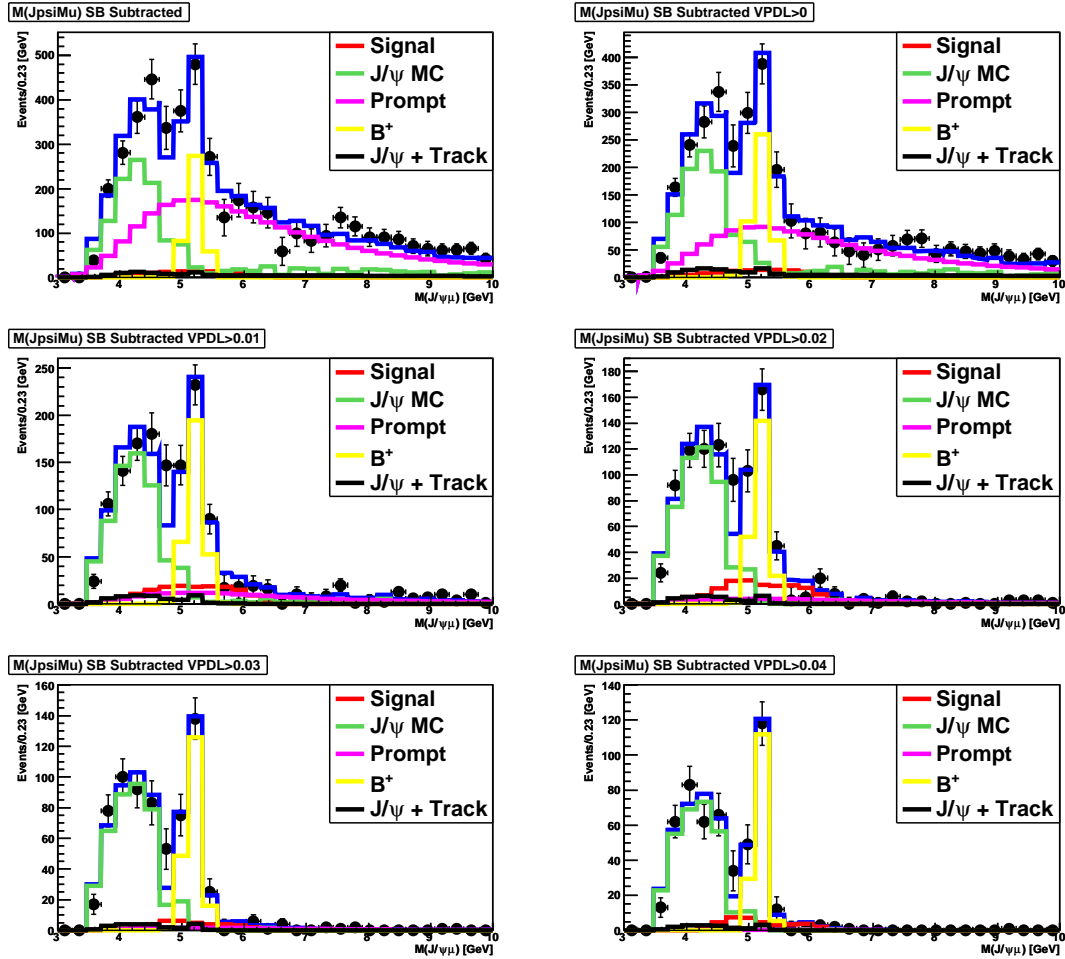


Figure 5.22: Mass fits after cutting progressively harder on the pseudo-proper decay length (PPDL) of the vertex. Note that there is still signal apparent at the lower PDDL cuts, but for very large values, the fit indicates that the components are dominated by the long-lived J/ψ QCD and the B^+ components; the prompt component has almost completely disappeared as has the signal.

where each term will be defined in subsequent subsections.

The total is broken up in this manner because the fraction of those events that are from the $J/\psi + \text{track}$ background determined using the fit to the number of B^+ events in the $J/\psi + \text{track}$ sample versus the $J/\psi + \mu$ sample as shown in Fig. 5.11 and discussed in Section 5.5.2, is used as an input i.e., $f_{jtrk} = 0.0338 \pm 0.0020$. Similarly, the number of those events that are $J/\psi + \mu$ sideband events, or fake J/ψ events, are taken from the fraction of data events that are in the sideband when compared to the number within the J/ψ signal region, i.e., $f_{sb} = 0.6672 \pm 0.0036$ (see Section 5.5.3 and Fig. 5.13). In the final fit, these fractions are allowed to float within a Gaussian penalty function, where the width of the Gaussian function is the indicated error on each value.

Each component consists of a mass shape template as described and shown in Section 4, as well as a lifetime functional model multiplied together. The shape of each lifetime component is described below.

5.7.1 Prompt J/ψ ($c\bar{c}$)

As described in the mass modeling section, events taken to describe this component are those with negative decay length. As verified in MC samples,

the prompt lifetime distribution is expected to be symmetric around a PDDL of zero. The lifetime distribution of events with negative decay length was then “mirrored” around zero, as shown in Fig. 5.23, and fit with a double (same mean) Gaussian function. This was done only to validate the functional form; in the full fit a Gaussian resolution function (Eq. 5.8) is used with floating parameters:

$$\mathcal{R}(\lambda_j, \sigma(\lambda_j), s) = \left(\frac{1}{\sqrt{(2\pi\sigma)(\lambda_j)s}} \right) e^{\frac{-(\lambda_j - \lambda_0)^2}{2(\sigma(\lambda_j)s)^2}}, \quad (5.8)$$

where $\sigma(\lambda_j)$ is the event-by-event uncertainty on the PDDL, and s is a floating scale factor to take into account any systematic underestimate of this error due to tracking systematic uncertainties not being included in the errors on the track parameters.

The total for this lifetime model is then:

$$\mathcal{F}_{pr}^i = f_{g1} \mathcal{R}(\lambda_j, \sigma(\lambda_j), s) + (1 - f_{g1}) \mathcal{R}(\lambda_j, \sigma(\lambda_j) \cdot k, s), \quad (5.9)$$

where k is a multiplicative factor on the width of the second Gaussian function compared to the first, and f_{g1} is the fractional weighting of the first Gaussian function.

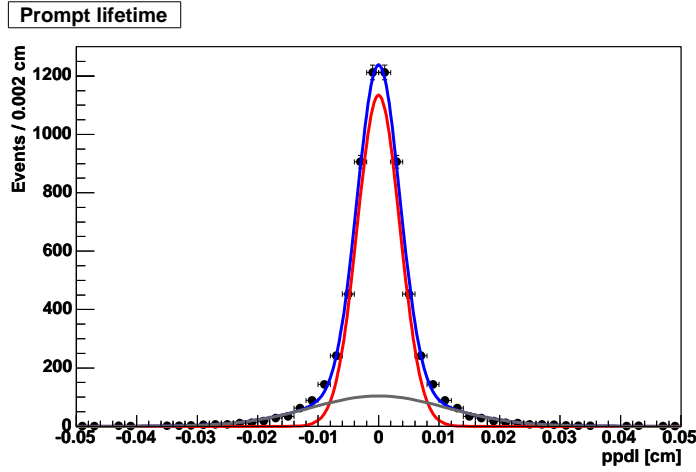


Figure 5.23: PPDL of events with negative decay length, mirrored about the zero point of the x axis.

5.7.2 Real J/ψ + Fake μ

As shown in Fig. 5.24, a fit was made to the PPDL distribution in the J/ψ + track sample to obtain the lifetime PDF for this sample. An empirical functional form as shown below was used with the parameters fixed to the values in Table 5.1, and only the normalization, via the fraction f_{jtrk} , was allowed to float in the fit.

$$\mathcal{F}_{jtrk}^i = f_{L1} \frac{e^{-\lambda/\lambda^{L1}}}{\lambda^{L1}} + f_{L2} \frac{e^{-\lambda/\lambda^{L2}}}{\lambda^{L2}} + f_G \mathcal{R}(\lambda_j, \sigma(\lambda_j), s) + \quad (5.10)$$

$$f_{R1} \frac{e^{\lambda/\lambda^{R1}}}{\lambda^{R1}} + f_{R2} \frac{e^{\lambda/\lambda^{R2}}}{\lambda^{R2}} + (1 - f_{L1} - f_{L2} - f_G - f_{R1} - f_{R2}) \frac{e^{\lambda/\lambda^{R3}}}{\lambda^{R3}}.$$

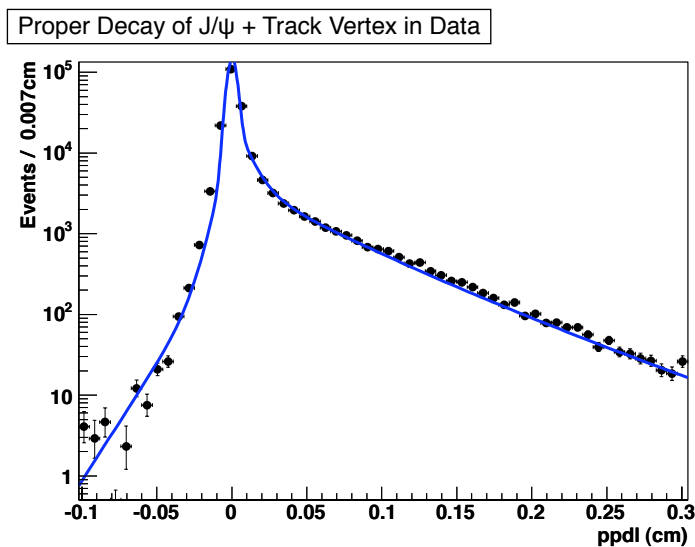


Figure 5.24: Fit to PDDL distribution of events in the J/ψ + track data set. As will be seen, the contribution of this category in the final fit will only be a few percent.

The Gaussian resolution function above is the same as described in Eq. 5.8.

5.7.3 Fake J/ψ + Real μ

This component is described by the PDDL distribution in the J/ψ sideband sample as shown in Fig. 5.25. The empirical function that is used for the PDF for this component is given by:

$$\mathcal{F}_{jsb}^i = f_{CG} (f_{g1} \mathcal{R}(\lambda_j, \sigma(\lambda_j), s) + (1 - f_{g1}) \mathcal{R}(\lambda_j, \sigma(\lambda_j) \cdot k, s)) + \quad (5.11)$$

$$f_{R1} \frac{e^{\lambda/\lambda^{R1}}}{\lambda^{R1}} + f_{L1} \frac{e^{-\lambda/\lambda^{L1}}}{\lambda^{L1}} + (1 - f_{CG} - f_{R1} - f_{L1}) \frac{e^{\lambda/\lambda^{R2}}}{\lambda^{R2}}.$$

Table 5.1: Function parameters for empirical J/ψ + track PDDL model.

Parameter	Value
f_{L1}	0.06
f_{L2}	0.007
f_G	0.63
f_{R1}	0.15
f_{R2}	0.09
λ^{L1}	0.005 cm
λ^{L2}	0.015 cm
λ^{R1}	0.008 cm
λ^{R2}	0.04 cm
λ^{R3}	0.068 cm

The fit parameters found in the fit in the J/ψ mass sideband sample are given in Table 5.2, and these remain fixed within the total fit.

5.7.4 Real J/ψ + Real μ

The PDF that was used to model the lifetime distribution of this component is given by:

$$\mathcal{F}_{jmc}^i = (1 - f_L) \left(f_{R1} \frac{e^{-\lambda/\lambda^{R1}}}{\lambda^{R1}} + (1 - f_{R1}) \frac{e^{-\lambda/\lambda^{R2}}}{\lambda^{R2}} \right) + f_L \frac{e^{-\lambda/\lambda^{L1}}}{\lambda^{L1}}. \quad (5.12)$$

A fit, as shown in Fig. 5.26 was made on the J/ψ QCD Monte Carlo sample to obtain the values that will be used as starting values in the full fit. They

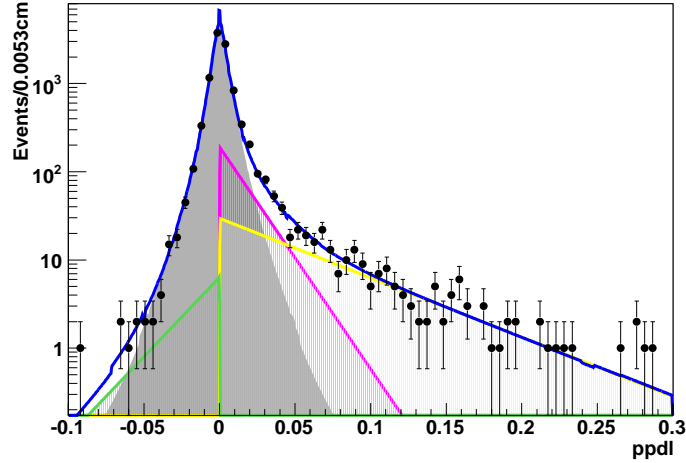


Figure 5.25: Fit to PPDL distribution of events in the J/ψ mass sidebands.

are listed in Table 5.3 where the values are indicated as fixed, fixed within a Gaussian penalty function, or allowed to float freely in the fit.

5.7.5 B^+

The lifetime PDF for this component is a single exponential function with slope taken from the PDG [3], i.e., $\tau(B^+) = 1.638 \pm 0.011$ ps. This value was allowed to float but constrained within a Gaussian penalty function, the width of which was the error on the measurement in the PDG. The PPDL values for this component were scaled to take into account the mass difference between the B^+ and the B_c mesons.

Table 5.2: Function parameters for the empirical J/ψ mass sideband PDDL model.

Parameter	Value	Error	Fixed	Fixed w/ Gaussian	Float Freely
f_G	0.900	0.007	×		
f_{R1}	0.056	0.009		×	
f_{L1}	0.003	0.001		×	
λ^{R1}	0.0160 cm	0.0023 cm			×
λ^{R2}	0.0571 cm	0.0056 cm			×
λ^{L1}	0.0214 cm	0.0059 cm			×

5.7.6 Signal

The signal PDF lifetime function is comprised of an exponential function convoluted with a Gaussian resolution function \mathcal{R} and smeared with the normalized K -factor distribution $\mathcal{H}(K)$, defined as:

$$\mathcal{F}_{sig}^i(\lambda_j, \sigma(\lambda_j), s) = \int dK \mathcal{H}(K) \left[\frac{K}{c\tau(B_c)} e^{-K\lambda_j/c\tau(B_c)} \otimes \mathcal{R}(\lambda_j, \sigma(\lambda_j), s) \right] \quad (5.13)$$

where:

$\tau(B_c)$ = the lifetime of the B_c signal candidates;

\mathcal{R} = resolution function, as described in Eq. 5.8.

The scale factor s on the event-by-event decay length uncertainty is the same parameter as used in the definition of the prompt lifetime PDF.

Table 5.3: Function parameter for J/ψ QCD MC PDDL model.

Parameter	Value	Error
f_L	0.090	0.005
f_{R1}	0.251	0.020
λ^{R1}	0.0067	0.0006
λ^{R2}	0.0518	0.0016
λ^{L1}	0.0037	0.0002

The integration of the K -factor PDF is approximated by a sum as follows:

$$\int dK \mathcal{H}(K) \rightarrow \sum_k \Delta K \mathcal{H}(K_k). \quad (5.14)$$

In addition to the above, the K -factor distributions are binned in the $M(J/\psi\mu)$ value of the given candidate (see Fig. 5.7).

Also note that 6.5% of the events are randomly chosen to have come from the feed-down component as described in Section 5.5.1. This sample has all the same properties of the above description but with K factors and mass templates taken from the generated $\psi(2S)$ sample.

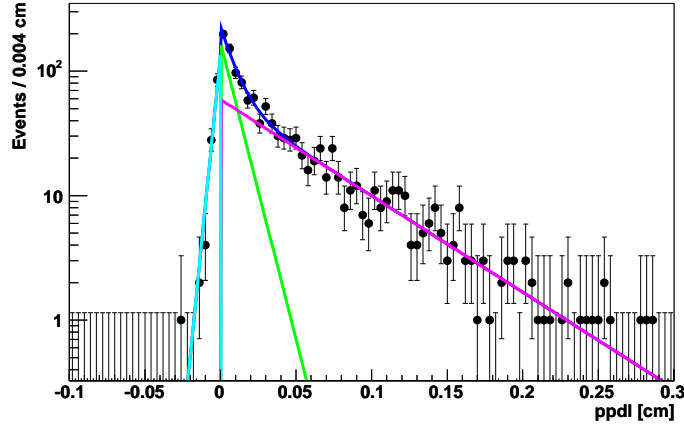


Figure 5.26: Fit to PPDL distribution of the J/ψ QCD MC sample.

Check for Lifetime Bias

Before examining the fit to the data, as a check, three different signal B_c^\pm Monte Carlo samples were generated with different lifetimes. The original lifetime sample had an input of $c\tau = 0.014$ cm, so one sample was generated with a 50% smaller value, i.e., $c\tau = 0.007$ cm, and another generated with a lifetime 50% larger at $c\tau = 0.021$ cm. Fits were performed to the true decay lengths of the sample and to the PPDL distributions and compared as shown in Fig 5.27. A linear fit to these values indicates a slope consistent with 1.0, i.e., no evidence of bias. Ensemble tests indicate the validity of the extracted statistical uncertainty and also show no evidence of a lifetime bias.

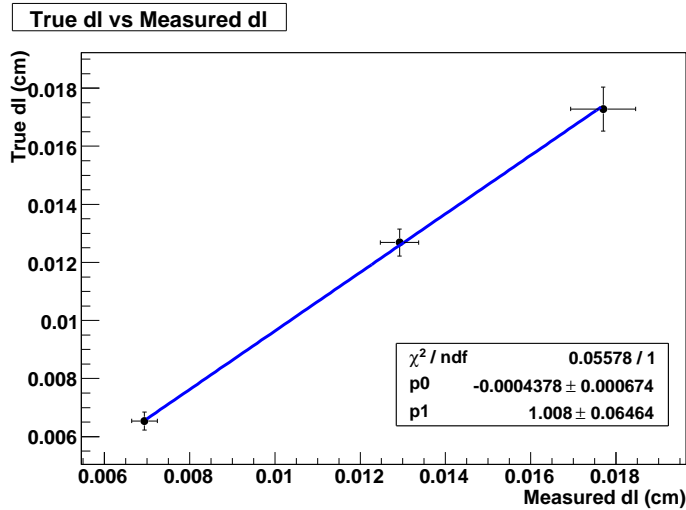


Figure 5.27: True decay length of the B_c versus the measured PPDL for the B_c signal MC.

5.7.7 Full Fit and Results

A simultaneous mass and lifetime fit was performed using all the components described in previous sections. The fitted lifetime of the B_c meson is found to be:

$$\tau(B_c^\pm) = 0.448^{+0.038}_{-0.036} \text{ (stat) ps.}$$

with an estimated signal sample of 881 ± 80 (stat.) candidates. The significance of the signal is 11.4σ , i.e., found using the difference in the log likelihood with and without the signal component.

Results of the fit variables are given in Table 5.4, and Fig. 5.28 shows the $M(J/\psi\mu)$ and PPDL distributions of the $J/\psi + \mu$ sample with projections of the fit result overlaid. Table 5.5 shows the correlations between all the variables in the fit. The largest correlations were between the variables that were heavily involved in the determination of the second gaussian on the prompt component.

Table 5.4: Results of the full simultaneous likelihood fit.

Parameter	Fit Value \pm Stat. Error	
f_{sig}	0.1837 ± 0.0167	
f_{jmc}	0.2070 ± 0.0123	
f_{bp}	0.0558 ± 0.0060	
λ_{jmc}^{R1}	0.0074 ± 0.0006	cm
λ_{jmc}^{R2}	0.0561 ± 0.0031	cm
λ_{jmc}^{L1}	0.0052 ± 0.0016	cm
f_{jmc}^{R1}	0.2131 ± 0.0189	
$\tau(B_c)$	0.4484 ± 0.0369	ps
f_{g1}	0.7557 ± 0.0221	
k	2.2767 ± 0.0670	
s	1.3457 ± 0.0242	
λ_{bp}	0.0584 ± 0.0003	cm
f_{jsb}	0.6639 ± 0.0034	
f_{jtrk}	0.0327 ± 0.0018	

Table 5.5: Correlation matrix of all variables in the full fit.

	f_{sig}	f_{jmc}	f_{bp}	λ_{jmc}^{R1}	λ_{jmc}^{R2}	λ_{jmc}^{L1}	f_{jmc}^{R1}	$\tau(B_c)$	f_{g1}	k	s	λ_{bp}	$f_{j sb}$	$f_{j trk}$
f_{sig}	-	-0.38	-0.32	-0.06	0.25	0.06	-0.01	-0.10	0.08	-0.03	-0.02	0.02	0.05	0.06
f_{jmc}	-0.38	-	0.13	0.01	-0.37	-0.03	0.12	-0.21	0.01	-0.02	0.00	-0.01	0.18	-0.03
f_{bp}	-0.33	0.13	-	0.02	-0.12	-0.01	-0.01	-0.23	-0.01	0.01	0.00	-0.03	0.09	0.01
λ_{jmc}^{R1}	-0.06	0.01	0.02	-	0.05	0.01	0.14	-0.01	0.00	0.00	-0.01	0.00	0.00	0.00
λ_{jmc}^{R2}	0.25	-0.37	-0.12	0.05	-	0.01	0.17	0.07	0.00	0.02	0.00	0.00	-0.01	0.02
λ_{jmc}^{L1}	0.06	-0.03	-0.01	0.01	0.01	-	-0.01	0.00	-0.04	-0.14	-0.09	0.00	-0.01	0.00
f_{jmc}^{R1}	-0.01	0.12	-0.01	0.14	0.17	-0.01	-	0.10	0.01	0.00	0.01	0.00	0.00	-0.01
$\tau(B_c)$	-0.10	-0.21	-0.23	-0.01	0.07	0.00	0.10	-	-0.07	-0.08	-0.02	0.01	0.01	-0.00
f_{g1}	0.08	0.01	-0.01	0.00	0.00	-0.04	0.01	-0.07	-	0.49	0.77	0.00	0.00	0.00
k	-0.03	-0.02	0.01	0.00	0.02	-0.14	0.00	-0.08	0.49	-	0.09	0.00	-0.01	-0.01
s	-0.02	0.00	0.00	-0.01	0.00	-0.09	0.01	-0.02	0.77	0.09	-	0.00	0.00	0.00
λ_{bp}	0.02	-0.01	-0.03	0.00	0.00	0.00	0.00	0.01	0.00	0.00	0.00	-	0.00	0.00
$f_{j sb}$	0.05	0.18	0.09	0.00	-0.01	-0.01	0.00	0.01	0.00	-0.01	0.00	0.00	-	0.02
$f_{j trk}$	0.06	-0.03	0.01	0.00	0.023	0.00	-0.01	-0.01	0.00	-0.01	0.00	0.00	0.02	-

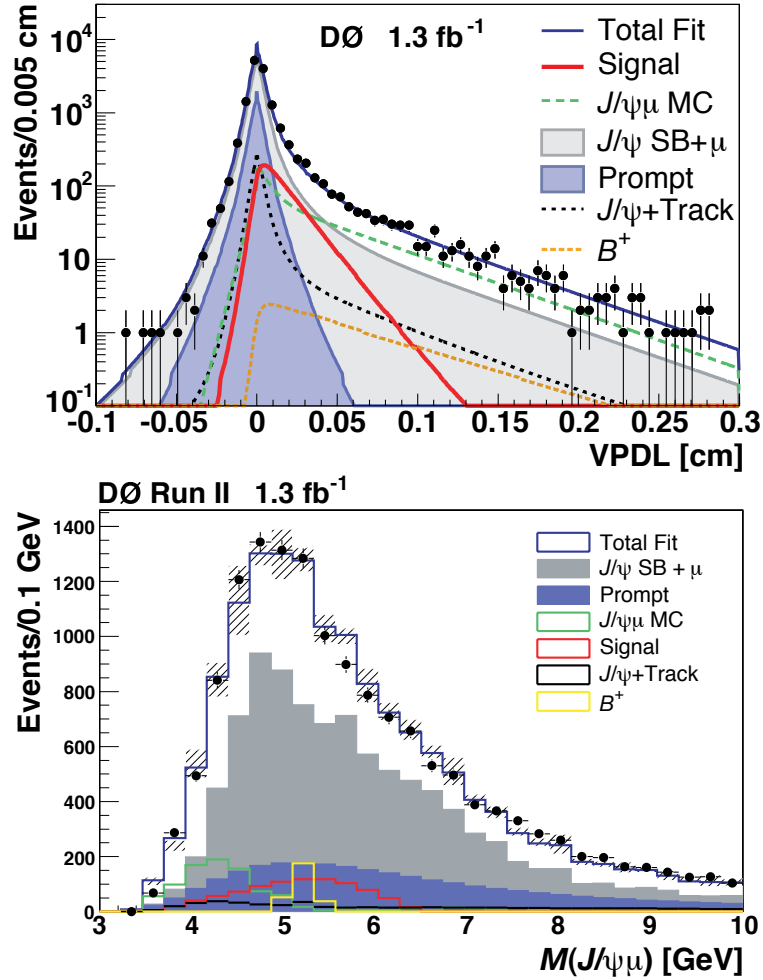


Figure 5.28: PPDL and Mass distribution of the $J/\psi+\mu$ sample with the projected components of the fit overlaid. The hatching on the mass distribution is the systematic uncertainty of all the components as well as the statistical uncertainty from the sideband component, which is the largest contribution.

Chapter 6

Systematic Uncertainties and Analysis Checks

*“The first principle is that you must not fool yourself and you
are the easiest person to fool.” Richard P. Feynman*

The B_c^\pm meson lifetime measurement has numerous systematics tests applied and are discussed in the following chapter. Systematic uncertainties cover uncertainties in the lifetime and mass template shapes for each component of the analysis as well as possible effects due to the event simulations and alignment. All will be covered in further detail in the following sections.

6.1 Mass Shape Systematic Uncertainties

Uncertainties on the K -factor for the signal and on the mass templates for both signal and background components are considered in the following subsections.

6.1.1 Signal Decay Model

Another sample of B_c signal Monte Carlo was generated, but with a decay model of phase space rather than the ISGW2 model [17] that was used for the default analysis. The lifetime fit was then rerun with a distribution for the $M(J/\psi\mu)$ and K -factor determined from this new MC sample. The mass distribution difference can be seen in Figure 6.1. The result is:

$$\tau(B_c^\pm) = 0.44321 \pm 0.03645 \text{ ps};$$

$$\Delta\tau(B_c^\pm) = \pm 0.00515 \text{ ps}.$$

Variations of the B_c mass within its measurement uncertainties, $M(B_c) = 6274.1 \pm 3.2 \pm 2.6 \text{ MeV}$ [51], made negligible difference on the lifetime.

6.1.2 $\psi(2S)$ Feed-Down Signal Component

Varying the feed-down $B_c \rightarrow \psi(2S)X$ signal component fraction from 6.5% down to zero contribution and then doubling to 13%, which is the

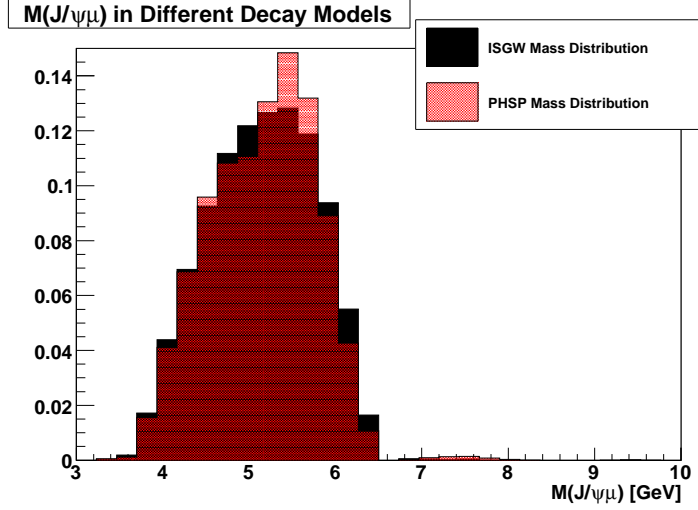


Figure 6.1: $M(J/\psi\mu)$ difference for the ISGW and Phase Space (PHSP) Models.

worst case scenario as described previously, gives the following:

$$0\% \text{ Feed Down : } \tau(B_c^\pm) = 0.44494 \pm 0.03671 \text{ ps;}$$

$$\Delta\tau(B_c^\pm) = -0.00342 \text{ ps;}$$

$$13\% \text{ Feed Down : } \tau(B_c^\pm) = 0.45330 \pm 0.03826 \text{ ps;}$$

$$\Delta\tau(B_c^\pm) = +0.00494 \text{ ps.}$$

6.1.3 Uncertainty on the B_c^\pm p_T Distribution

A source of uncertainty on the predicted MC distribution of $p_T(B_c)$ is due to the choice of the factorization scale μ . The default weighting used

was $\mu = \mu_R = \sqrt{(p_T^2(\text{parton}) + m_b^2)}$. Weightings to this p_T distribution as determined from Ref. [20] were used to vary this distribution to that expected for $\mu = \mu_R/2$ and $\mu = 2\mu_R$ as shown in Fig 6.2. This was described in more detail in Section 2.4.3.

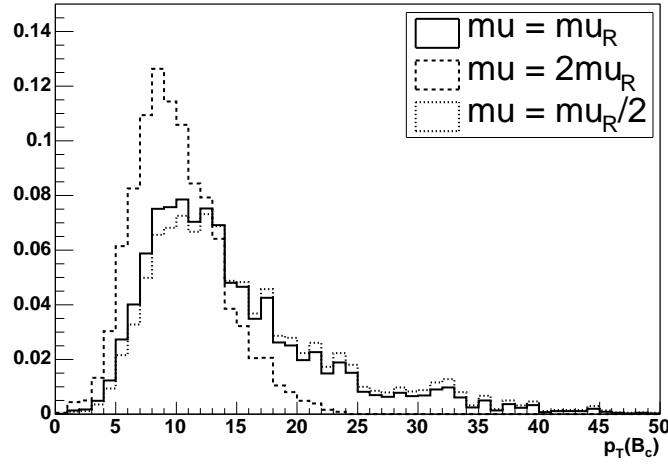


Figure 6.2: Predicted $p_T(B_c)$ distribution after event selection before and after reweighting to different factorization scales.

The fit to the lifetime was remade to find :

$$\mu = \mu_R/2 : \tau(B_c^\pm) = 0.44825 \pm 0.03715 \text{ ps};$$

$$\Delta\tau(B_c^\pm) = -0.00011 \text{ ps};$$

$$\mu = 2\mu_R : \tau(B_c^\pm) = 0.45459 \pm 0.03690 \text{ ps};$$

$$\Delta\tau(B_c^\pm) = +0.00624 \text{ ps};$$

Other sources of uncertainty on $p_T(B_c)$ could arise from uncertainty on the initial parton distributions in the proton - antiproton collision; however, variations in overall $p_T(b)$ described below are estimated to cover this source.

6.1.4 Uncertainties on $p_T(b)$ Distributions

The weighting factor described in Section 5.2.4 was removed and the lifetime fit repeated with the new mass distributions determined from both signal and background MC samples. The difference in the distribution can be seen in Figures 6.3 and 6.4, for the signal MC and J/ψ MC respectively. The resulting lifetime of B_c^\pm is:

$$\tau(B_c^\pm) = 0.45440 \pm 0.03814 \text{ ps};$$

$$\Delta\tau(B_c^\pm) = \pm 0.00605 \text{ ps}.$$

Note that this weighting factor was also normally applied to the signal MC sample to determine the signal mass shape *and* K -factor distribution. When the weighting was dropped, these were re-determined as well in the new fit above.

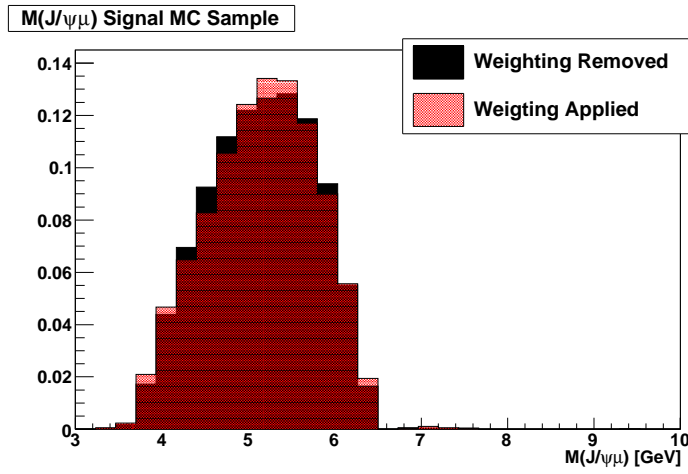


Figure 6.3: Mass of the $J/\psi + \mu$ distribution in the signal Monte Carlo sample with and without the $p_t(b)$ weighting applied.

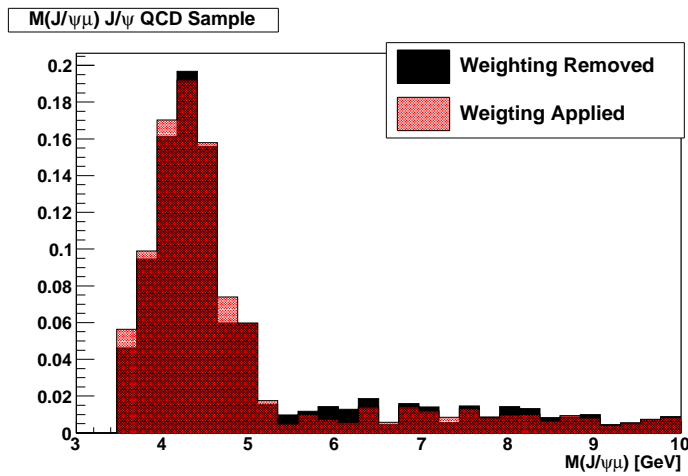


Figure 6.4: Mass of the $J/\psi + \mu$ distribution in the J/ψ QCD Monte Carlo sample with and without the $p_T(b)$ weighting applied.

6.1.5 J/ψ MC Mass Distribution

The J/ψ MC mass distribution has contributions from several different physics processes: flavor creation, where two quarks or gluons annihilate to produce a b and \bar{b} ; flavor-excitation, where one of the b quarks from a $b\bar{b}$ pair in the sea scatters off a parton; and gluon-splitting, where a gluon scatters and then splits to a $b\bar{b}$ pair. To assess the systematic uncertainty on this sample, we examine the effect of separating these contributions, i.e., instead of using all of events from the J/ψ QCD MC sample, we remove both the gluon splitting and flavor excitation decays.

To remove these components, we look at the Monte Carlo truth information and look at the parentage of the J/ψ and μ . Several different categories of events are considered: J/ψ from a b -hadron and μ not from a b -hadron; neither the J/ψ or μ from a b -hadron; both the J/ψ and the μ from a b -hadron, but not the same b -hadron; J/ψ not from a b -hadron and μ from a b -hadron; and the J/ψ and μ from the same b -hadron. The $\Delta(\phi)$, where $\Delta(\phi)$ is the angle between the J/ψ and $m\mu$, distribution for all these contributions can be seen in Figure 6.5. To see the gluon splitting contribution, we can look at the $\Delta(\phi)$ distribution for events with the requirement that both the J/ψ and μ are from a b -hadron. This can be seen in Figure 6.6. There is

a peak of events with low $\Delta(\phi)$ due to the kinematics of gluon splitting, but there are also events at larger masses, partially due to misreconstructions. To properly remove the gluon splitting and flavor excitation however, the next level of parentage has to be found. In other words the parents of the parents of the J/ψ and μ . Due to the way that the MC ‘truth’ information of gluons and quarks is stored in the simulated events, if the grandparents of both the J/ψ and μ are then b -hadrons, the component is subtracted from the total.

The new result after removing the gluon splitting and the flavor excitation contribution is:

$$\tau(B_c^\pm) = 0.43627 \pm 0.03618 \text{ ps};$$

$$\Delta\tau(B_c^\pm) = \pm 0.01209 \text{ ps}.$$

6.1.6 J/ψ Sideband Mass Distribution

It is assumed that the modeling of the J/ψ combinatoric background can be approximated by taking the average of the upper and lower mass sidebands. To test this assumption, the fit is first performed using only the lower mass sideband and then only the higher mass sideband, and a systematic uncertainty equal to one-half the resultant shifts in lifetime is assigned.

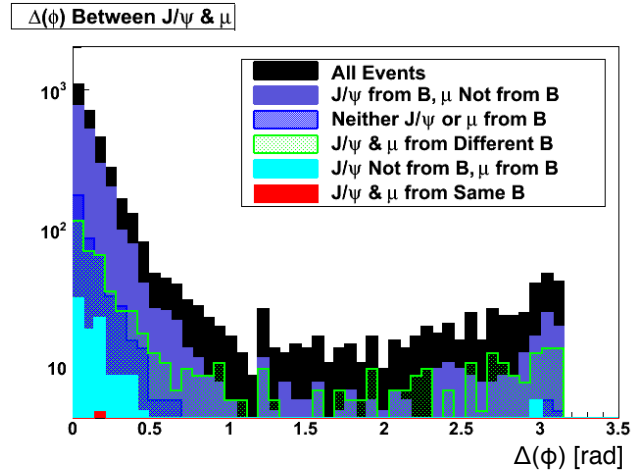


Figure 6.5: $\Delta(\phi)$ distribution for several different parentage categories.

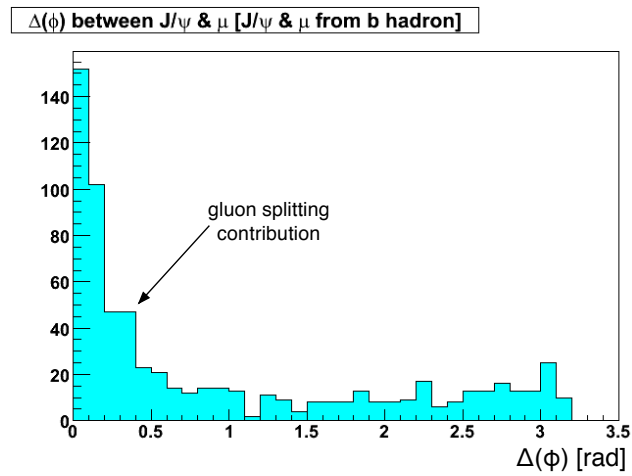


Figure 6.6: $\Delta(\phi)$ distribution for demonstrating gluon splitting contribution.

Low Mass Sideband Distribution, $\tau(B_c^\pm) = 0.47568 \pm 0.03840$ ps;

$$\Delta\tau(B_c^\pm) = 0.01366 \text{ ps};$$

High Mass Sideband Distribuion, $\tau(B_c^\pm) = 0.41864 \pm 0.03671$ ps;

$$\Delta\tau(B_c^\pm) = -0.01486 \text{ ps}.$$

6.1.7 Prompt Mass Distribution

To check the systematic uncertainty of the prompt mass component, the two values that are inputs to the Landau distribution fit to the shape were varied by $\pm 1\sigma$.

$$+1\sigma \tau(B_c^\pm) = 0.45352 \pm 0.03791 \text{ ps};$$

$$\Delta\tau(B_c^\pm) = +0.00517 \text{ ps};$$

$$-1\sigma \tau(B_c^\pm) = 0.44391 \pm 0.03647 \text{ ps};$$

$$\Delta\tau(B_c^\pm) = -0.00444 \text{ ps}.$$

6.2 Lifetime Model Systematic Uncertainties

6.2.1 Signal Lifetime Model

The fitted scale factor was found to be $s = 1.346 \pm 0.024$. The s scale factor value was fixed to $s = 1.2$ and then $s = 1.4$, as typical fit values as observed in other lifetime analyses [53].

$$s = 1.2, \tau(B_c^\pm) = 0.45485 \pm 0.03689 \text{ ps};$$

$$\Delta\tau(B_c^\pm) = +0.00649 \text{ ps};$$

$$s = 1.4, \tau(B_c^\pm) = 0.44788 \pm 0.03713 \text{ ps};$$

$$\Delta\tau(B_c^\pm) = -0.00048 \text{ ps}.$$

There is also the possibility that the the s factor could vary as a function of decay length. A systematic effect such as imperfect alignment, not taken into account in the calculated errors on track parameters, would potentially affect the shorter lived B_c^\pm meson more in comparison to other longer-lived B hadrons. A functional form was applied to calculate the s value based on the following criteria:

$$dL < 0 : s = s_{avg} + s_{avg} \times F$$

$$dL > 3 \cdot dL_{avg} : s = s_{avg} - 3 \times s_{avg} \times F$$

$$0 < dL < 3 \cdot dL_{avg} : s = s_{avg} - s_{avg} \times F \times \frac{dL - dL_{avg}}{dL_{avg}}$$

where dL is the decay length, dL_{avg} is the average decay length in the $J/\psi\mu$ sample, s_{avg} is the default value of s as determined by the original fit, and F is an additional scale factoring. With these requirements, if $dL = dL_{avg}$ the s value still takes on the default of 1.35. If the $dL < 0$ then s is forced to be higher by some factor F . If $dL > 3 \times dL_{avg}$ then the requirement

is that s is $3 \times F$ lower than the default value. For the values in between, the values are smoothly connected by a linear function, see Figure 6.7 for an illustration. F was chosen to be 0.02 and -0.02 to cover a reasonable possible range. After doing this the results of the fit are:

$$F = 0.02, \tau(B_c^\pm) = 0.44114 \pm 0.03344 \text{ ps};$$

$$\Delta\tau(B_c^\pm) = -0.00721 \text{ ps};$$

$$F = -0.02, \tau(B_c^\pm) = 0.45685 \pm 0.04130 \text{ ps};$$

$$\Delta\tau(B_c^\pm) = 0.00850 \text{ ps}.$$

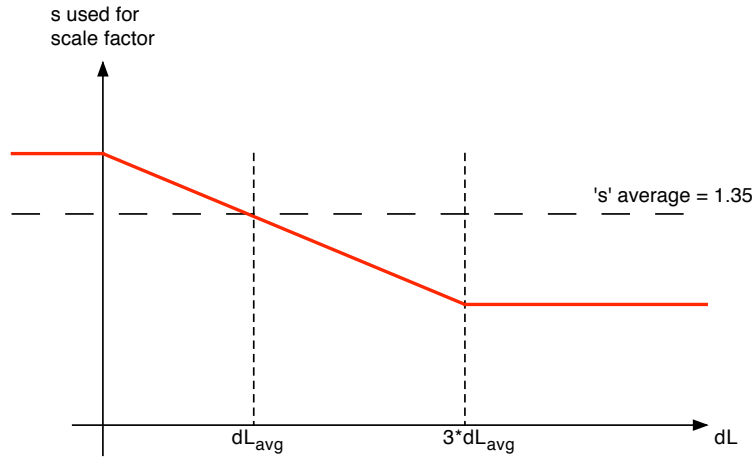


Figure 6.7: Depiction of the s scale factor taken as a function of decay length rather than a constant value.

6.2.2 Prompt Lifetime Model

Using a single Gaussian function rather than a double Gaussian as the PDF to describe the zero lifetime events yielded the following lifetime measurement:

$$\tau(B_c^\pm) = 0.43912 \pm 0.03311 \text{ ps};$$

$$\Delta\tau(B_c^\pm) = \pm 0.00923 \text{ ps}.$$

6.2.3 J/ψ Sideband Lifetime Model

Since all the parameters defining the empirical functional form are fixed, they are changed by $\pm 1\sigma$ with the resultant changes in the final fit result:

$$+1\sigma, \tau(B_c^\pm) = 0.46350 \pm 0.04239 \text{ ps};$$

$$\Delta\tau(B_c^\pm) = +0.01515 \text{ ps};$$

$$-1\sigma, \tau(B_c^\pm) = 0.43271 \pm 0.03610 \text{ ps};$$

$$\Delta\tau(B_c^\pm) = -0.01564 \text{ ps}.$$

6.2.4 J/ψ QCD Monte Carlo

For the parameters defining the empirical functional that are constrained by Gaussian penalty functions, their central values are changed by $\pm 1\sigma$ with the result:

$$+1\sigma, \tau(B_c^\pm) = 0.45142 \pm 0.03951 \text{ ps};$$

$$\Delta\tau(B_c^\pm) = +0.003006 \text{ ps};$$

$$-1\sigma, \tau(B_c^\pm) = 0.44577 \pm 0.03750 \text{ ps};$$

$$\Delta\tau(B_c^\pm) = -0.00259 \text{ ps}.$$

6.2.5 B^+ Lifetime Model

Since the B^+ lifetime value is constrained within a Gaussian penalty function, the central value was changed by $\pm 1\sigma$ keeping the “penalty” width the same. Therefore, checking at $\lambda_{B^+}=0.0488$ cm and $\lambda_{B^+}=0.0494$ cm:

$$\lambda_{B^+}=0.0494 \text{ cm}, \tau(B_c^\pm) = 0.44895 \pm 0.03618 \text{ ps};$$

$$\Delta\tau(B_c^\pm) = +0.00059 \text{ ps};$$

$$\lambda_{B^+}=0.0488 \text{ cm}, \tau(B_c^\pm) = 0.44843 \pm 0.03706 \text{ ps};$$

$$\Delta\tau(B_c^\pm) = 0.00008 \text{ ps}.$$

As an additional check, the B^+ lifetime was allowed to float in the full fit, finding a value of 1.83 ± 0.15 ps, consistent with the PDG value of 1.638 ± 0.011 ps [3].

The B_c^\pm lifetime value when the B^+ lifetime value was allowed to float is:

$$\lambda_{B^+}=\text{floating}, \tau(B_c^\pm) = 0.44078 \pm 0.03865 \text{ ps};$$

$$\Delta\tau(B_c^\pm) = \pm 0.00758 \text{ ps}.$$

6.3 Alignment Systematic

The signal Monte Carlo is re-reconstructed using a SMT geometry file where the silicon sensors are virtually moved from their nominal positions by an amount consistent with the current alignment precision. The lifetime is measured in the original sample, and then again in the same sample using the different SMT geometry file, with the result:

$$\Delta\tau = \pm 0.00590 \text{ ps.}$$

6.4 Split Sample Tests

To check the stability of the measurement, values of important variables were chosen so as to split the data sample roughly in half in each case. The lifetime was then found separately for each split sample and the difference in number of σ calculated, as given in Table 6.1. Since none of these split samples tests resulted in differences more than 2σ , i.e., all variations were consistent within statistical uncertainty no systematic uncertainties were assigned due to these split sample tests.

Table 6.1: Split sample tests.

Test	$\Delta c\tau(\text{cm})$	No. σ Diff.
$\eta(B_c) > 0$	0.00042	0.20
$\eta(B_c) < 0$	0.00058	0.27
$5 < p_T(B_c) < 10 \text{ GeV}$	0.00023	0.11
$p_T(B_c) > 10 \text{ GeV}$	-0.00117	-0.65
$\eta(\mu_3) > 0$	0.00104	0.51
$\eta(\mu_3) < 0$	0.00029	0.14
$ \eta(\mu_3) < 1$ (central)	-0.00080	-0.40
$ \eta(\mu_3) > 1$ (forward)	0.00329	1.44
$\phi(\mu_3) > 0$	0.00133	0.71
$\phi(\mu_3) < 0$	0.00045	0.19
$3.0 < p_T(\mu_3) < 4.5 \text{ GeV}$	0.00100	0.44
$p_T(\mu_3) > 4.5 \text{ GeV}$	0.00018	0.09
Run < 204950	-0.00171	-0.85
Run > 204950	0.00234	1.22

6.5 Summary

The estimated systematic uncertainties are summarized in Table 6.2. Adding the systematics in quadrature and symmetrizing the error for convenience, the measured B_c^\pm lifetime and total uncertainty is:

$$\tau(B_c^\pm) = 0.448_{-0.036}^{+0.038} (\text{stat}) \pm 0.032 (\text{sys}) \text{ ps.} \quad (6.1)$$

Table 6.2: Summary of estimated systematic uncertainties.

Systematic Source	$+\Delta\tau$ (ps)	$-\Delta\tau$ (ps)
Signal Decay Model	0.00515	0.00515
0% Feed Down	–	0.00342
13% Feed Down	0.00494	–
Uncertainty on $p_T(B_c)$ $\mu = 2\mu_R$	0.00624	–
Uncertainty on $p_T(B_c)$ $\mu = \mu_R/2$	–	0.00011
Uncertainty on $p_T(b)$	0.00605	0.00605
J/ψ MC Mass Distribution	0.01209	0.01209
Prompt Mass Distribution $+1\sigma$	0.00517	–
Prompt Mass Distribution -1σ	–	0.00444
Signal Lifetime Model $s = 1.2$	0.00649	–
Signal Lifetime Model $s = 1.4$	–	0.00048
Signal Lifetime Model - Function fraction = 0.02	–	0.00721
Signal Lifetime Model - Function fraction = -0.02	0.00850	–
Left Sideband Mass Model	0.01366	–
Right Sideband Mass Model	–	0.01486
Prompt Lifetime	0.00923	0.00923
J/ψ SB Lifetime Model $+1\sigma$	0.01515	–
J/ψ SB Lifetime Model -1σ	–	0.01564
J/ψ MC Lifetime Model $+1\sigma$	0.00306	–
J/ψ MC Lifetime Model -1σ	–	0.00259
B^+ Lifetime Model $+1\sigma$	0.00059	–
B^+ Lifetime Model -1σ	0.00008	–
B^+ Lifetime Model Float	0.00758	0.00758
Alignment	0.00590	0.00590
Total	0.03189	0.03070

Chapter 7

Summary and Conclusion

“Do not believe in anything simply because you have heard it. Do not believe in anything simply because it is spoken and rumored by many. Do not believe in anything simply because it is found written in your religious books. Do not believe in anything merely on the authority of your teachers and elders. Do not believe in traditions because they have been handed down for many generations. But after observation and analysis, when you find that anything agrees with reason and is conducive to the good and benefit of one and all, then accept it and live up to it.”

–Gautama Siddharta

In summary we have measured the B_c^\pm meson lifetime using the DØ detector to be :

$$\tau(B_c^\pm) = 0.448_{-0.036}^{+0.038} (\text{stat}) \pm 0.032 (\text{syst}) \text{ ps.} \quad (7.1)$$

Referring back at the theoretical predictions discussed in Section 2.4.4 and given in Table 7.1, we can see that this result is consistent with both predictions. Also given in this table is the most recent B_c^\pm meson lifetime preliminary measurement from the CDF experiment [55] and the most up to date Heavy Flavor Averaging Group (HFAG) world average. The measurement found in this analysis is consistent with both the theoretical predictions as well as the CDF measurement. The DØ and CDF results have comparable errors as shown in Figure 7.1, but this result is the most precise in the world and has been submitted for publication [54].

It was pointed out previously that the B_c^\pm meson should have a shorter lifetime than the other B hadrons due to the fact that there are three possible decay chains. In Figure 7.2 there is a visual depiction of the B_c^\pm meson lifetime compared to the lifetime values of the Λ_b , B^+ , B_s , and B_d . From this we can easily see that the lifetime of the B_c^\pm is much shorter than the other B hadrons, as expected.

Table 7.1: Experimental measurement compared with various theoretical predictions and the average (HFAG) of the experimental results.

Source	$c\tau(B_c^\pm)$ ps	
This result	$0.448^{+0.038}_{-0.036}$ (stat) ± 0.032 (syst)	[54]
OPE & PM	0.55 ± 0.15	[23, 24]
QCD Sum Rules	0.48 ± 0.05	[25]
CDF	$0.475^{+0.053}_{-0.049}$ (stat) ± 0.018 (syst)	[55]
HFAG, World Average	0.461 ± 0.036	

In conclusion, the B_c^\pm meson has been measured with the best precision ever with a value consistent with theoretical predictions.

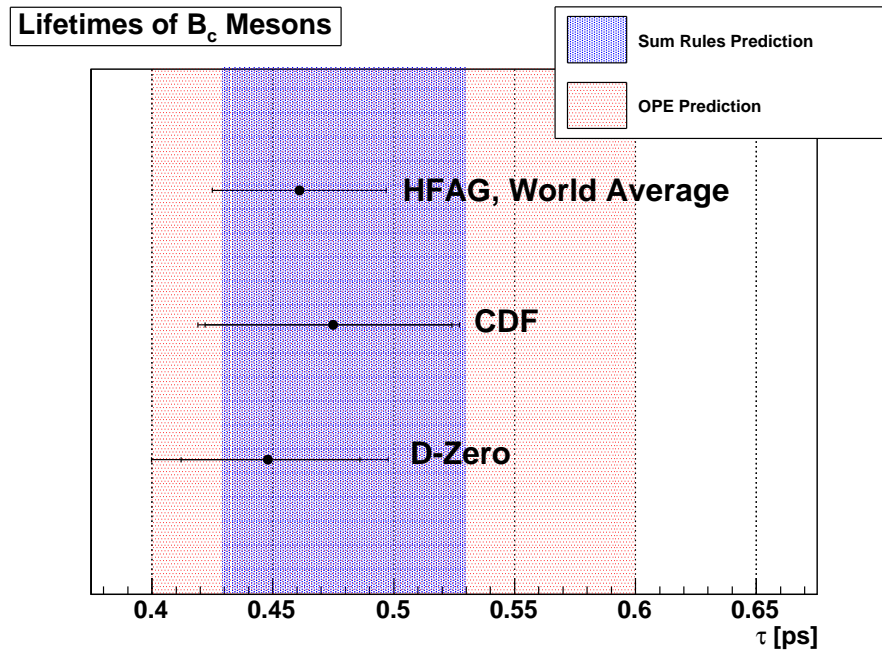


Figure 7.1: Lifetimes of the B_c^\pm meson at the DØ and CDF experiments as well as comparing with theoretical predictions.

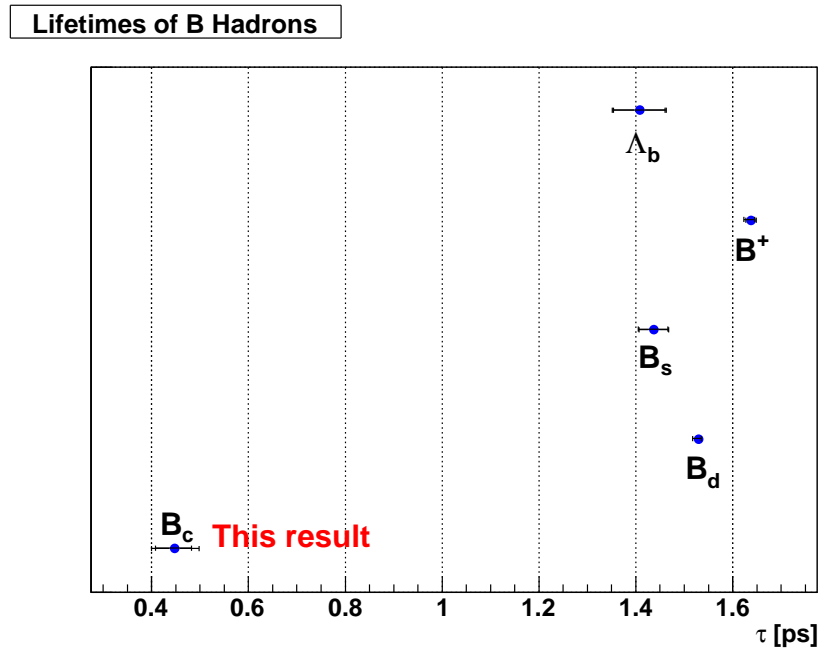


Figure 7.2: Lifetimes of various B hadrons including the experimental measurement of the B_c^\pm meson of this thesis.

Chapter 8

Appendix A

- Impact-parameter biasing triggers removed from sample are
 - ML1_TMM_IPPHI
 - MM1_TMM_IPPHI
 - ML2_MM_IPPHI
 - MM1_HI_TMM_IPPHI
 - MEB1_MM_IPPHI
 - ML1_IPTMM_IMP_V
 - MM1_IPTMM5_IMP_V
 - MM1_HI_IPTMM
 - ML1_TMM_2IP_IMP_V

- ML1_TMM_3IP_IMP_V
- ML1_TMM_4IP_IMP_V
- MM1_TMM_IMP_2IPV
- MM1_TMM_IMP_3IPV
- MM1_TMM_IMP_4IPV
- ML2_2IPMM_IMP_V
- ML2_3IPMM_IMP_V
- ML2_4IPMM_IMP_V
- ML3_2IPMM_IMP_V
- MM1_HI_TMM_2IPV
- MM1_HI_TMM_3IPV
- MEB1_2IPMM_IMP_V
- MEB1_3IPMM_IMP_V
- MEB1_4IPMM_IMP_V
- MUJB_MM0_BID
- JT1_ACO_MHT_BDV
- JT2_3JT15L_IP_VX

- JT3_3JT10L_LM3_V
- JT7_3JT15L_IP_VX
- MUJ1_2JT12_LMB_V
- MUJ1_JTHATK_LMVB
- MUJ2_2JT12_LMB_V
- MUJ2_JTHATK_LMVB
- ZBB_TLM3_2JBID_V
- ZBB_JT_HATKTLMV
- EZBB_SHT122J12VB
- MT3_L2M0_MM3_IP
- ZB1_TLM3_2JBID_V
- ZB1_JT15HA_TLM8V
- E3_SHT122J12VB

Bibliography

- [1] S. Weinberg, Phys. Rev. Lett. **19**, 1264 (1967); A. Salam, *Elementary Particle Theory*, ed. N.Svartholm, Almqvist and Wiksells, Stockholm, p. 367, (1969).
- [2] Y. Fukuda *et al.* [Super-Kamiokande Collab.], Phys. Rev. Lett. **81**, 1562 (1998).
- [3] W.-M. Yao *et al.*, Journal of Physics G **33**, 1 (2006) and 2007 partial update for edition 2008.
- [4] A. Pich, ‘*The Standard Model of Electroweak Interactions*’, hep-ph/0502010.
- [5] S. Glashow, Nucl. Phys. **22** (1961); S. Weinberg, Phys. Lett. **12** 132 (1967); A. Salam, *Elementary Particle Physics*.
- [6] J. Goldstone and S. Weinberg, Phys. Rev. **127**, 965 (1962).

-
- [7] P.W. Higgs, Phys. Lett. **12**, 132 (1964).
- [8] W. Marciano and H. Pagels, Phys. Rep. C **52**, 137 (1954).
- [9] N. Cabibbo, Phys. Rev. Lett. **10**, 531 (1963).
- [10] L. Wolfenstein, Phys. Rev. Lett. **51**, 1945 (1983).
- [11] R. Fleischer, '*Flavour Physics and CP Violation*', arXiv:hep-ph/0405091v1.
- [12] C. Jarlskog, Phys. Rev. Lett. **55**, 1039 (1985).
- [13] S. Godfrey, Phys. Rev. D **70**, 054017 (2004).
- [14] '*B Physics at the Tevatron: Run II and Beyond.*' FERMILAB-Pub-01/197 hep-ph/0201071, December 2001. Chapter 9.2.2 & 9.3
- [15] M. Neubert, '*Heavy-Quark Effective Theory*', hep-ph/9610266.
- [16] N. Isgur and M.B. Wise, Phys. Rev. Lett. B **232**, 113 (1989).
- [17] D. Scora and N. Isgur, Phys. Rev. D **52**, 2783 (1995).
- [18] T. Mannel, '*Review of Heavy Quark Effective Theory*', hep-ph/9611411v1.

- [19] A.V. Berezhnoy, A.K. Likhoded and M.V. Shevlyagin, *Yad. Fiz.* **58**, 730 (1995);
A.V. Berezhnoy, A.K. Likhoded, and O.P. Yushenko, *Yad. Fiz.* **59**, 742 (1996);
C.-H. Chang et al., *Phys. Lett. B* **364**, 78 (1995);
K. Kolodziej, A. Leike, and R. Ruckl, *Phys. Lett. B* **355**, 337 (1995);
A.V. Berezhnoy, V.V. Kiselev, and A.K. Likhoded, *Z. Phys. A* **356**, 79 (1996).
- [20] K. M. Cheung and T. C. Yuan, *Hadronic Production of S-wave and P-wave Charmed Beauty Mesons via Heavy Quark Fragmentation*, *Phys. Rev. D* **53**, 1232 (1996), [hep-ph/9502250v2].
- [21] J.D. Bjorken, Estimate of Decay Branching ratios for hadrons containing Charm and Bottom Quarks, draft report, 07/22/86 (1986) [unpublished].
(<http://www-theory.fnal.gov/people/ellis/Bphysics/bjorken.PDF>).
- [22] V. Kiselev, *Decays of the B_c Meson*, hep-ph/0308214 (2003), and references therein.
- [23] A.I. Onishchenko, *Doubly heavy systems: decays and OPE* [hep-ph/9912424].

- [24] M. Lusignoli, M. Masetti, *Z. Phys. C* **51**, 549 (1991);
V.V. Kiselev, *Mod. Phys. Lett. A* **10**, 1049 (1995);
V.V. Kiselev, *Int. J. Mod. Phys. A* **9**, 4987 (1994);
V.V. Kiselev, A.K. Likhoded, and A.V. Tkabladze, *Yad. Fiz.* **56**, 128 (1993);
V.V. Kiselev, A.V. Tkabladze, *Yad. Fiz.* **48**, 536 (1988);
G.R. Jibuti, Sh.M. Esakia, *Yad. Fiz.* **50**, 1065 (1989); *Yad. Fiz.* **51**, 1681 (1990);
C.-H. Chang, Y.-Q. Chen, *Phys. Rev. D* **49**, 3399 (1994);
D. Scora, N. Isgur, *Phys. Rev. D* **52**, 2783 (1995);
A.Yu. Anisimov, I.M. Narodetskii, C. Semay, B. SilvestreBra, *Phys. Lett. B* **452**, 129 (1999);
A.Yu. Anisimov, P.Yu. Kulikov, I.M. Narodetsky, K.A. Ter-Martirosian, *Phys. Atom. Nucl.* **62**, 1739 (1999).
- [25] V.V.Kiselev, A.K.Likhoded, A.E.Kovalsky, *Decays and Lifetime of B_c in QCD Sum Rules*, *Nucl. Phys. B* **585**, 353 (2000); hep-ph/0006104 (2000).
- [26] A. Khanov, '*HTF: histogramming method for finding tracks. The algorithm description*', DØ Note 3778 (2000).

- [27] G. Borrisov, ‘*Technical Details of AA Tracking*’, DØ Note in preparation, http://www-d0.fnal.gov/global_tracking/talks/.
- [28] T. Andeen *et al.*, ‘*The DØ Experiment’s Intergrated Luminosity for Tevatron Run IIa*’, FERMILAB-TM-2365 (2007).
- [29] p17 release: <http://www-d0.fnal.gov/computing/algorithms/>.
- [30] Common Sample Group,
http://www-d0.fnal.gov/Run2Physics/cs/skimming/skim_p17fixedPass2/doc_write.html.
- [31] BANA information page
<http://d0server1.fnal.gov/users/nomerot/Run2A/BANA/Dskim.html> .
- [32] T. Sjöstrand *et al.*, *Comp. Phys. Commun.* **135**, 238 (2001).
- [33] D.J. Lange, *Nucl. Instrum. Methods* **462**, 152 (2001);
EVTGEN package home page <http://hep.ucsb.edu/people/lange/EvtGen/>.
- [34] Y. Fisyak, J. Womersley, ‘*DØGSTAR: DØGEANT Simulation of the Total Apparatus Response*’, DØ Note 3191 (1997).
- [35] S. Youssef *et al.*, ‘*DØSIM User Manual*’, DØ Note 407 (1986).
- [36] R. Brun *et al.*, CERN Report No. DD/EE/84-1, 1984.

- [37] J. Thomson, '*Introduction to Colliding Beams*', FERMILAB-TM-1909 (1994).
- [38] <http://www-bd.fnal.gov/public/proton.html>.
- [39] <http://www-bd.fnal.gov/public/maininj.html>.
- [40] <http://www-bd.fnal.gov/public/antiproton.html>.
- [41] V.M. Abazov *et al.* [D0 Collab.], Nucl. Instrum. Meth. A **565**, 463 (2006).
- [42] V.M. Abazov *et al.* [DO Collab.], Nucl. Instrum. Meth. A **552**, 372 (2005).
- [43] L3 DAQ web page, <http://www-d0online.fnal.gov/www/groups/l3daq/doc/>.
- [44] D. Scora and N. Isgur, *Phys. Rev. D* **52**, 2783 (1995).
- [45] A. Chandra, K. Yip, and D. Zieminska, *Lifetime Difference and Polarization Amplitudes in the Decay $B_s \rightarrow J/\psi\phi$* , DØ Note 4810.
- [46] A. Abulencia *et al.* [CDF Collaboration], *Phys. Rev. Lett.* **96**, 082002 (2006) [arXiv:hep-ex/0505076].

- [47] V. M. Abazov *et al.* [DØ Collaboration], *Measurement of the B_c meson mass in the exclusive decay $B_c \rightarrow J/\psi\pi$* , Fermilab-Pub-08/047 [arXiv:hep-ex/0802.4258]
- [48] Muon ID web page
http://www-d0.fnal.gov/computing/algorithms/muon/muon_algo.html.
- [49] D. Ebert *et al.*, *Physical Review Letters* **D68**, 094020 (2003), and references therein.
- [50] J. Abdallah *et al.* [DELPHI Collaboration], *Eur. Phys. J.* **C32**, 185 (2004).
- [51] $B_c \rightarrow J/\psi\pi$ with 2.2 fb^{-1} , CDF Public Note 8004, July 22, 2007.
- [52] D. Acosta *et al.* [CDF Collaboration], *Phys. Rev. D* **71**, 092001 (2005) [arXiv:hep-ex/0412006].
- [53] V. Abazov *et al.*, D0 Collaboration *Phys. Rev. Lett.* **99**, 142001 (2007), *Physical Review Letters* **99**, 182001 (2007).
- [54] *Measurement of the lifetime of the B_c meson in the semileptonic decay channel*, arXiv:0805.2614; Fermilab-Pub-08/136-E, submitted to *Physical Review Letters*.

- [55] CDF Note 9294, *Measurement of the B_c Lifetime in the $B_c \rightarrow J/\psi + \ell + X$ Decays*, April 2008;
http://www-cdf.fnal.gov/physics/new/bottom/080327/blessed-BC_LT_SemiLeptonic/ .

Curriculum Vitae

Personal

- Leah Welty-Rieger

- e-mail: lwrieger@gmail.com

Education

- PhD Physics, Indiana University, Bloomington, 2002-2008

- B.S. Physics, Indiana University, Bloomington, 1997-2001

Research Experience

- FNAL DØ- The Lifetime of a Beautiful and Charming Meson : B_c
Lifetime in the Semileptonic Channel

Work Experience

- Obtiva - Software Developer - August 2008 - Present

- Indiana University - Research Assistant, 2002-2008